The Dissertation Committee for Matthew McCullough Sartin certifies that this is the approved version of the following dissertation:

The Electrogenerated Chemiluminescence of Unique Organic Chromophores

Committee:

_____
Allen J. Bard, Supervisor

_____
Alan Campion

_____
Richard M. Crooks

_____
David A. Vanden Bout

_____
Arumugam Manthiram

The Electrogenerated Chemiluminescence of Unique Organic Chromophores

by

Matthew McCullough Sartin, B.S.; M.A.

Dissertation

Presented to the Faculty of the Graduate School of

the University of Texas at Austin

in Partial Fulfillment

of the Requirements

for the Degree of

Doctor of Philosophy

The University of Texas at Austin

December 2007

Acknowledgments

I would like to thank Dr. Bard for all of his advice, my parents for their support, Angie Nelson for her help and for her advice on practical matters, and my labmates, past and present, for many fond memories.

The Electrogenerated Chemiluminescence of Unique Organic Chromophores

Publication No._____

Matthew McCullough Sartin, Ph.D.

The University of Texas at Austin, 2007

Supervisor: Allen J. Bard

Electrogenerated chemiluminescence (ECL) studies were performed on several interesting compounds. A series of silole-based (silacyclopentadiene) chromophores was examined to understand the effects of their structure on the electrochemistry and spectroscopy of these compounds. A case was observed in which high steric hindrance improved ECL by inhibiting internal conversion and protecting radicals from secondary reactions. Another case was observed in which steric effects induced a rotation in the silole substituents, increasing secondary reactions and lowering quantum efficiency (Φ_{PL}). Spiro-FPA, which consists of two DPA centers, exhibits excimer formation despite high steric hindrance, due to its ability to form di-ions, which have a greater electrostatic attraction to one another than mono-ions. The compound (dppy)BTPA is a highly solvatochromic, boron-containing chromophore that was examined in a variety of

solvents. Of note is the emission in pure acetonitrile, which is prominent in the ECL spectrum, but barely visible in the photoluminescence. Finally, B^8amide, a compound based on the laser dye, BODIPY, was examined. It exhibited unusual ECL characteristics. These include a strong, long-wavelength emission and transients that are clearly visible for 20 min or more, but display dramatically varying light intensities with each pulse. Evidence for the contribution of a film formed with the oxidation product is presented. Additionally, ECL simulations are performed using a general physics software package to better understand some of the observed phenomena.

Table of Contents

List of Figures

List of Tables

List of Schemes

Chapter 1: Electrogenerated Chemiluminescence

1.1 Background

Electrogenerated chemiluminescence (ECL) is the generation of light through electrochemical processes. Usually, this is done by annihilation between a radical anion and cation. Luminescence during electrolysis was first observed in the 1920s when Grignard compounds were oxidized at several hundred volts,[1] and again when luminol was electrochemically oxidized in an alkaline solution.[2] In 1964, Hercules showed that a square wave potential pulse could be used to generate light in the absence of oxygen.[3]

Following these early experiments, many developments have occurred in the field of ECL, including the use of coreactants,[4-6] which made aqueous ECL possible.[4,6] The low detection limit of ECL has made it an ideal analysis tool.[7] It is especially popular in the area of bioanalysis, where it has been used in enzyme detection, immunosensors,[8] and DNA probes.[9] While its applications are primarily biological, ECL studies are also performed on organic compounds in the absence of oxygen. This has led to the observation of many interesting phenomena from the electrochemistry and spectroscopy of a variety of unique compounds.

ECL is typically generated via annihilation of electrogenerated anions and cations, as shown in the following scheme:

$$A + e \rightarrow A^{\bullet -} \quad (1.1)$$

$$A - e \rightarrow A^{\bullet +} \quad (1.2)$$

$$A^{\bullet -} + A^{\bullet +} \rightarrow {}^1A^* + A \quad (1.3)$$

$${}^1A^* \rightarrow A + h\nu \quad (1.4)$$

Direct population of an electronic state can only occur if the energy of ion annihilation is greater than the electronic transition energy. The energy available for excited state generation is the internal energy, ΔU, which in condensed phase is approximately equal to the enthalpy. The condition for direct population of the singlet state is therefore $-\Delta H = \Delta G - T\Delta S > E_s$, where E_s is the singlet energy, and $T\Delta S \approx 0.1$ eV. This is known as S-route ECL. If the available energy is not sufficient, emission can still occur via triplet-triplet annihilation, in what is known as T-route ECL.

$$A^{\bullet -} + A^{\bullet +} \rightarrow {}^3A^* + A \quad (1.5)$$

$${}^3A^* + {}^3A^* \rightarrow {}^1A^* + A \quad (1.6)$$

$${}^1A^* \rightarrow A + h\nu \quad (1.7)$$

1.2 Coreactants

ECL can also be produced by using a coreactant. A coreactant is a compound that can, upon reduction or oxidation, become an oxidizing or reducing agent, respectively. The most common coreactants are benzoyl peroxide (BPO),[10] persulfate,[11] tripropylamine (TPrA),[12] and oxalate.[13]

TPrA and oxalate can both be oxidized to create reducing agents, while BPO and persulfate can be reduced to make oxidizing agents. For example, BPO reduction creates a benzoate radical with E^o = 0.8 V[14] or 1.5 V[10] via the following mechanism:

$$BPO + e \rightarrow BPO^- \quad (1.8)$$

$$BPO^- \rightarrow C_6H_5COO^- + C_6H_5COO^\bullet \quad (1.9)$$

If a chromophore in solution is reduced with the BPO, the excited state is generated as follows:

$$A + e \rightarrow A^{\bullet -} \quad (1.10)$$

$$A^{\bullet -} + C_6H_5COO^\bullet \rightarrow C_6H_5COO^- + A^* \quad (1.11)$$

Coreactants are typically used when one radical ion species is unstable and decomposes prior to annihilation. In the above mechanism, the anion and the oxidizing agent are produced almost simultaneously, so light can be generated even if the cation is too unstable. Coreactants are also helpful if one of the radical ions cannot be generated within the solvent window. TPrA, for instance, is often used with aqueous solutions, since most chromophores cannot be reduced within the solvent window of water. Ion annihilation ECL sometimes results in unusual phenomena, such as additional, long wavelength emission. Coreactants can be used to determine whether these phenomena result from ion annihilation, since coreactant ECL circumvents ion pair annihilation.[15]

1.3 Excimer Formation

An excimer is an excited state dimer that is unstable in the ground state. Their formation and decay are described by the following mechanism:

$$A^* + A^* \rightarrow A_2^* \quad (1.12)$$

$$A_2^* \rightarrow 2A + h\nu \quad (1.13)$$

Because they lack a stable ground state, they often feature broad, structureless emissions at longer wavelengths than the monomer emission.

Creation of excimers in ECL where none are observed in PL is believed to occur because of the close proximity of two species at the time of annihilation.[15,16] Excimer formation can also occur during triplet-triplet annihilation of energy insufficient ECL processes.[17]

Additional, long wavelength ECL does not necessarily indicate excimer formation, however. The electrochemical processes involved in ECL can be followed by homogeneous reactions that yield emissive products, as is the case with anthracene, which gives long wavelength ECL from the anthranol product of cation radical decomposition.[18] Cyclic voltammetry can be used to demonstrate the stability of the electrochemical processes. A simple test for excimer formation is to produce the ECL with a coreactant. Since ion pair annihilation will not occur as frequently when a coreactant is used, the long wavelength peak from excimer formation should be absent from the spectrum.[15]

1.4 Solvatochromism

Solvatochromism is a shift in the wavelength of the absorbance or fluorescence of a molecule as a function of some solvent parameter. This occurs in molecules that exhibit large charge separation between the electronic configurations of the ground and excited states.[19] If the charge separation results in a strong dipole moment in the excited state, S_1, then S_1 will be more stabilized in a polar solvent than in a nonpolar one. Thus, the two relaxation energies shown in Scheme 1.1 will be greater for a polar solvent, and the fluorescence will occur at longer wavelength.

Scheme 1.1. Jablonski diagram

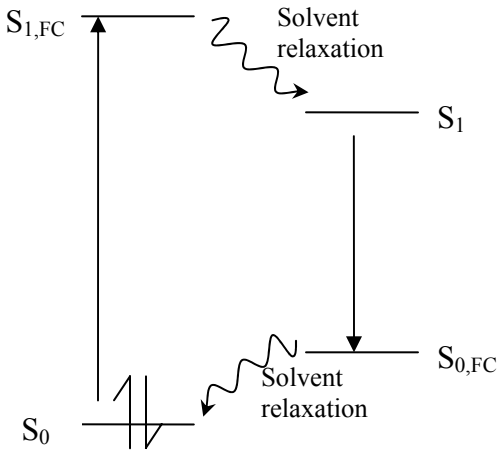

This phenomenon is often described using the Lippert equation,[19,20] which characterizes the Stokes shift in terms of the change in dipole moment between the ground and excited states:

$$\bar{\nu}_a - \bar{\nu}_f \cong \frac{2}{hc}\left(\frac{\varepsilon - 1}{2\varepsilon + 1} - \frac{n^2 - 1}{2n^2 + 1}\right)\frac{(\mu^* - \mu)^2}{a^3} + const \qquad (1.14)$$

This equation describes the Stokes shift of a molecule in a solvent cavity of radius *a*, also known as the Onsager radius. Planck's constant is *h*, *c* is the speed of light, ε is the dielectric constant, *n* is the refractive index, $\bar{\nu}_a$ and $\bar{\nu}_f$ are the absorbance and fluorescence wavenumbers, respectively, and μ^* and μ are the excited and ground state dipole moments. After electronic excitation of the chromophore, the surrounding solvent molecules must reconfigure their electron distribution and their orientation to minimize the energy of the chromophore in the excited state. The redistribution of electrons is believed to occur on the time scale of absorption, thus the Stokes shift, which consists of relaxation from the Franck-Condon excited state, $S_{1,FC}$, to the solvent-relaxed excited state, S_1, and the later relaxation from $S_{0,FC}$ to S_0, results only from the molecular reorientation of the solvent. This value is referred to as the solvent polarizability, Δf. It is obtained by subtracting the *n*-dependent electronic reorganization term from the ε-dependent total electronic and molecular reorganization.

For an ideal molecule, a plot of the Stokes shift versus Δf of a compound in a variety of solvents yields a straight line with a slope that can be used to determine the change in dipole moment. The Onsager radius can be roughly estimated from the radius of the molecule.[21] However, many molecules deviate from the expectations of the Lippert equations due to specific interactions of the

chromophore with the solvent[19] or because in some molecules, a low Δf favors locally excited electronic states over charge transfer states.[22] Moreover, the responses of some solvents, such as benzene, are more complicated than described by the Lippert equation, because they contain quadrupole moments.[23] Variations of the Lippert equation are available to deal with some of these complexities,[19] but these involve adding parameters to the equation.

It is more common in such cases to use an empirical scale, such as the E_T^N scale, in which the response of a standard compound, such as betaine-30, to a particular solvent is normalized according to its response to solvents of extreme polarizability.[24,25]

$$E_T^N = \frac{E_T(solvent) - E_T(TMS)}{E_T(water) - E_T(TMS)} \tag{1.15}$$

In (1.15), E_T represents the electronic transition energy in each solvent. TMS is tetramethylsilane, the nonpolar extreme, and water is the polar extreme. The Stokes shift can then be plotted versus the E_T^N values for each solvent, and $\Delta\mu$ can be extracted from the following equation:[26]

$$\bar{\nu}_a - \bar{\nu}_f = 11307.6\left(\frac{\mu^* - \mu}{\mu_S^* - \mu_S}\right)^2\left(\frac{a_S}{a}\right)^3 E_T^N + const \tag{1.16}$$

where μ_S and a_S are the dipole moment and cavity radius, respectively, of the standard compound. This expression corrects for many of the uncertainties in the

Lippert equation, but it still cannot correct for effects of specific interaction between solvent and chromophore.

1.5 References

(1) Dufford, R. T.; Nightingale, D.; Gaddum, W. L. *J. Am. Chem. Soc.* **1927**, *49*, 1858.
(2) Harvey, N. *J. Phys. Chem.* **1929**, *33*, 1456.
(3) Hercules, D. M. *Science*. **1964**, *145*, 808.
(4) Rubinstein, I.; Bard, A. *J. Am. Chem. Soc.* **1981**, *103*, 512.
(5) White, H.; Bard, A. *J. Am. Chem. Soc.* **1982**, *104*, 6891.
(6) Leland, J.; Powell, M. *J. Electrochem. Soc.* **1990**, *137*, 3127.
(7) For reviews of ECL applications, see: (a) Fahnrich, K.; Pravda, M.; Guilbault, G. *Talanta*. **2001**, *54*, 531. (b) Knight, A. *TrAC* **1999**, *18*, 47. (c) Richter, M. *Chem. Rev.* **2004**, *104*, 3025.
(8) Obenauer-Kutner, L.; Jacobs, S.; Kolz, K.; Tobias, L.; Bordens, R. *J. Immunol. Methods* **1997**, *206*, 25.
(9) Motmans, K.; Raus, J.; Vandevyver, C. *J. Immunol. Methods* **1996**, *190*, 107.
(10) Chandross, E.; Sonntag, F. *J. Am. Chem. Soc.* **1966**, *88*, 1089.
(11) White, H.; Bard, A. *J. Am. Chem. Soc.* **1982**, *104*, 6892.
(12) Leland, J.; Powell, M. *J. Electrochem. Soc.* **1990**, *137*, 3127.
(13) Rubenstein, I.; Bard, A. *J. Am. Chem. Soc.* **1981**, *103*, 512.
(14) Akins, D.; Birke, R. *Chem. Phys. Lett.* **1974**, *29*, 428.
(15) Choi, J.-P.; Wong, K.-T.; Chen, Y.-M.; Yu, J.-K.; Chou, P.-T.; Bard, A. *J. Phys. Chem. B* **2003**, *107*, 14407.
(16) Chandoross E.; Longworth, J.; Visco, R. *J. Am. Chem. Soc.* **1965**, *87*, 3259.
(17) Maloy, J.; Bard, A. *J. Am. Chem. Soc.* **1971**, *93*, 5968.
(18) Faulkner, L.; Bard, A. *J. Am. Chem. Soc.* **1968**, *90*, 6284.
(19) Lakowicz, J.; *Principles of Fluorescence Spectroscopy*. Plenum Press: NY, **1983**, pp 189-215.
(20) Lippert, V. *Z. Electrochem.* **1957**, *61*, 962.
(21) Seliskar, C.; Brand, L. *J. Am. Chem. Soc.* **1971**, *93*, 5414.
(22) Schuddeboom, W.; Jonker, S.; Warman, J.; Leinhos, U.; Kühnle, W.; Zachariasse, K. *J. Phys. Chem.* **1992**, *96*, 10809.
(23) Subuddh, U.; Haldar, S.; Sankararaman, S.; Mishra, A. *Photochem. Photobiol. Sci.* **2006**, *5*, 459.
(24) Reichardt, C. *Chem. Rev.* **1994**, *94*, 2319.
(25) Ravi, M.; Soujanya, T.; Samanta, A.; Radhakrishnan, T. *J. Chem. Soc. Faraday Trans.* **1995**, *91*, 2739.
(26) Rave, M.; Samanta, A.; Radhakrishnan, T. *J. Phys. Chem.* **1994**, *98*, 9133.

Chapter 2: Simulation of potential pulse ECL

2.1 Introduction

Digital simulations provide one of the most effective means of understanding the many complex processes in electrogenerated chemiluminescence. Due to the complexity of ECL processes and the fact that ECL is typically generated by pulsing the electrode potential between oxidation and reduction, visualizing the concentration profiles of the reacting species is difficult, and constructing an equation to describe the processes occurring in ECL is even more difficult. [1] Therefore, a simulation that circumvents this mathematical complexity is very beneficial.

Simulations of electrogenerated chemiluminescence began with early work by Feldberg, who produced a quantitative description of how ECL intensity varies with pulse width, concentration, and the anion-cation annihilation rate constant for a double-potential step experiment.[2] The slope of a Feldberg plot for a diffusion controlled annihilation reaction was used to characterize deviations from the standard model of ECL, which did not account for triplet-triplet annihilation, homogeneous following reactions, or radical ion quenching. Triplet-triplet annihilation was analyzed by later simulations and characterized by a larger slope.[3] This was followed by Cruser's work, which presented a simulation for multiple potential steps and examined the effects of a homogeneous first order

cation decomposition on the ECL peak intensity as a function of time.[4] A working curve showing the effects of various decomposition rate constants is also presented in this work.

These early simulations were written in programming languages such as FORTRAN. The chief advantage to programming in basic languages is the vast control that the programmer has over the problem. Cell geometry, applied potential function, quenching reactions, and many other parameters can be varied by the programmer. This is counterbalanced by the time required for programming and the difficulty of programming 2D and 3D systems. The programming time increased as electrochemical and ECL problems grew more complex, which led to the use of EC software packages, such as DigiSim,[5] DigiElch,[6] and ECL-PACKAGE[7] as a means of saving time and making simulations more broadly accessible. However, many of these programs are too specialized for certain work. DigiSim and DigiElch are strictly cyclic voltammetry programs, and some creativity is necessary to use them for even simple things like chronoamperometry. There is minimal control over the cell design or the applied potential program. ECL-PACKAGE, being specialized for ECL, is undoubtedly more versatile, but that, too, appears limited to ECL problems of current interest and established geometries, leaving little room for expansion to suit future needs.

To minimize programming time while retaining the ability to control a large variety of parameters, we have simulated basic ECL experiments using COMSOL Multiphysics, a general physics software package. Its generality slows the programming of simple problems compared to what a more specialized software package offers. However, more complicated problems are made easier, due to the complete control over cell geometry, and the ability to include other physical parameters not typically used in ECL simulations. In addition, a general program such as Multiphysics can be used for simulations unrelated to ECL or even electrochemistry.

In this chapter, we show how multi-potential step ECL can be simulated using the Multiphysics software package. Following Cruser's paper, we constructed a working curve based on the ratio of integrated ECL intensities for a system in which the cation radical decomposes at various rates.

2.2 Experimental

These simulations were written using the chemical engineering module of COMSOL Multiphysics. The simulation model is a one-dimensional cell with an electrode boundary condition on one side of the cell, and a semi-infinite boundary condition on the "open" side of the cell. The semi-infinite condition is achieved by making the cell considerably larger than the diffusion layer, and by maintaining the bulk concentration (1 mM) of the analyte at the "open" boundary of the cell. On the electrode side of the cell, the Butler-Volmer expression for

electrode reaction kinetics is applied. In Multiphysics, kinetic boundary conditions give the rate, v, of increasing concentration of a species, rather than the rate of its decomposition. Thus, for the reaction

$$A + e \rightarrow A^{\bullet -} \tag{2.1}$$

the electrode boundary condition is given by

$$v = k_b[A^{\bullet -}] - k_f[A] \tag{2.2}$$

where

$$k_f = k^o \exp[-\alpha F(E-E^o)/RT] \tag{2.3}$$

$$k_b = k^o \exp[(1-\alpha)F(E-E^o)/RT] \tag{2.4}$$

In these expressions, k_f is the rate constant of the forward reaction, k_b is for the back reaction, k^o is the standard rate for heterogeneous electron transfer, α is the electron transfer coefficient, E^o is the redox potential for the conversion of A to $A^{\bullet -}$, F is Faraday's constant, R is the gas constant, T is temperature, and E is the applied potential.

Application of the boundary condition to the electrode surface creates a concentration gradient, which allows diffusion of the reacting species to occur within the subdomain, according to Fick's laws of diffusion. The current can then be calculated at each time step from the normal diffusive flux of the reactant or product at the electrode boundary. If the pulses are made between oxidation and reduction, as in ECL, then the current will be the difference between the flux of $A^{\bullet +}$ and the flux of $A^{\bullet -}$.

Since the boundary condition for the "open" side of the cell simulates semi-infinite diffusion by mimicking another electrode, extensive interaction between the growing diffusion layer and the "open" boundary will distort the concentration profile of the entire cell. A sufficiently large cell will minimize such interactions, but at the cost of increased computational time. For these simulations, the concentration profiles were used to estimate the smallest cell size that did not create significant interaction between the diffusion layer and the "open" boundary. Based on this estimate, a 0.6 mm cell was chosen. A comparison of simulation results revealed no difference between the 0.6 mm cell and a 2.4 mm cell. Cells smaller than 0.6 mm were not investigated.

The same conflict must be addressed for mesh sizes. The mesh size is the number of discrete volume elements between the two boundaries. Each volume element is assigned an analyte concentration, which is then allowed to diffuse between elements according to Fick's laws of diffusion. A fine mesh consists of many, small volume elements, allowing the analyte to diffuse short distances more frequently. In the limit of infinitely small mesh size, the model would be equivalent to the continuity of real diffusion. Thus, a fine mesh yields more accurate concentration profiles, but a greater number of mesh elements also requires in more computational time. A compromise can be found by using small mesh elements near the electrode surface, where higher accuracy is needed, and gradually increasing the mesh size with distance from the electrode. For these

simulations, a mesh of 52 elements, with a size of 10 nm near the electrode and growing by factors of 1.2 with increasing distance from the electrode, gave the same results as more refined meshes.

Similarly, the time steps taken by the simulator were chosen as 1 ms to optimize resolution and computational time. Choosing 10 ms time steps made the low intensity ECL peaks irresolvable during a pulsing experiment. The actual time steps taken by the simulation are somewhat random—typically on the order of 1 μs. The value of 1 ms governs the maximum size of the time step, but only directly effects which data points are extracted from the calculation for processing. In fact, the actual time step may not occur at the data points being analyzed. Unless strict conditions are set when the time step is selected, the data points at 1 ms intervals may be an interpolation of the data actually simulated. Such random factors included in the simulation model probably cause variations in the results that are similar to experimental noise.

While the electrochemical processes can be completely addressed by the boundary conditions, the secondary processes that generate ECL are established by the subdomain conditions. For each species in the simulation, the rate expression for its growth or decomposition is assigned. For the annihilation reaction,

$$A^{\bullet -} + A^{\bullet +} \rightarrow A^{*} + A \qquad (2.5)$$

both $A^{\bullet+}$ and $A^{\bullet-}$ must lose concentration equal to the annihilation rate, $k_{ann}[A^{\bullet-}][A^{\bullet+}]$, while A^* and A gain the same amount during each time step. The annihilation rate constant, k_{ann}, was chosen as 2×10^8 $M^{-1}s^{-1}$, based on the value reported for 9,10-diphenylanthracene (DPA).[8] The actual reported value of 2×10^{10} $M^{-1}s^{-1}$ yielded negative concentrations in our simulation. However, Feldberg observed that using $k_{ann} > 10^7$ $M^{-1}s^{-1}$ did not affect the shape of the ECL.[2] The emission rate constant was chosen as $k_{em} = 1.2\times10^8$ s^{-1}, based on the emission rate constant for DPA in methanol.[9]

ECL is typically generated by pulsing the potential of the working electrode between two potentials that are beyond the oxidation and reduction peak potentials of the CV. In our simulation, this is achieved by multiplying each potential by a Heaviside function of a sine function of time. The Heaviside function is zero when the sine function is negative, and it is 1 elsewhere, so the function is periodically switched on and off. Alternate potential pulses can be generated by expressing the applied potential as the sum of both Heaviside functions, and setting their respective sine arguments out of phase from one another. The frequency of the sine waves can be adjusted to vary the pulse width. The current is then calculated from the difference between the diffusive fluxes for each product, and ECL intensity is calculated as

$$I_{ECL} = N_a \Phi_{PL} k_{em} \int [A^*] dV \qquad (2.6)$$

where Φ_f is the fluorescence efficiency and N_a is Avogadro's number.

2.3 Results and Discussion

Alternate pulsing of the applied potential generates faradaic current transients and ECL transients. The current transients shown in Figure 2.1a are of equal height because there are no secondary reactions to deplete the products. Allowing the cation to decompose to a non-electroactive species, using $k_d = 100\ s^{-1}$, as in Figure 2.1b, results in a gradual decay in the height of the current transient. The decay occurs because the charge passed for the potential step in one direction is not reversed for the charge passed in the other direction, since the decomposition product is usually non-electroactive. This is not observed experimentally due to slow instrumental response.

The ECL transients follow a more documented trend, since their effect is visible on instruments. With no decomposition reactions, the ECL intensity is constant for each potential step, giving a maximum intensity of $\sim 5 \times 10^{20}$ photons on each pulse, as shown in Figure 2.2a. However, as with the current, if a decomposition reaction is added, the ECL intensity decreases with each pulse, because there is less analyte within the diffusion layer every time the unstable species is generated. The potential pulses in which the stable radical ion is generated will decay more rapidly (Figure 2.2b, c), because the unstable radical will have partly decomposed before the next pulse can begin, resulting in lower emission. The integrated intensity ratio between the forward and reverse pulses can be plotted as a logarithmic function of the decomposition rate constant to

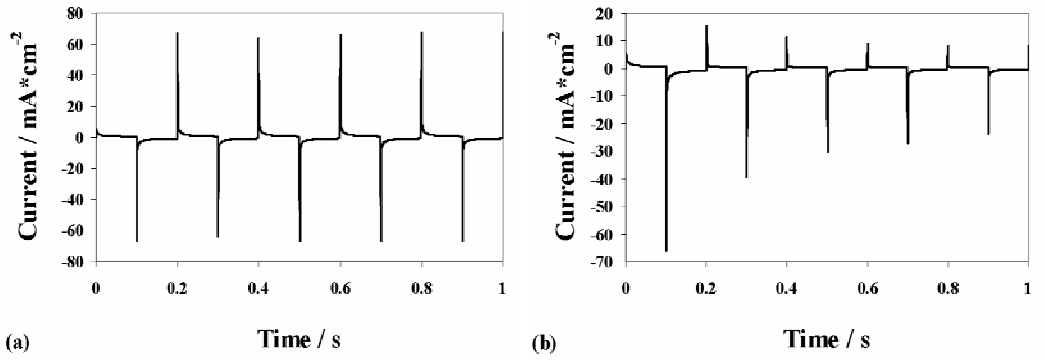

Figure 2.1. Current response to potential pulses alternation between oxidation and reduction for (a) no decomposition and (b) cation decomposition with $k = 100$ s^{-1}.

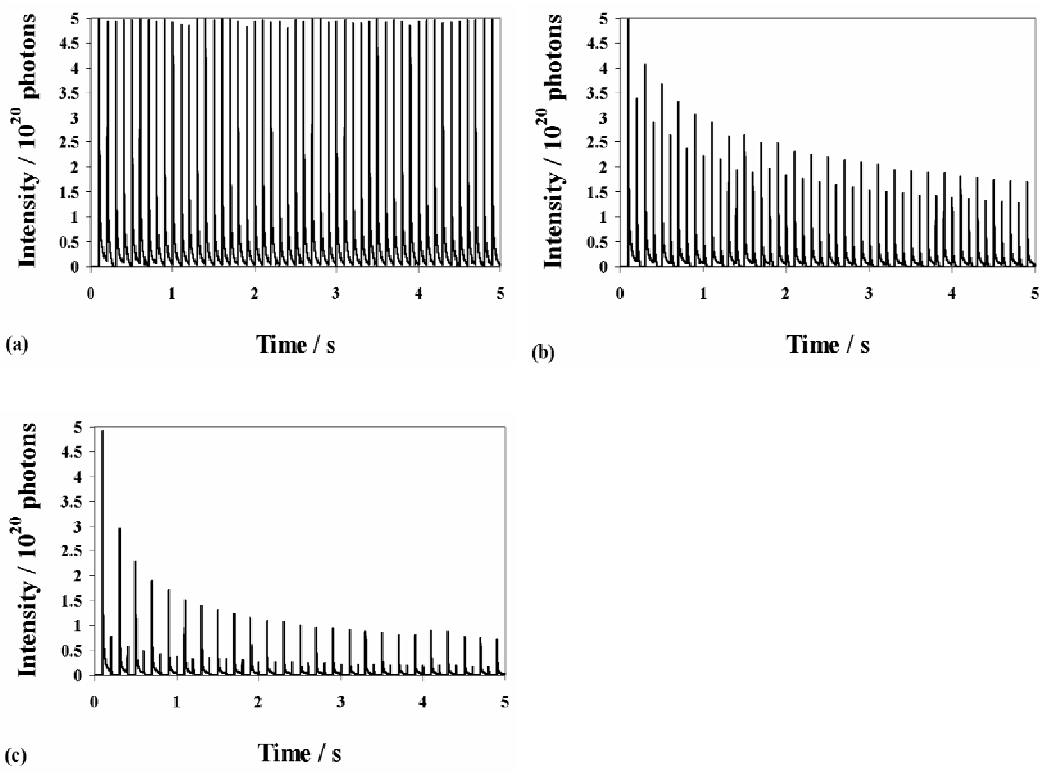

Figure 2.2. ECL transients taken over 5s pulsing between oxidation and reduction at 5 Hz for a simulation with cation decomposition rate of (a) $k = 0$ s^{-1} (b) $k = 10$ s^{-1} (c) $k = 100$ s^{-1}.

generate a working curve, as shown in Figure 2.3. However, the initial pulses are not consistent with the remaining pulses, because the starting conditions for the first pulse are different from those of the subsequent pulses. The result is an intensity ratio that grows before it reaches the constant value described in the earlier paper (Figure 2.4). Therefore, the intensity ratio is only used for pulses obtained after the first 8 cycles (1.6s), at which point, each pulse has the same starting conditions. In addition, due to the randomness inherent in Multiphysics, there is some variation in the intensity ratio with continued cycling, as shown in Figure 2.4. Thus the average of the intensity ratios from 1.6 seconds to 4.8 seconds was used for each point in Figure 2.3, and the error bars come from the standard deviations.

Radical ion quenching of the excited state was included in the model to improve the accuracy of the simulation. These reactions were described using the rate expressions $k_{rq}[A^{\bullet-}][A^*]$ and $k_{rq}[A^{\bullet+}][A^*]$, with $k_{rq} = 2\times10^{10}$ $M^{-1}s^{-1}$. Adding them decreased the average maximum intensity for a 50 cycle simulation from 4.84×10^{20} to 4.71×10^{20} photons, as shown in Figure 2.5.

2.4 Conclusions

COMSOL Multiphysics has been used to simulate a simple ECL experiment using multiple potential pulses. The results observed here agree with previous experimental and simulated data, showing that the program is a viable option for ECL simulations. From this starting point, it is possible to include

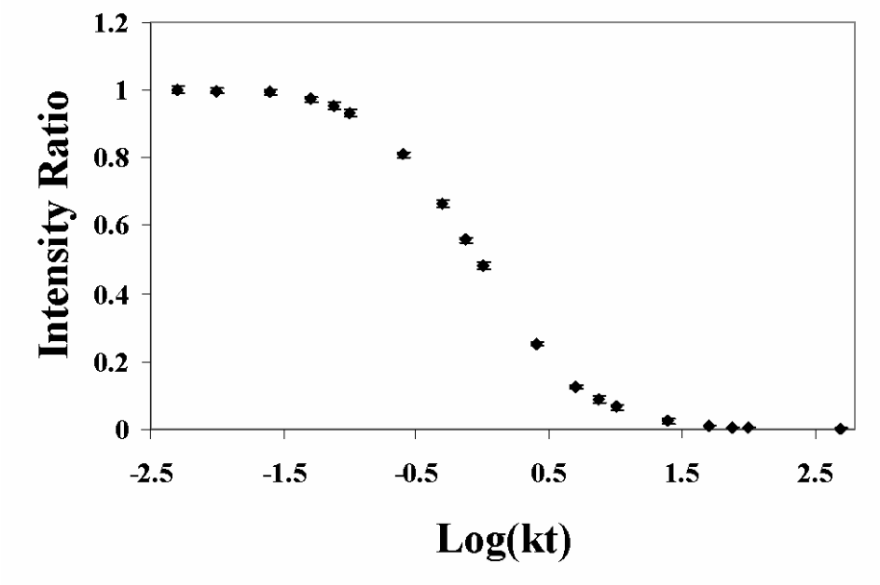

Figure 2.3. Working curve relating the integrated ECL intensity ratio of two consecutive peaks to the cation decomposition rate constant. Ratios are averaged over all cycles from 1.6 s to 4.8 s.

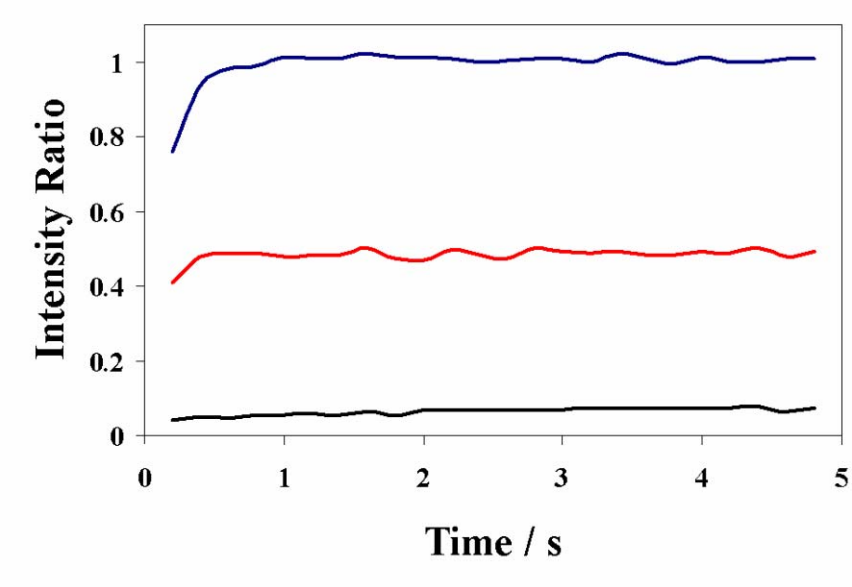

Figure 2.4. Change of integrated intensity ratio of consecutive peaks as a function of time for $k = 0\ s^{-1}$ (blue), $k = 10\ s^{-1}$ (red) $k = 100\ s^{-1}$ (black).

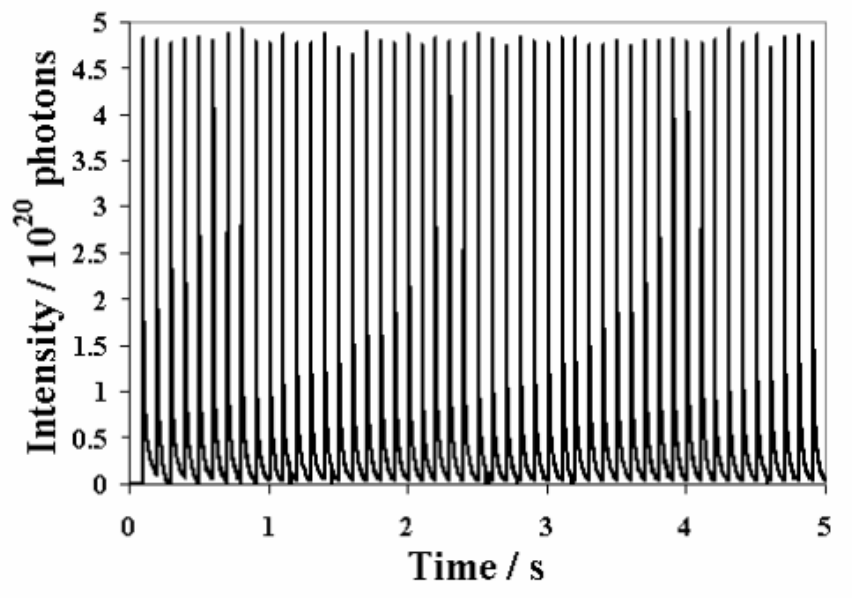

Figure 2.5. ECL transients taken over 5s pulsing between oxidation and reduction at 5 Hz for a simulation including radical ion quenching of the excited state.

other phenomena, such as triplet-triplet annihilation, coreactants, unique cell geometries, and many other variations.

2.5 References

(1) Maloy, J. In *Electrogenerated Chemiluminescence*; Bard, A.; Ed.; Marcel Dekker: New York, NY, **2004**, pp. 101-106.

(2) Feldberg, S. *J. Am. Chem. Soc.* **1966**, *88*, 390.

(3) Feldberg, S. *J. Phys. Chem.* **1966**, *12*, 3928.

(4) Cruser, S.; Bard, A. *J. Am. Chem. Soc.* **1969**, *91*, 267.

(5) (a) Rudolph, M.; Reddy, D.; Feldberg, S. *Anal. Chem.* **1994**, *66*, 589A; (b) Bott, A.; Feldberg, S.; Manfred, R. *Curr. Sep.* **1996**, *15*, 67; (c) Ketter, J.; Forry, S.; Wightman, M.; Feldberg, S. *Electrochem. Solid-State Lett*. **2003**, *7*, E18.

(6) (a) Rudolph, M. *J. Electroanal. Chem.* **2003**,*543,* 23; (b) Ruldolf, M. *J. Electroanal. Chem.* **2004**, *571*, 289; (c) Rudolph, M. *J. Electroanal. Chem.* **2003**, *558*, 171. (d) Rudolph, M. *J. Comp. Chem.* **2005**, *26*, 619; (e) Rudolph, M. *J. Comp. Chem.* **2005**, *26*, 233; (f) Rudolph, M. *J. Comp. Chem.* **2005**, *26*, 1193.

(7) (a) Svir, I.; Oleinick, A.; Klimenko, A. *J. Electroanal. Chem.* **2001**, *513*, 119.

(8) Collinson, M.; Wightman, R.; Paolo, P. *J. Phys. Chem.* **1994**, *98*, 11942.

(9) Boens, N.; Qin, W.; Basarić, N.; Hofkens, J.; Ameloot, M.; Pouget, J.; Lefèvre, J.-P.; Valeur, B.; Gratton, E.; vandeVen, M.; Silva, N.; Engelborghs, Y.; Willaert, K.; Sillen, A.; Rumbles, G.; Phillips, D.; Visser, A.; van Hoek, A.; Lakowicz, J.; Malak, H.; Gryczynski, I.; Szabo, A.; Krajcarski, D.; Tamai, N.; Miura, A. *Anal. Chem.* **2007**, *79*, 2137.

Chapter 3: Electrochemistry, spectroscopy, and electrogenerated chemiluminescence of silole-based chromophores

3.1 Introduction

We report the electrochemistry and electrogenerated chemiluminescence (ECL) of a series of silole (1-silacyclopentadiene) compounds. There have been several studies of silole photoluminescence,[1-5] but chemiluminescence (CL) has only been observed in one instance.[6] There have also only been a few, brief studies of the electrochemistry of siloles, and few siloles are known to exhibit stable radical anions, while none showed stable radical cations.[1,2,7,8] Synthetically, siloles of broad structural diversity have been difficult to synthesize and those most easily obtained from Tamao's cycloreduction protocol[9] generally show poor photoluminescence efficiencies.[10] It was recently observed, however, that judicious structural modifications could achieve high quantum yields from siloles derived via cycloreduction of bis(phenylethynyl)silanes.[11] These recent contributions have made possible the first series of homologous silole chromophores suitable for potential ECL studies. Given the unique molecular orbital properties of siloles, and their resultant applications in electron transport materials,[3,4,12-14] a better understanding of the relationship between the structural

and electrochemical properties of these compounds is of interest, as is ECL in this class of compounds.

Siloles are interesting because of their low LUMO level compared with that of analogous conjugated cyclic compounds, such as furan, pyrrole, thiophene, and cyclopentadiene.[15] The suspected cause is a unique interaction between the π^* orbital of the butadiene moiety with the σ^* orbital of the exocyclic Si-R bond.[15] A narrow energy gap enables oxidation and reduction of a silole within the potential window of the solvent, which is necessary for ECL.[16]

In ECL, an anion and a cation are electrochemically generated and allowed to annihilate. The energy of annihilation is $-\Delta H^o = -\Delta G^o - T\Delta S^o$ ($T\Delta S^o \sim$ 0.1 eV), where ΔG^o is $E^o_{red} - E^o_{ox}$. If ΔH^o of annihilation is sufficient, one of the annihilating pair will be left in an excited state. The simplest reaction scheme is as follows:

$$R + e \rightarrow R^{\bullet -} \quad (2.1)$$

$$R - e \rightarrow R^{\bullet +} \quad (2.2)$$

$$R^{\bullet -} + R^{\bullet +} \rightarrow {}^1R^* + R \quad (2.3)$$

$$R^{\bullet -} + R^{\bullet +} \rightarrow {}^3R^* + R \quad (2.4)$$

$${}^3R^* + {}^3R^* \rightarrow {}^1R^* + R \quad (2.5)$$

Several criteria are important for annihilation ECL. Both the reduction and oxidation must occur within the potential window of the solvent. As

mentioned earlier, the difference between the reduction and oxidation potentials must be greater than the energy of an excited state of one of the reactants. The radical anion and cation must be sufficiently stable to encounter one another before they are consumed by secondary reactions. Even small amounts of water or oxygen can often scavenge enough of the radical ions to prevent ECL, and some radical ions can dimerize or polymerize.[17,18] When generating ECL by pulsing an electrode between potentials for the oxidation and reduction of the substrate, it is often necessary to generate both the oxidized and reduced species in rapid succession so that they can react before scavenging processes become significant.

Recently, a series of highly luminescent (quantum efficiency, Φ_{PL}, as high as 0.60) 2,5-bis(arylethynyl)-substituted siloles were synthesized.[19] These and a similar series of ethylene-substituted siloles (shown in Figure 3.1) form the basis of this study. Though they lack the structural rigidity that appears to minimize internal conversion in ethynyl-substituted siloles,[19] olefinic compounds are less susceptible to polymerization reactions upon reduction.[20] Eliminating such secondary reactions improves ECL stability. However the ethynyl-substituted siloles were consistently more efficient fluorophores and generally exhibited greater radical ion stability than their ethylene-substituted counterparts. With increasing steric protection of the triple bonds, the ethynyl-substituted compounds exhibited increases in both fluorescence efficiency and radical ion stability,

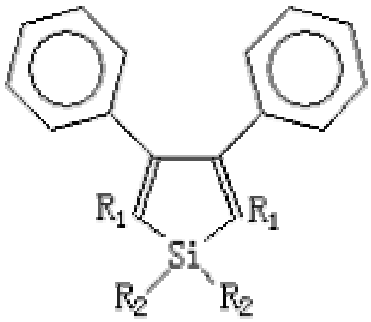

Silole	R_1	R_2	**Silole (cont.)**	R_1	R_2
2a	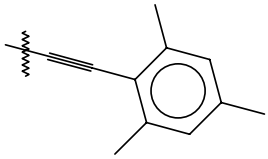	CH_3	**3a**	CH_3	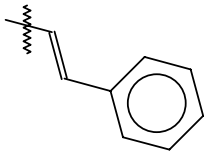
2b	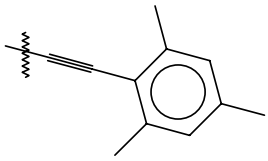	*t*-butyl	**3b**	CH_3	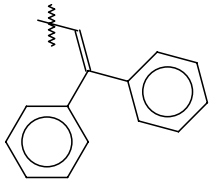
2c	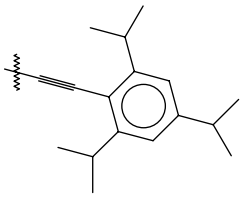	*t*-butyl	**3c**	CH_3	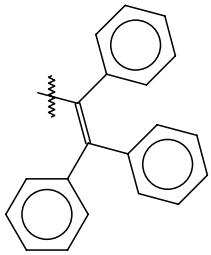

Figure 3.1. Structure and names of each silole compound used.

whereas the ethylene-substituted compounds exhibited decreasing quantum efficiency and radical stability with increasing steric protection. In this paper, we examine the structures of these compounds in an attempt to understand their impact on both their electrochemical and photophysical behavior.

3.2 Experimental

3.2.1 Materials

Anhydrous acetonitrile, benzene, and acetone were obtained from Aldrich (St. Louis, MO) and transferred directly into a helium atmosphere drybox (Vacuum Atmospheres Corp., Hawthorne, CA) without further purification. THF was distilled from sodium and benzophenone under a nitrogen atmosphere and degassed with argon prior to use with Li metal. $ZnCl_2$ was flame-dried under vacuum and stored in a drybox. Tetra-*n*-butylammonium perchlorate (TBAP) was obtained from Fluka and transferred directly into the drybox. All silole compounds except **3b** and **3c** were synthesized as previously described.[1,19]

Bis(diphenylethenyl) silole (3b): A solution of bis(phenylethynyl)dimethylsilane **1** (520 mg, 2.00 mmol) in THF (2.0 mL) was added dropwise into a THF solution of LiNaph (9.4 mL, 0.85 M, 8.00 mmol) under argon. The mixture was stirred for 10 min, then cooled in an ice-salt bath and a solution of $ZnCl_2$ (1.36 g, 10.0 mmol) in THF (10 mL) was added rapidly via cannula. The ice-salt bath was removed and the mixture stirred for 30 min. In a separate dry flask equipped with a H_2O-jacketed condenser was added

$Pd(PPh_3)_4$ (231 mg, 0.20 mmol), THF (5 mL), and 2-bromo-1,1-diphenylethene (1.14 g, 4.40 mmol) under argon. The silole solution was then added into the flask containing Pd via cannula under argon atmosphere. The resulting mixture was heated at 50 °C and monitored by TLC. Upon completion (ca 13 h), the mixture was allowed to cool, poured into half-saturated NH_4Cl solution and extracted with Et_2O (3 x 20 mL). The organic extracts were washed with brine (1 x 50 mL), dried ($MgSO_4$), filtered through silica gel (50% CH_2Cl_2/hexanes elution) and concentrated. Flash chromatography on silica gel (10% CH_2Cl_2/hexanes) provided 582 mg (94%) of the desired compound as a yellow powder. R_f 0.11 (20% CH_2Cl_2/hexanes); ^1H NMR ($CDCl_3$, 400 MHz) δ 7.37-7.28 (m, 10 H), 7.16-7.01 (m, 20 H), 6.54 (s, 2 H), -0.85 (s, 6H); ^{13}C NMR ($CDCl_3$, 100 MHz) δ 158.5, 143.7, 143.4, 141.45, 141.37, 139.1, 132.0, 130.0, 129.9, 128.6, 127.9, 127.8, 127.6, 127.3, 126.9, 126.8, -4.2; HRMS m/z calcd for $C_{46}H_{38}Si$ [M^+]: 618.2743, found: 618.2743.

Bis(triphenylethenyl) silole (3c): A solution of bis(phenylethynyl)dimethylsilane **1** (1.302 g, 5.00 mmol) in THF (5.0 mL) was added dropwise into a THF solution of LiNaph (24 mL, 0.85 M, 25.0 mmol) under argon. The mixture was stirred for 10 min, then cooled in an ice-salt bath, and a solution of $ZnCl_2$ (3.41 g, 25.0 mmol) in THF (25 mL) was added rapidly via cannula. The ice-salt bath was removed and the mixture stirred for 30 min. In a separate dry flask equipped with a H_2O-jacketed condenser was added

$Pd(PPh_3)_4$ (578 mg, 0.50 mmol), THF (12 mL), and 1-bromo-1,2,2-triphenylethene (3.69 g, 11.0 mmol) under argon. The silole solution was then added into the flask containing Pd via cannula under argon atmosphere. The resulting mixture was heated at 40 °C and monitored by TLC. Upon completion (ca 12 h), the mixture was allowed to cool, poured into hexanes (ca 150 mL), filtered through silica gel (30% CH_2Cl_2/hexanes elution) and concentrated. The crude material was recrystallized three times sequentially from hot ^{i}PrOH/hexanes to give 3.21 g (83%) of the desired compound as a yellow powder. Analysis of the ^{1}H NMR spectrum at variable temperatures suggests that the compound exists as a mixture of rotational isomers. Two crystallographically unique molecules were identified in the unit cell by x-ray analysis. ^{1}H NMR ($CDCl_3$, 400 MHz) δ 7.29-6.48 (m, 40 H), -0.23 (s, 6H), -0.27 (s, 6H), -0.34 (s, 6H); ^{13} C NMR ($CDCl_3$, 100 MHz) δ 155.6, 154.7, 144.9, 144.5, 144.3, 144.1, 144.0, 143.9, 143.7, 143.5, 143.4, 140.1, 139.5, 139.2, 139.1, 138.7, 138.6, 138.4, 131.6, 131.5, 131.0, 130.8, 130.7, 130.5, 128.7, 127.45, 127.40, 127.2, 127.0, 126.6, 126.2, 126.0, 125.9, 125.5, 125.4, -1.2. -2.9. -5.1; HRMS m/z calcd for $C_{58}H_{46}Si$ [M^+]: 770.3369, found: 770.3376.

3.2.2 Characterization

Scheme 2.1 describes the synthesis of 3b and 3c. The procedure generates 3b in 94% yield, and 3c in 83% yield. X-ray crystal structures (Figure 3.2) confirm the structures of these two compounds, and they show the orientation of

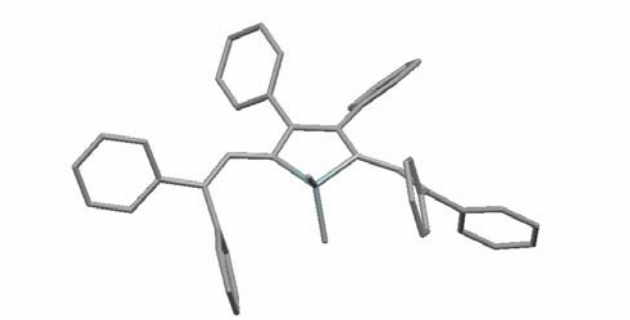

(a)

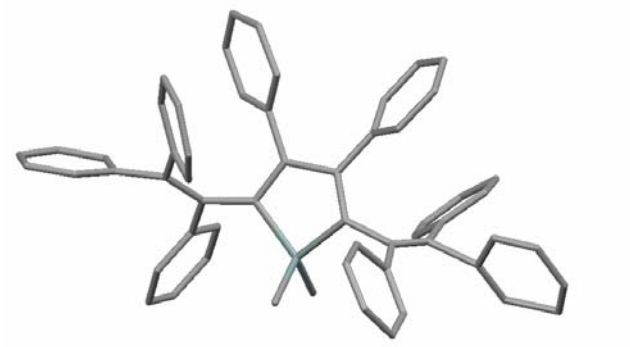

(b)

Figure 3.2. X-ray crystal structures of (a) **3b** and (b) **3c**.

the phenyl substituents with respect to the silole moiety in the solid state.

Scheme 3.1. Synthetic route for siloles.

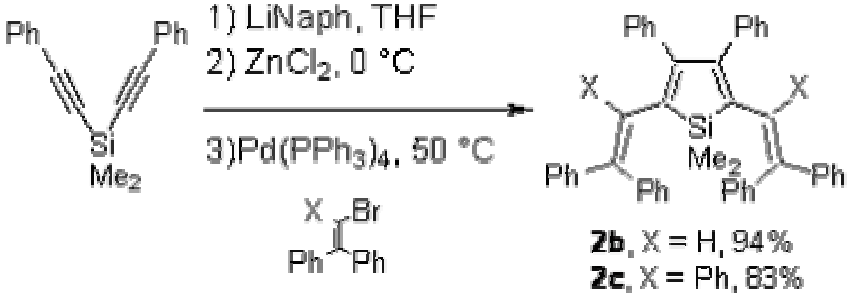

The electrochemical cell consisted of a coiled, Pt wire as a counter electrode, a Ag wire as a quasi-reference electrode, and a 0.5 mm diameter Pt disk inlaid in glass. Fast scan experiments (scan rate, ν=20 V/s to 2000 V/s) were performed with a 25 μm Pt disk inlaid in glass. At the end of an experiment, the Ag wire was calibrated with ferrocene (0.342 V vs SCE).[21] Before each experiment, the working electrode was polished on a felt pad with 0.3 μm alumina (Buehler, Ltd., Lake Bluff, IL) before being sonicated in DI water and then ethanol for one minute, each. The electrode was then rinsed with acetone and transferred into the drybox. For ECL experiments, the working electrode was a ~2 mm Pt disk bent at a 90˚ angle (J-type electrode), so that the disk faced the detector.

For electrochemical experiments, a 1 mM silole solution in 1:1 acetonitrile/benzene was prepared, and the solution was made 0.1 M in TBAP, the supporting electrolyte. All solutions were prepared inside of the drybox. For measurements made outside of the box, the electrochemical cell was closed with a

Teflon cap that had a rubber o-ring to form an air-tight seal. Stainless steel rods driven through the cap formed the electrode connections. Cyclic voltammograms were obtained on a CH Instruments Model 660 Electrochemical Workstation (Austin, TX).

For photophysical characterization, various concentrations of silole were prepared in 1:1 benzene/acetonitrile in a 1 cm quartz cell. Electronic absorption spectra were collected on a DU 640 spectrophotometer (Beckman, Fullerton, CA). Fluorescence spectra were collected on a QuantaMaster Spectrofluorimeter (Photon Technology International, Birmingham, NJ).

Digital simulations of cyclic voltammograms performed with the DigiElch software package[22] were used to investigate the mechanisms of the electrochemical processes. The uncompensated resistance and capacitance were determined by performing a potential step in the relevant solvent system in a region where faradaic reactions did not occur and using the potential step equations for the analogous RC circuit. Diffusion coefficients for each species were determined from potential steps to a diffusion-limited region and application of the Cottrell equation. For compounds that did not show simple, one-electron behavior, the diffusion coefficient (D) was approximated as 9×10^{-6} cm^2/s, and adjusted to fit the data. Usually, no adjustment was necessary, as the value for all siloles was near 10^{-5} cm^2/s. The electrode surface area used in the simulations

was determined by a potential step experiment performed in a solution of acetonitrile and ferrocene ($D = 1.2 \times 10^{-5}$ cm^2/s).[23]

To generate ECL, the working electrode was pulsed between the oxidation and reduction potentials of the silole with a pulse width of 0.1 s. For the ECL spectra, the potentiostat was a Princeton Applied Research Model 173 Potentiostat/Galvanostat used in conjunction with a Princeton Applied Research Model 175 Universal Programmer (Trenton, NJ), and the detector was a CH 260 charge-coupled device (CCD) camera from Photometrics (Tucson, AZ). The camera was cooled with liquid nitrogen between -100 to -120˚C. The spectra were calibrated with a Hg lamp after each measurement. ECL transients were obtained by excitation with an Eco Chemie Autolab potentiostat (The Netherlands) connected to a photomultiplier tube (PMT, Hamamatsu R4220p, Japan). The PMT was supplied with -750 V from a high voltage power supply series 225 (Bertan High Voltage Corp., Hucksville, NY).

ECL quantum efficiencies were determined by comparing the peak currents of the largest ECL transients collected during potential pulsing to the transients of DPA. These measurements are only accurate to about an order of magnitude.

3.3 Results and Discussion

3.3.1 Electrochemistry

Ethynyl–substituted siloles. -A summary of the electrochemical data for all siloles is given in Table 3.1, and cyclic voltammograms of the ethynyl-substituted siloles are shown in Figure 3.3. Reductions of **2c** and **2b**, at -1.80 and -1.76 V vs SCE, respectively, are one-electron, chemically reversible processes. However, the separation between the forward and reverse peaks (ΔE_p) for the reduction of 2c is larger than the 59 mV expected for a nernstian reaction[24] (e.g. ΔE_p = 90 mV at v = 200 mV/s). The uncompensated resistance, R_u, in this cell for the benzene/MeCN solution used was ca. 2 kΩ, which increases the apparent ΔE_p in the CVs. We also examined the CV of ferrocene (Fc), which shows a nernstian, one-electron oxidation at the scan rates used (50 mV/s to 10 V/s). Simulations of these CVs with this R_u-value for Fc over the range of scan rates fit very well. However, even with R_u included in the simulations, the observed ΔE_p for the reduction of **2c** was significantly larger than that predicted for a nernstian reaction, suggesting that slow heterogeneous electron transfer (HET) effects are significant with **2c**. Agreement between the experimental and simulated ΔE_p-values for **2c** was only obtained with a heterogeneous reaction rate constant, k^o, of 0.025 cm/s (Figure 3.4). This contrasts with the results for **2b**, where nernstian behavior was seen (i.e. k^o is so large that HET does not compete with diffusional rates). Slow HET kinetics usually indicates a large reorganization energy for the

Table 3.1. Electrochemical data for all siloles. All experiments were performed at a ~0.5 mm Pt disk electrode in 1:1 Benzene/MeCN with 0.1 M TBAP as the supporting electrolyte.

Silole	**E_{red} / V vs SCE**[a]	**E_{ox} / V vs SCE**[a]	**ΔE**	**D / 10^{-6} cm^2/s**	**k^o / cm/s**[h]	**red. mech.**	**ox. mech.**
2a	-1.66[b] -1.68[c] -1.86[d]	0.99[f]	2.85	~9	0.05[g]	complex; Rev. at ν > 1 V/s	Irrev. 2 e
2b	-1.76	1.01	2.77	10	>d.c[i]	Rev.	ECE k_1 = 3 s^{-1}
2c	-1.80	1.05	2.84	8.2	0.025	Rev.	ECE k_1 = 1 s^{-1}
3a	-1.76	0.83	2.59	18	>d.c[i]	Rev.	ECE k_1 = 4 s^{-1}
3b	-1.82	0.86, 0.95[e]	2.70	12	0.05	Rev.	EEC k_1 = 100 s^{-1}
3c	-2.03[e]	0.93[f]	2.97	~9	Unk.[j]	Unk.	Irrev. 2 e

[a] $E_{1/2} = (E_{p,c} + E_{p,a})/2$, except where otherwise specified.
[b] Peak potential of prewave.
[c] $E_{1/2}$ for the prewave at high scan rate, when it shows diffusional behavior.
[d] $E_{1/2}$ for the diffusion wave that follows the prewave. ΔE_p for this wave is 140 mV.
[e] Process is too complicated to measure $E_{1/2}$ in conventional ways, so it was estimated using the value required to make the simulated data fit.
[f] Process is too fast to see reverse wave; peak potential was estimated as $E_{3/4}$ of the forward wave.
[g] Determined at high scan rate, when adsorption peak behaved like a diffusional wave.
[h] Heterogeneous rate constant for reduction reaction.
[i] The heterogeneous electron transfer was faster than diffusion control (d.c.) at the highest scan rates employed (> 1 cm/s).[24]
[j] Irreversibility of the cyclic voltammogram prevents the use of ΔE_p to determine k^o.

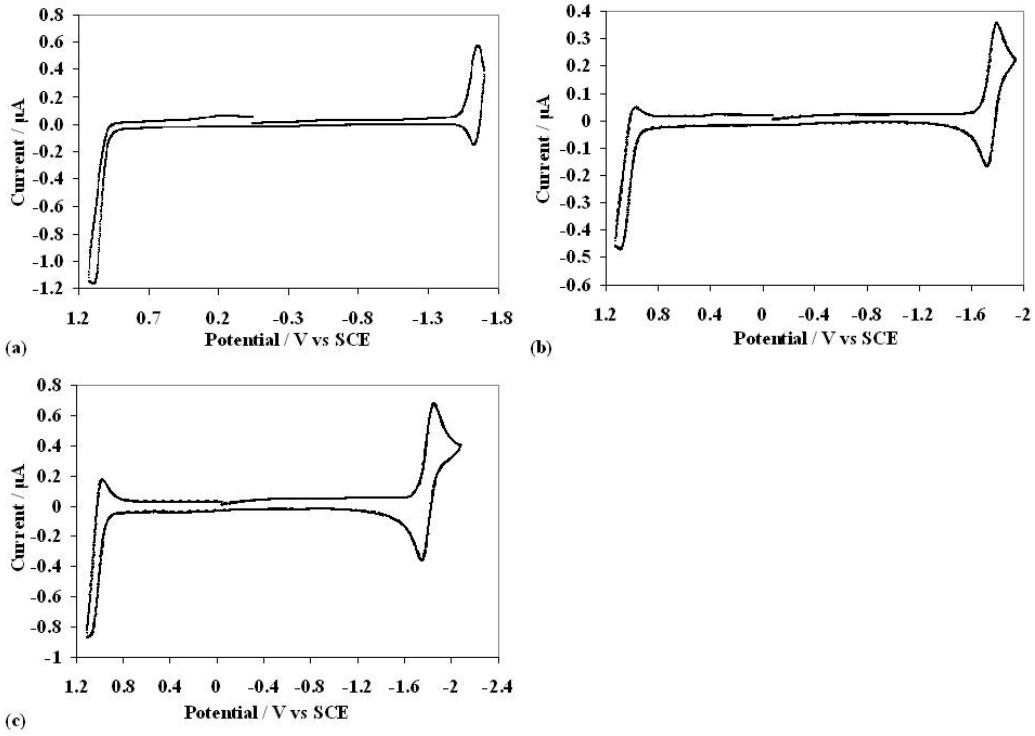

Figure 3.3. Cyclic voltammograms of 1 mM (a) **2a**, (b) **2b**, and (c) **2c** in 1:1 C_6H_6/MeCN with 0.1 M TBAP as the supporting electrolyte. Scans were made at 0.2 V/s.

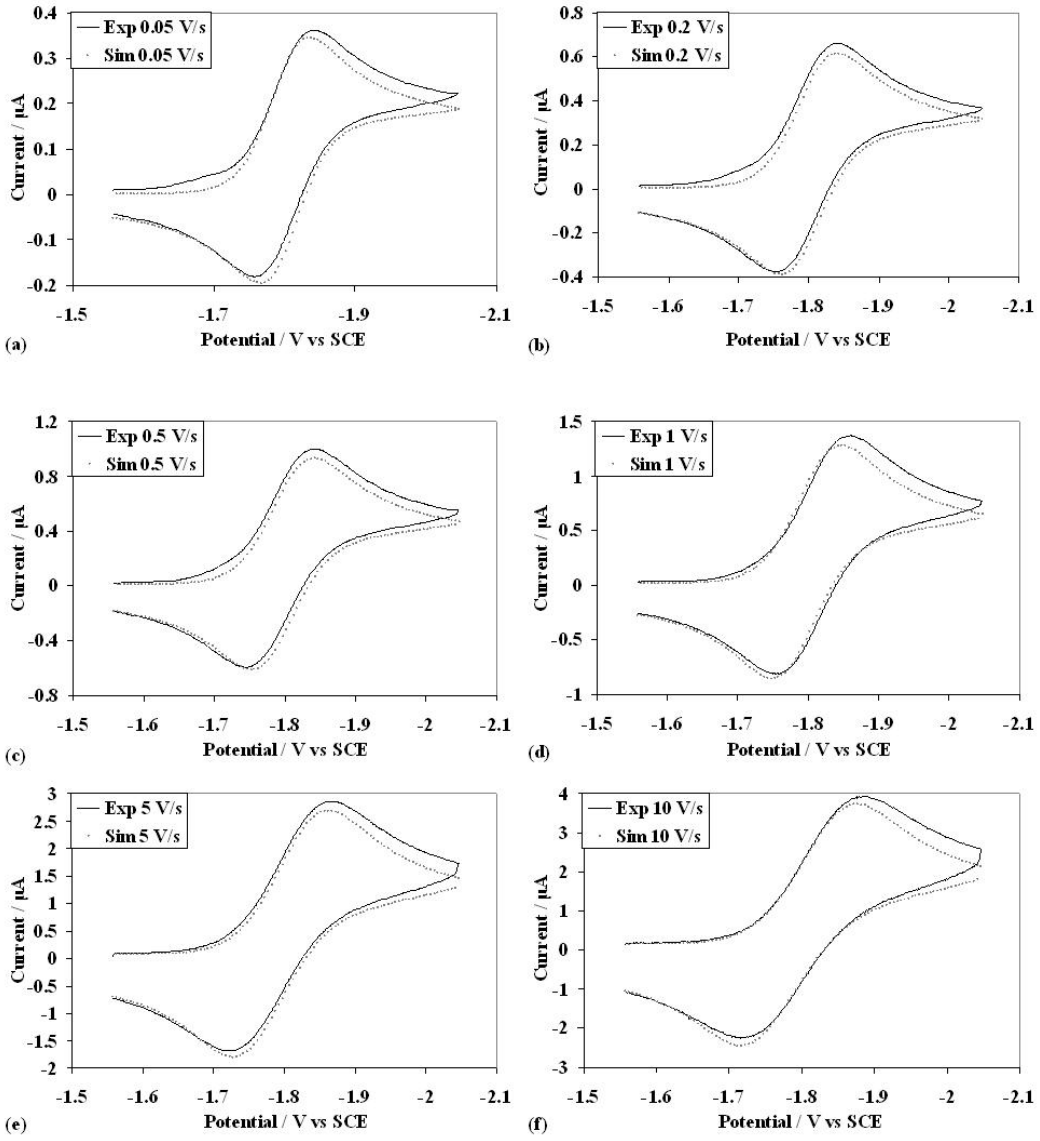

Figure 3.4. Comparison between simulated and experimental data for **2c** at scan rates of (a) 0.05, (b) 0.2, (c) 0.5, (d) 1, (e) 5, and (f) 10 V/s. The simulation model is a one-electron, reversible reaction with k^o = 0.025 cm/s.

molecule or the solvent. Organic compounds are often only weakly solvated and have very similar structures before and after the electron transfer reaction; thus they show fast HET.[25] However, **2c** is the most sterically crowded of this group of compounds, with isopropyl groups on the phenyl of the R1 substituents, which could lead to significant reorganization of the molecule on electron transfer.

Attempts to simulate the CV of **2c** by adding homogeneous chemical reactions to the model, while leaving k^o large were unsuccessful. For example a C_rE mechanism, in which a first order, reversible process precedes the electron transfer, as shown in equations (6) and (7).

$$A \rightleftharpoons B \tag{2.6}$$

$$B + e \rightarrow C \tag{2.7}$$

The above reactions could simulate intramolecular rotations of the molecule that occur prior to electron transfer. This mechanism was tested for various homogeneous rate constants for equation (6), with a fixed equilibrium constant. However, the predicted ΔE_p values for all rate constants studied in the simulations were less than that of the experimental data. For a small homogeneous rate constant, the voltammogram exhibited nernstian behavior, and for a sufficiently large rate constant, the forward peak appeared to flatten, while the ΔE_p remained unchanged. This shape change is not reflected in the experimental data, so it indicates an upper limit to practical simulations. The other possibility studied was

the EC_r mechanism, in which a reversible homogeneous reaction follows the electrochemical step. In this case, simulations were made with the homogenous rate constant held constant, while the equilibrium constant was varied. Again, the large ΔE_p was not observed. The voltammogram appeared nernstian when the equilibrium constant was small. When it was large, the voltammogram lost its reversibility, indicating an upper limit to practical equilibrium constants. Thus we describe the large ΔE_p in terms of slow HET kinetics.

The reduction of **2a** at v>500 mV/s results in a diffusion controlled wave with a k^o of about 0.05 cm/s occurring at –1.68 V vs. SCE. This wave shows chemically reversible behavior when the scan is reversed before –1.8 V (Figure 3.5). Upon scanning to more negative potentials, a second wave appears at about –1.86 V, and the anodic reversal wave of the earlier wave disappears. This effect appears to be associated with formation of some type of blocking film on the electrode, as can be seen from voltammograms taken at a 25 μm diameter Pt ultramicroelectrode (UME) (Figure 3.6). At low scan rates, where a typical steady state voltammogram would show a diffusion-limited plateau, the steady state current of **2a** drops when a blocking layer is formed, but recovers partially on a reverse scan. Presumably the film formation is a time-dependent process and rapid scans can be made before filming becomes significant. Resolving the actual mechanism of this complex process will require further study.

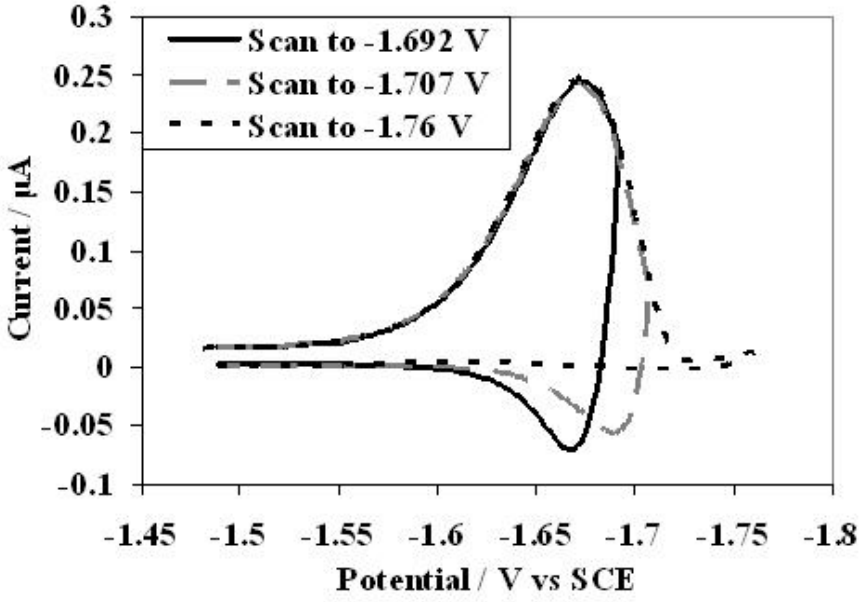

Figure 3.5. The reduction of **2a** at 50 mV/s for various potential scan lengths. The irreversibility at longer potential scans indicates the formation of a blocking film.

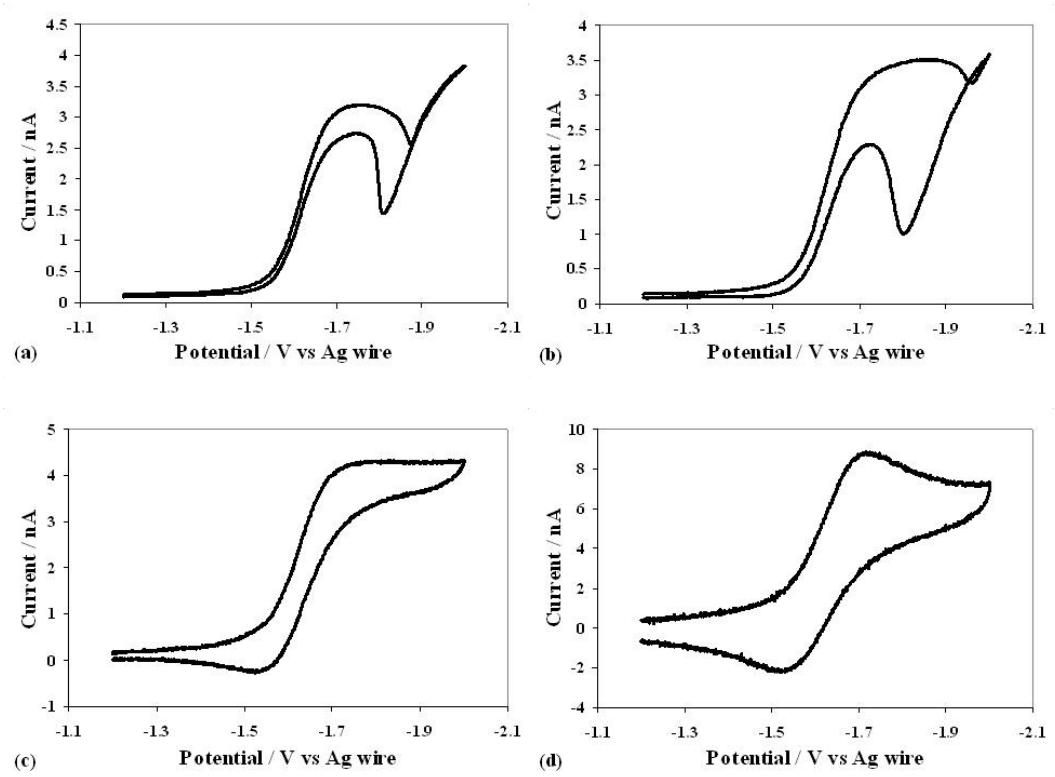

Figure 3.6. Cyclic voltammograms of **2c** performed at a 25 μm electrode scanned at (a) 0.01 V/s, (b) 0.05 V/s, (c) 0.5 V/s, and (c) 5 V/s. The sudden decrease in steady-state current at slow scan rates is attributed to an unstable blocking layer that forms during reduction.

The oxidations of **2a**, **2b**, and **2c** show irreversibility that is characteristic of radical cation instability (Figure 3.3). The anodic waves are also significantly larger (about twice that of the corresponding initial reduction waves of the radical anions) suggesting further electron transfer processes, i.e. ECE reaction sequences.[26] Simulations are consistent with **2b** and **2c** following ECEC mechanisms, with the first oxidations occurring about 1.01 and 1.05 V vs SCE, respectively (Figure 3.7). The potential for the second oxidation step for both of these compounds is unknown, but in both cases, the second wave is indistinguishable from the first, which indicates that its potential is more negative than that of the first oxidation. Since this second wave is not involved in the ECL process, it was not investigated further. The following reactions for **2b** and **2c** were taken as first-order decompositions with rate constants, k_f of 0.5 s^{-1}, and 3 s^{-1}, respectively. In both cases, this homogeneous process could be the reaction of adventitious water with the radical cation (including higher order kinetics to account for this may improve the accuracy of the simulation, but introduces more parameters than are useful to estimate). The oxidation of **2a** was not simulated, as it showed no chemical reversibility for scan rates up to 2000 V/s, signaling a much faster decomposition of its radical cation. Comparison to the reduction wave peak height at 10 V/s suggests that the oxidation is a two-electron process.

The kf-values for decomposition of the radial cation follow the trend **2a** >> **2b** > **2c**, suggesting that blocking of reactive sites, such as the triple-bonds, is

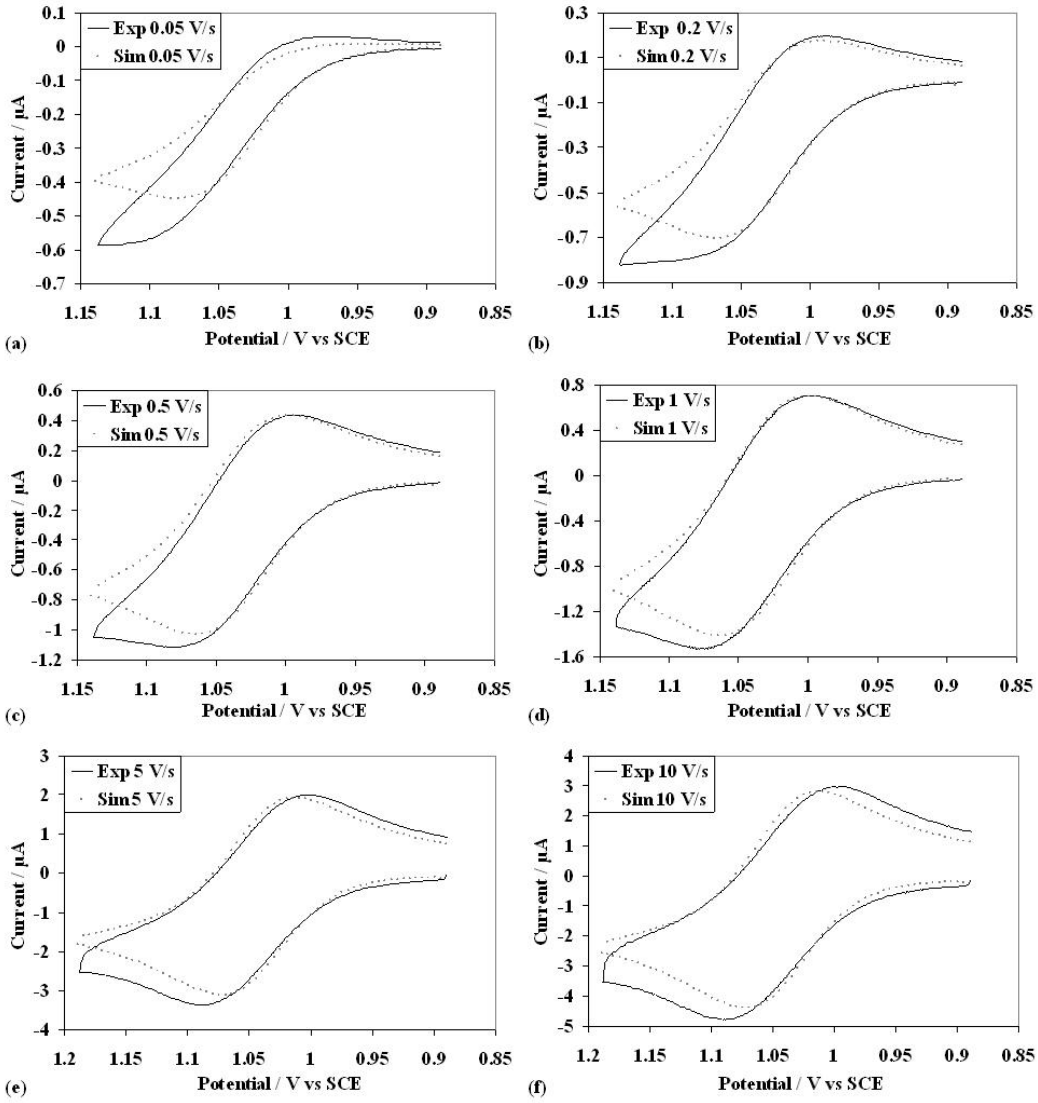

Figure 3.7. Comparison between simulated and experimental oxidation of **2c** at (a) 0.05, (b) 0.2, (c) 0.5, (d) 1, (e) 5, and (f) 10 V/s. The model for these simulations was an ECEC reaction with E_1 = 1.05 V vs SCE, E_2 slightly more negative, $k_1 = 0.5\ s^{-1}$, and $k_2 = 10\ s^{-1}$.

important. In **2b** and **2c**, the large 2,5-substituents and the t-butyl groups on the silicon protect the triple bonds in the molecule from intermolecular reactions. The isopropyl groups on the phenyls are more protective than the methyls. The much higher reactivity of **2a** compared with **2b** suggests that the R2 substituents on the Si are also important.

Ethylene–substituted siloles. – Compounds **3a**, **3b** and **3c** reduce at about the same potentials as the ethynyl-substituted compounds. Interestingly, reduction of the ethylene-substituted siloles becomes more difficult as the number of phenyl groups attached to the ethylenes increases (Table 3.1 and Figure 3.8). This can be ascribed to a decrease in the conjugation of the phenyls with the remainder of the molecule because of steric interactions forcing the phenyls out of the molecular plane (Figure 3.1). To investigate further, quality crystals of **3b** and **3c** were obtained and analyzed by X-ray diffraction analysis. Indeed, the C2/C5-substituents of **3b** were rotated out-of-plane with the silole ring, thus reducing electronic communication along the chromophore backbone (average dihedral angle = 38°). Consistent with the electrochemistry and electronic absorption data (vide infra), the substituents on **3c** showed average dihedral angles of 55° explaining the manifestation of even further reduced electronic communication.

Of the ethylene-substituted series, **3c** is the most difficult to reduce ($E_{1/2} \approx$ -2.03 V vs SCE), probably because the interaction of the 2,5-phenyl groups on the triphenyethylene substituents forces the phenyls to rotate out of the plane of

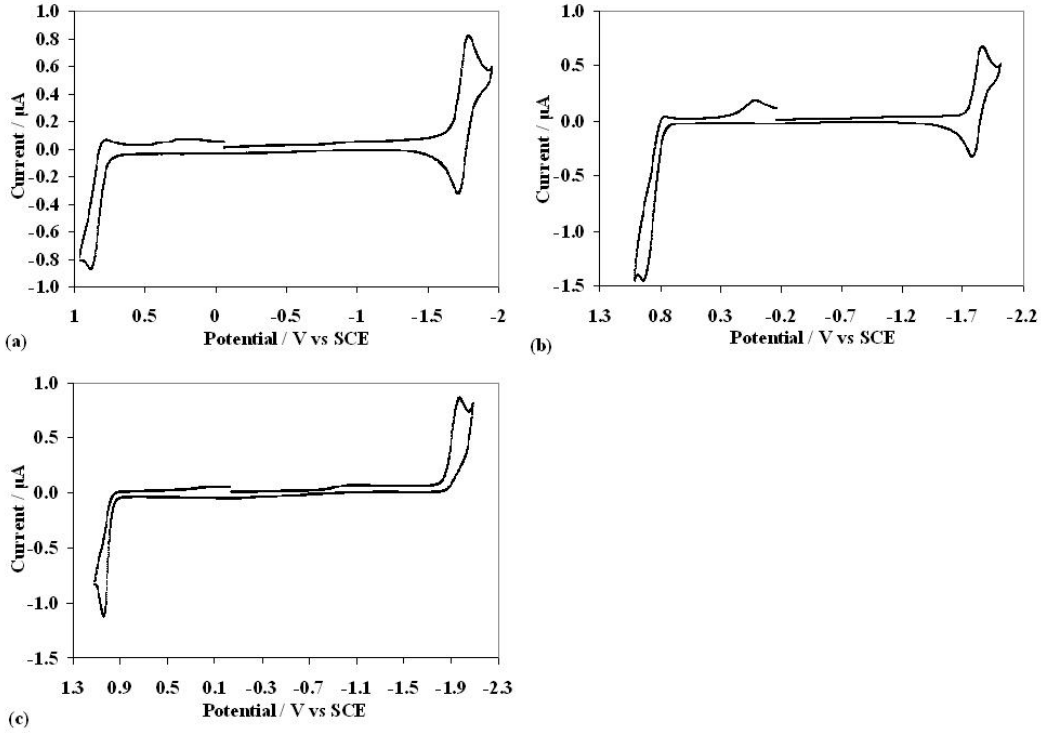

Figure 3.8. Cyclic voltammograms of 1 mM (a) **3a**, (b) **3b**, and (c) **3c** in 1:1 C_6H_6/MeCN with 0.1 M TBAP as the supporting electrolyte. Scans were made at 0.2 V/s.

conjugation with the silole moiety. This illustrates the importance of the silole moiety in the conjugation of these compounds. Reduction of the **3a** is the easiest, occurring at -1.76 V vs SCE, as a reversible, one-electron process with fast heterogeneous kinetics. The reduction of **3b** is slightly more difficult (-1.82 V vs SCE), again because of disrupted conjugation. A k^o of 0.05 cm/s was required to match the simulated data to the experimental ΔE_p at high scan rates.

The reduction of 3c is chemically irreversible at low scan rates (50 mV/s), but shows increasingly reversible behavior as the scan rate is increased (up to 10 V/s). The value of $i_{p,c}/v^{1/2}$, where $i_{p,c}$ is the cathodic peak current, decreases as the scan rate increases and becomes the one-electron value (based on the diffusion coefficients of the more well-behaved siloles) only for v> 2 V/s (Figure 3.9). This behavior suggests an ECE-mechanism.[26] However the absence of any anodic wave at low scan rates suggests that an irreversible homogeneous reaction also follows the second electron transfer, so the mechanism is actually ECEC:

$$A + e \rightarrow B \qquad (2.8)$$

$$B \rightarrow C \qquad (2.9)$$

$$C + e \rightarrow D \qquad (2.10)$$

$$D \rightarrow F \qquad (2.11)$$

We carried out simulations based on this mechanism assuming both (9) and (11) are first order reactions. The closest fit to the experimental data was obtained with $E_8^o = E_{10}^o$ = -2.03 V vs SCE and k^o = 0.015 cm/s for both electron

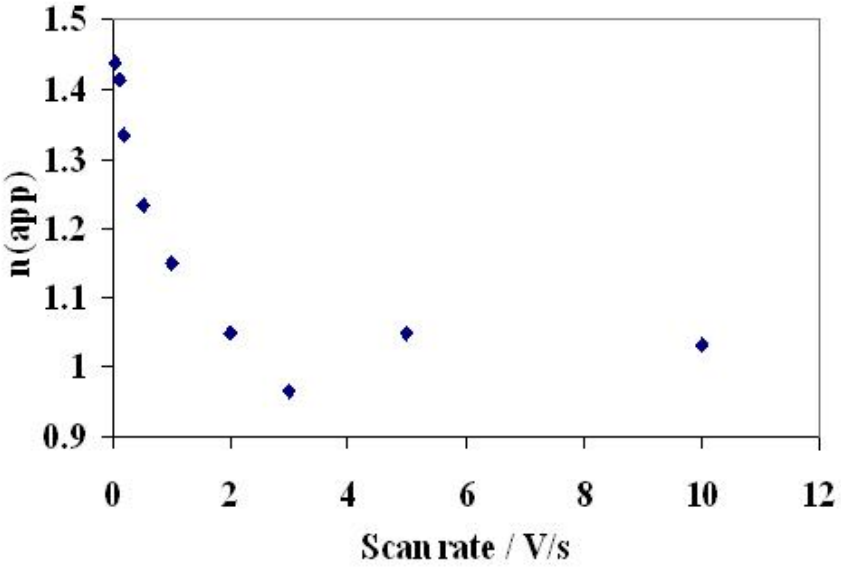

Figure 3.9. A plot of the apparent number of electrons versus scan rate for **3c.**

transfers, k_9 = 3 s^{-1} and k_{11} = 0.5 s^{-1}. However even this best fit showed considerable deviation from the experimental data (Figure 3.10), largely because at v > 500 mV/s there is additional cathodic current, perhaps caused by a small amount of adsorption of starting material or intermediates, just beyond the reduction peak. Clearly, a fuller discussion of the reaction mechanism will require additional study in different solvents.

The oxidation waves of ethylene-substituted siloles at v < 200 mV/s are chemically irreversible, signaling a lower stability of the radical cations. In all cases $i_{p,a}$ is larger than that of the initial reduction wave, indicating additional electron transfer reactions. The oxidation of **3a** is an ECE reaction, with the first oxidation at 0.83 V vs SCE, and k_f = 4 s^{-1} for the following reaction. Again, the second oxidation occurs at a potential negative of the first oxidation (Figure 3.11). The oxidation of **3b** appears to be an EEC mechanism, with two distinguishable waves at E_1 = 0.86 V vs SCE and E_2 = 0.95 V, and k_f = 100 s^{-1} for the following reaction. The simulations (Figure 3.12) are only marginal, largely because of a third oxidation step that occurs slightly positive of the first two that adds to the forward anodic peak current. However, the general behavior of the waves fits an EEC mechanism better than others, like ECE. The EEC nature of the oxidation of **3b** suggests that it can be considered as primarily involving removal of electrons from the 2,5-substituents rather than from a common orbital shared between the substituents and the silole ring, with only a weak interaction between the

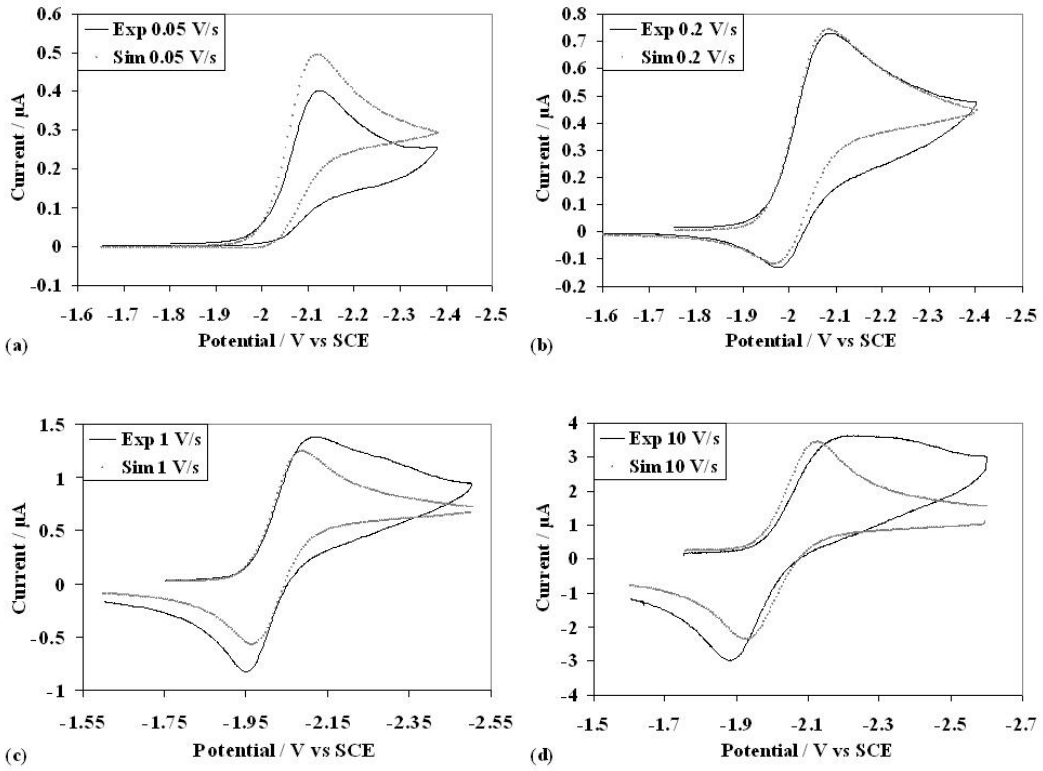

Figure 3.10. Simulated and experimental **3c** reduction data taken at (a) 0.05, (b) 0.2, (c) 1, (d) 10 V/s. The simulation model is an ECEC reaction with $E_1 = E_2 =$ -2.03 V vs SCE, $k_1 = 3\ s^{-1}$, $k_2 = 0.5\ s^{-1}$, and $k^o = 0.015$ cm/s.

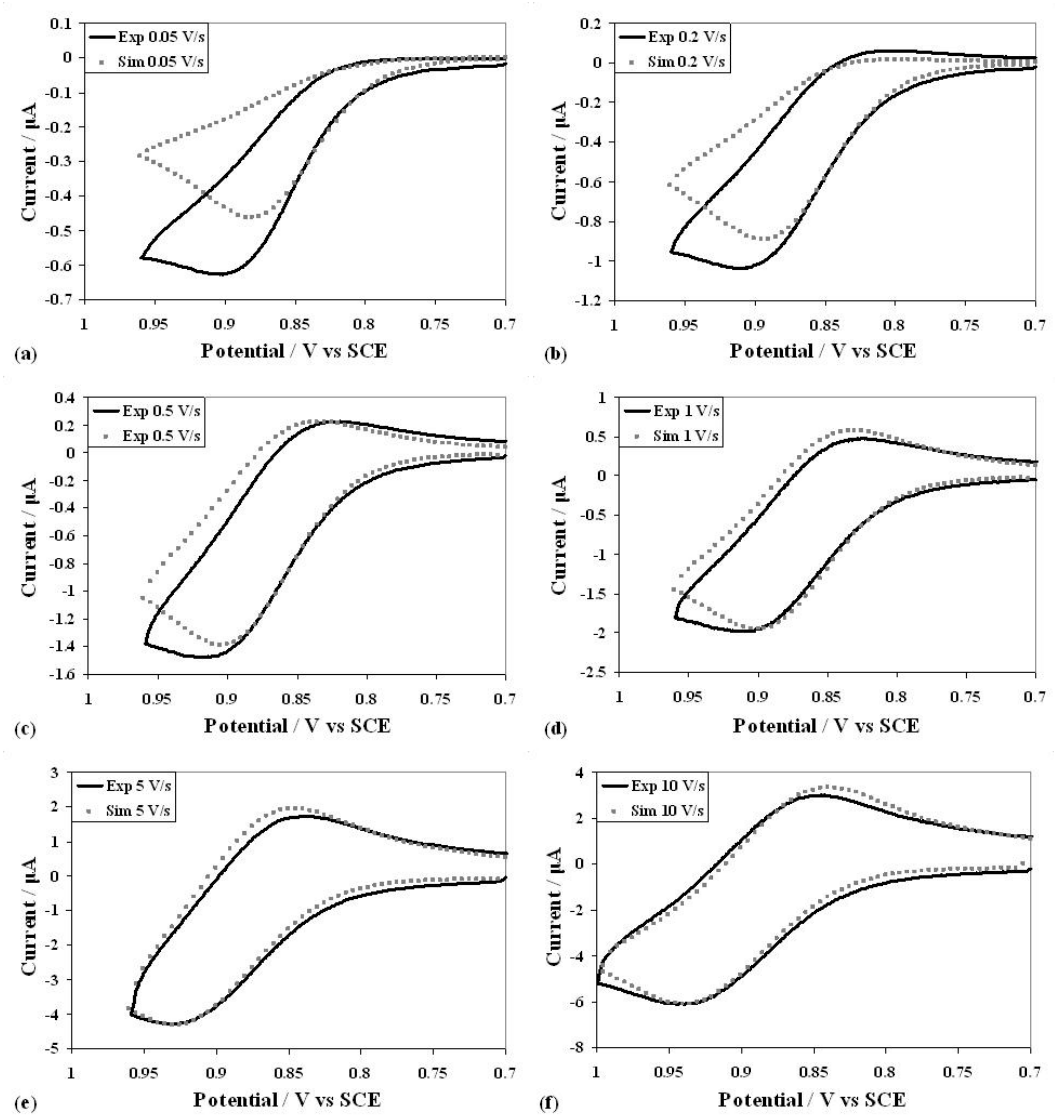

Figure 3.11. Simulated and experimental data for **3a** at scan rates of (a) 0.05, (b) 0.2, (c) 0.5, (d) 1, (e) 5, and (f) 10 V/s. The simulation model is an ECE reaction with E_1 = -1.76 V vs SCE, k^o = 0.05 cm/s, and k_1 = 4 s^{-1}.

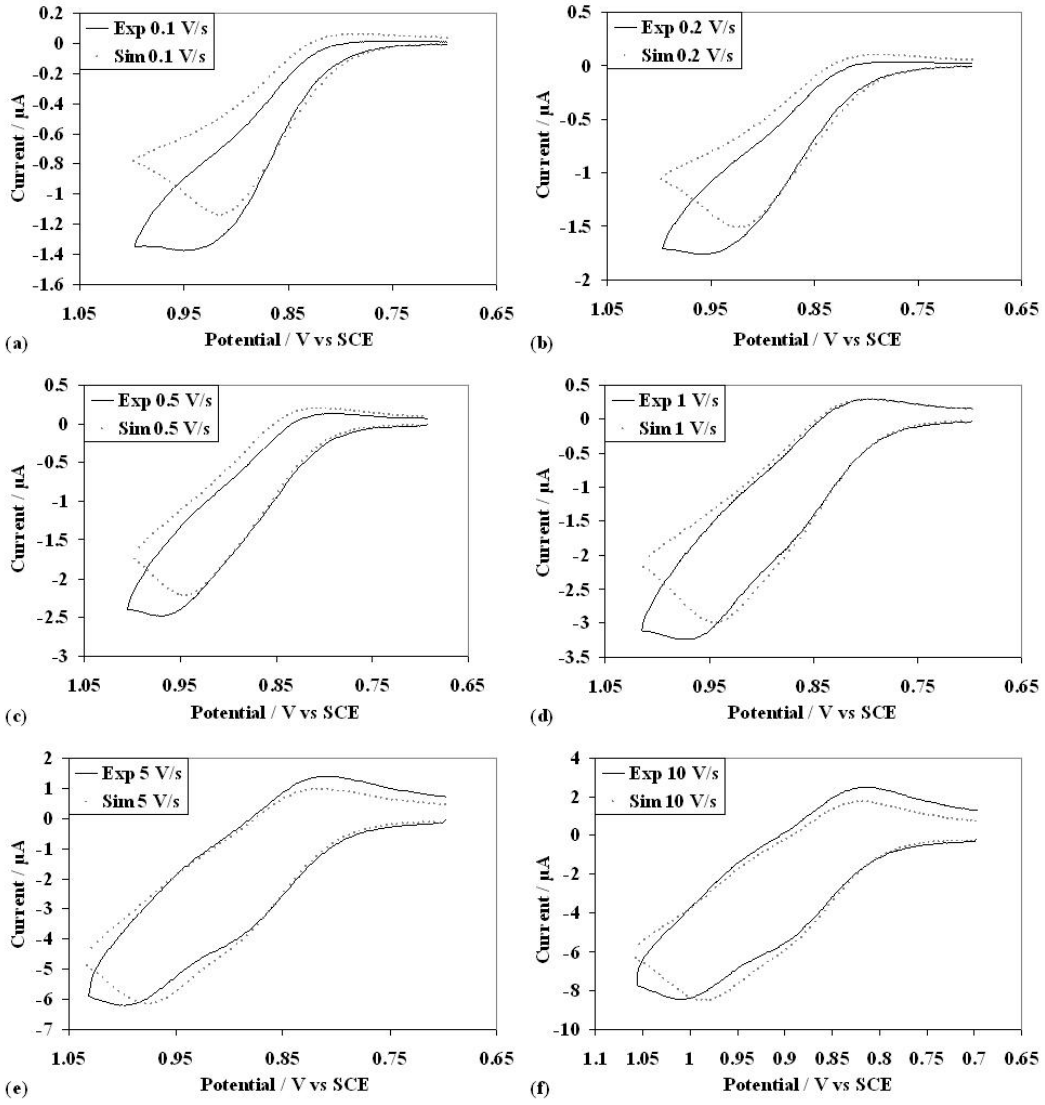

Figure 3.12. Simulated and experimental data for the oxidation of 3b at (a) 0.1, (b) 0.2, (c) 0.5, (d) 1, (e) 5, (f) 10 V/s. The simulation model is an EEC reaction with E_1 = 0.86 V vs SCE, E_2 = 0.95 V vs SCE, and k = 100 s^{-1}.

substituents. This makes sense if the two phenyls are rotated out of the plane of the molecule. The fact that E_2 - E_1 = 90 mV supports the idea of two weakly-coupled oxidations (compared to an uncoupled system, where $E_2 - E_1 \approx 35$ mV).[27] Oxidation of **3c** is irreversible up to 2000 V/s. Comparison of the **3c** oxidation peak current to its reduction counterpart suggests that the oxidation of **3c** is a two-electron process, but we were unable to determine this quantitatively, due to the previously mentioned problems in the **3c** reduction.

3.3.2 Spectroscopy

The absorbance and PL spectra are shown in Figure 3.13 and the results are summarized in Table 3.2. There are two peaks in the absorbance spectra. The shorter-wavelength peak (partially perturbed by the absorbance of the solvent) is usually associated with the substituents,[14] and the longer wavelength peak is associated with the silole itself. The absorption spectra of the silole with ethynyl-substituents are slightly red-shifted from those with ethylene-substituents. The λ_{max} for the three ethynyl-substituted siloles are very near one another, as expected, given the similarities in the structures. Of the siloles with ethylene substituents, **3c** is blue-shifted 33 to 35 nm with respect to **3a** and **3b**, consistent with the electrochemical data showing less conjugation of the crowded phenyl rings on the ethylene substituents in **3c** because of steric interactions.

All of the compounds, except **3c**, show fluorescence, with the ethynyl-substituted ones showing quite intense emission. Unlike the absorbance, the

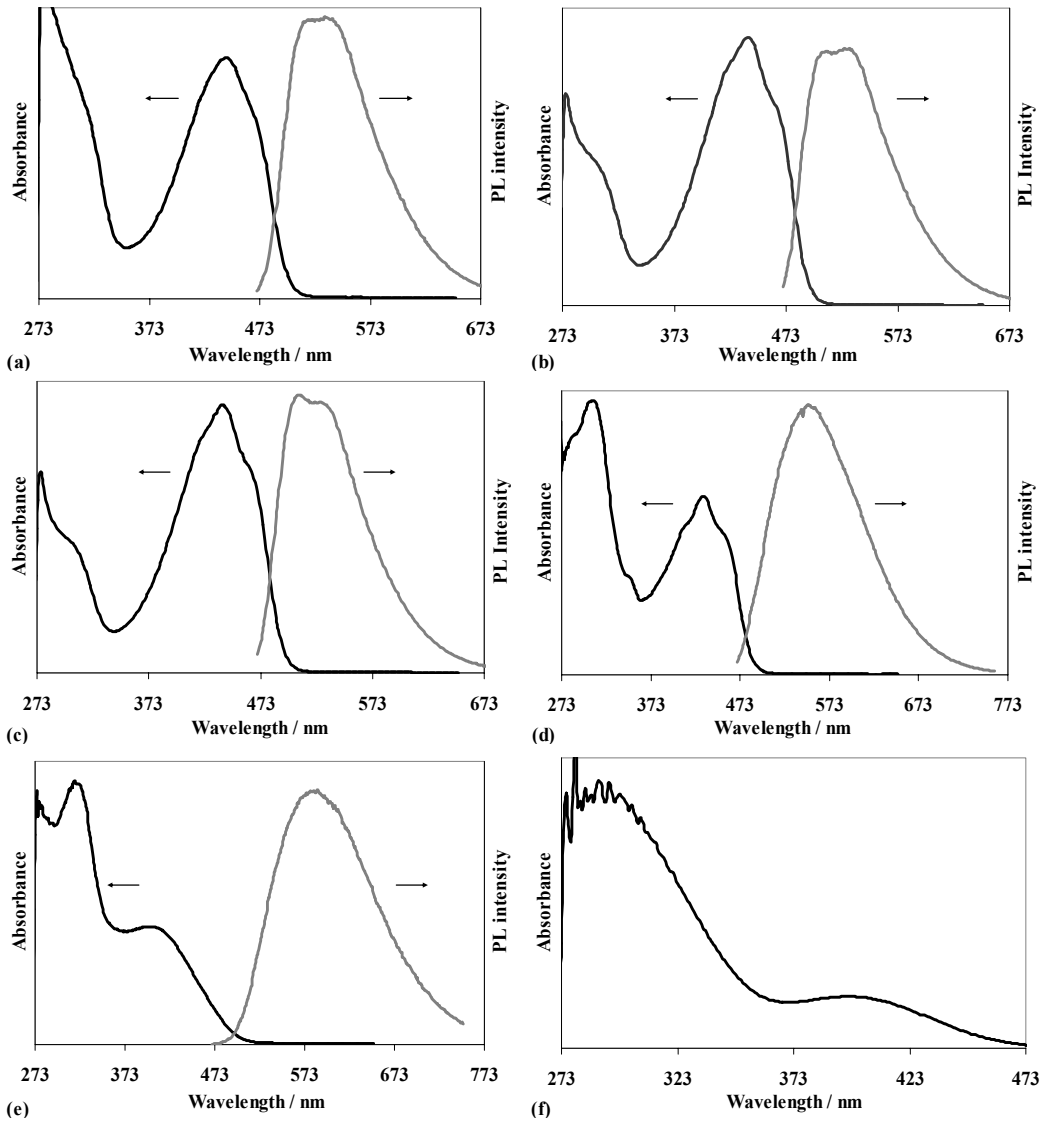

Figure 3.13. Absorbance and PL spectra (where applicable) of (a) **2a**, (b) **2b**, (c) **2c**, (d) **3a**, (e) **3b**, (f) **3c** in 1:1 C_6H_6/MeCN. All compounds were excited at the absorbance peak wavelength.

Table 3.2. Spectroscopic data for siloles. Absorbance and fluorescence measurements in dichloromethane.

Silole	**PL quant. eff. Φ[a]**	**Abs. max. λ_{ABS} / nm**	**PL max. λ_{PL} / nm**	**Stokes shift $\Delta\lambda$ / nm**	**E_{PL} / eV**	**ΔH_{ann} / eV**	**ECL eff.[c]**
2a	0.300	443	522	79	2.38	2.95	0.01
2b	0.630	439	529	90	2.35	2.87	0.1
2c	0.560	439	507	68	2.45	2.94	0.1
3a	0.183[b]	435	548	113	2.27	2.69	0.001
3b	0.016	433	584	151	2.13	2.8	0.01
3c	NA	398	NA	NA	2.60	3.07	NA

[a] Φ_{PL} determined with respect to fluorescein.

[b] Tamao reports Φ= 0.047 with respect to fluorescein.[1]

[c] Represents the fraction of emission of a DPA cell under similar conditions. Accurate to about an order of magnitude.

emission from **2c** is significantly blue-shifted from **2a** and **2b.** The smaller Stokes shift for **2c** could represent smaller reorganization in the excited state because of its steric rigidity. The ethylene-substituted compounds show larger Stokes shifts and smaller emission quantum efficiencies, probably because of the much greater flexibility of the substituents. The increasing number of phenyls in the ethylene-substituted series increases the number of degrees of freedom for internal conversion processes. This could explain the trend of decreasing quantum efficiency from **3a** to **3c**.

3.3.3 Electrogenerated Chemiluminescence (ECL)

As can be predicted from the high photoluminescence quantum yield and reversible electrochemistry for reductive and oxidative processes, siloles 2c and 2b give well-defined ECL upon cycling between potentials on the first reduction and oxidation waves. These ECL spectra overlap their photoluminescence spectra, as shown in Figure 3.14. The PL spectra exhibit two peaks where the ECL spectra have only one, due to the wide slit width (~1 mm) employed in the ECL measurements to capture the weaker emission. We were able to detect ECL with **2a** by pulsing the electrode with a 0.1 s pulse width and recording the total emission with a photomultiplier tube, but were unable to obtain an ECL spectrum because its radical cation was too unstable. As shown in Figure 3.15, the initial ECL signal was intense, as would be expected from its high PL quantum efficiency, but it rapidly diminishes after a few pulses; similar behavior is

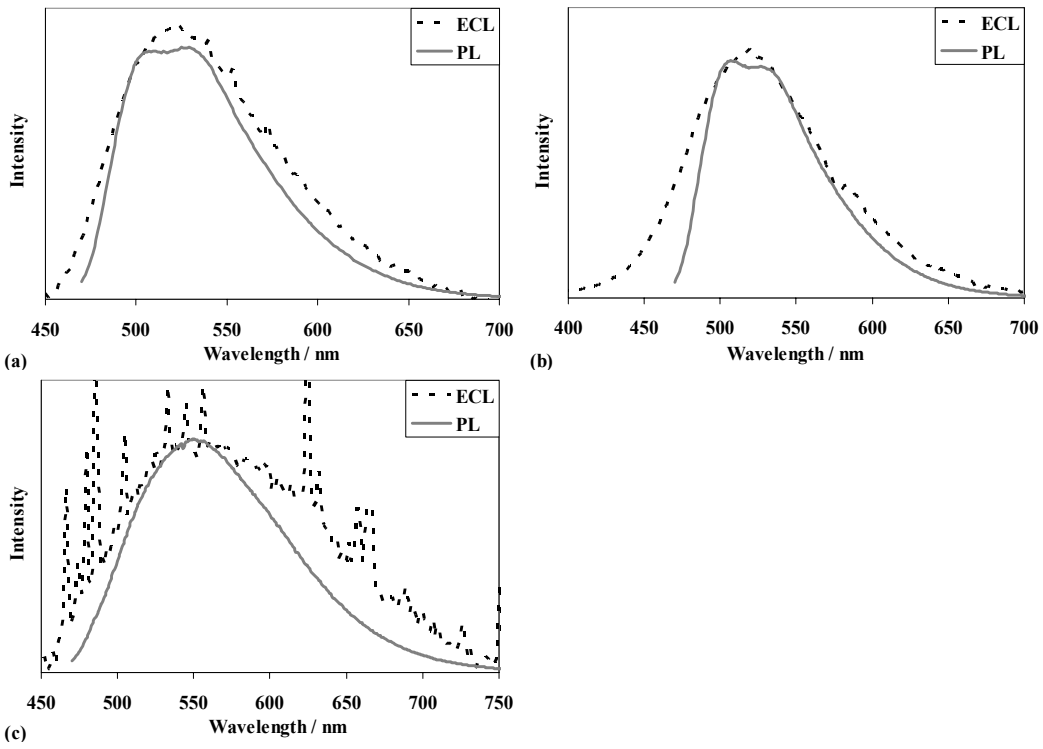

Figure 3.14. Overlays of ECL and PL spectra for (a) **2b**, (b) **2c**, (c) **3a** in 1:1 C_6H_6/MeCN. No other compounds were sufficiently stable to obtain ECL spectra. Spectra were generated by pulsing between a potential approximately 100 mV past the peak potentials for reduction and oxidation of each compound. Pulse width for all compounds was 100 ms.

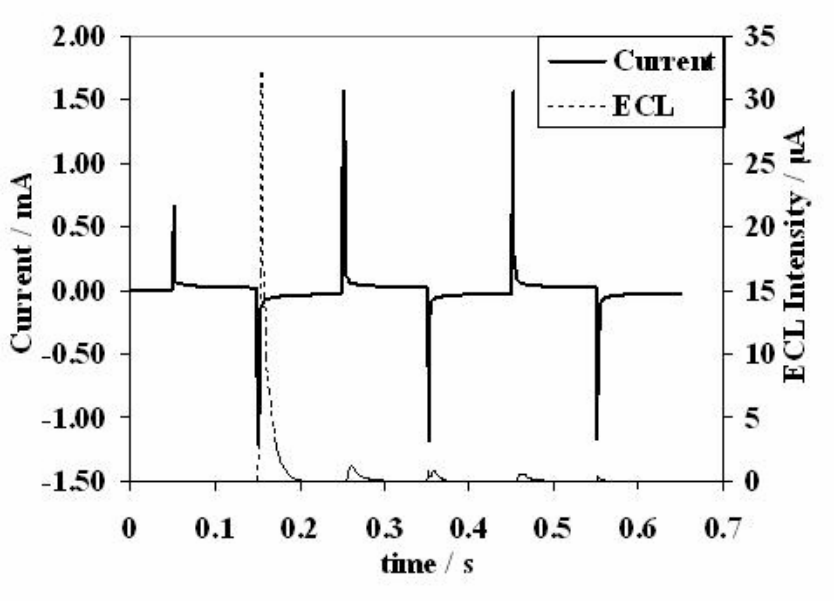

Figure 3.15. Intensity-time curve for **2a** ECL, generated by pulsing a single electrode at the first oxidation and first reduction potentials of the compound. The unstable radical cation of **2a** leads to a rapid loss of ECL intensity after multiple pulses.

observed for **3b**. While **3a** has a low fluorescence quantum yield, its homogeneous reactions are still slow enough that they do not compete with the time scale of the electrode pulses. Hence, this compound is also capable of stable ECL, and a spectrum was obtained for it as well (Figure 3.14c). In all cases where ECL was observed, the energy of the radical ion annihilation wassufficient to produce the energy of the singlet excited state.16[b]

3.4 Conclusions

The three ethynyl-substituted and three ethylene-substituted siloles show different trends in their electrochemical and photophysical behavior. The ethylene-substituted siloles have less steric rigidity, which gives them more ways to vibrationally dissipate energy, hence they show lower fluorescence quantum efficiencies. To alleviate steric stress in **3b** and **3c**, the 2,5-substituents are forced to rotate out of the plane of the silole moiety, whereas **3a** can remain completely planar. Thus, the chromophores of **3b** and **3c** have less protection from secondary reactions upon oxidation or reduction. As a result, their radical ions are less stable, and they have lower fluorescence quantum yields than **3a**, and poor ECL.

The ethynyl-substituted siloles are more sterically rigid. They show higher fluorescence quantum efficiencies than the ethylene-substituted siloles, but the unprotected triple bonds can lead to poor oxidative behavior. By adding *t*-butyl groups to the silicon the bonds are more protected from secondary

homogeneous reactions. Thus, these compounds exhibit high fluorescence quantum efficiencies and produce ECL on radical ion annihilation.

3.5 References

(1) Yamaguchi, S.; Tomonori, E.; Uchida, M.; Izumizawa, T.; Furukawa, K.; Tamao, K. *Chem. Eur. J.* **2000**, *6*, 1683.

(2) Zhan, X.; Risko, C.; Amy, F.; Chan, C.; Zhao W.; Barlow, S.; Kahn, A.; Brédas, J.-L.; Marder, S. *J. Am. Chem. Soc.* **2005**, *127*, 9021.

(3) Yu, G.; Yin, S.; Liu Y.; Chen J.; Xu, X.; Sun, X.; Ma D.; Zhan, X.; Peng, Q.; Shuai, Z.; Tang, B.; Zhu, D.; Fang, W.; Luo, Y. *J. Am. Chem. Soc.* **2005**, *127*, 6335.

(4) Lee, J.; Liu, Q.-D.; Motala, M.; Dane, J.; Gao, J.; Kang, Y.; Wang, S. *Chem. Mater.* **2004**, *16*, 1869.

(5) Chen, J.; Law, C.; Lam, J.; Dong, Y.; Lo, S.; Williams, I.; Zhu, D.; Tang, B. *Chem. Mater.* **2003**, *15*, 1535.

(6) Janzen, E.; Harrison, W.; Dubose, C. *J. Organometal. Chem.* **1972**, *40*, 281.

(7) Yamaguch, S.; Endo, T.; Uchida, M.; Izumizawa, T.; Furukawa, K.; Tamao, K. *Chem. Lett.* **2001**, 98.

(8) Dhiman, A.; Zhang, Z.-R.; West, R.; Becker, J. Y. *J. Electroanal. Chem.* **2004**, *569*, 15-22.

(9) Tamao, K.; Yamaguchi, S.; Shiro, M. *J. Am. Chem. Soc.* **1994**, *116*, 11715.

(10) a) S. Yamaguchi, T. Endo, M. Uchida, T. Izumizawa, K. Furukawa, K. Tamao, *Chem. Eur. J.* **2000**, *6*, 1683-1692; b) J. Lee, Q.-D. Liu, M. Motala, J. Dane, J. Gao, Y. Kang, S. Wang, *Chem. Mater.* **2004**, *16*, 1869-1877. Increased quantum yields (21%) have been obtained from 3,4-diarylsiloles via aggregation-induced emission, see: a) J. Luo, Z. Xie, J. W. Y. Lam, L. Cheng, H. Chen, Q. Chengfeng, H. S. Kwok, X. Zhan, Y. Lui, D. Zhu, B. Z. Tang, *Chem. Commun.* **2001**, 1740-1741; b) J. Chen, Z. Xie, J. W. Y. Lam, C. C. W. Law, B. Z. Tang, *Macromolecules* **2003**, *36*, 1108-1117; c) J. Chen, C. C. W. Law, J. W. Y. Lam, Y. Dong, S. M. F. Lo, I. D. Williams, D. Zhu, B. Z. Tang, *Chem. Mater.* **2003**, *15*, 1535-1546.

(11) Boydston, A. J.; Pagenkopf, P. L. *Angew. Chem. Int. Ed.* **2004**, *43*, 6336.

(12) Tamao, K.; Uchida, M.; Izumizawa, T.; Furukawa, K.; Yamaguchi, S. *J. Am. Chem. Soc.* **1996**, *118*, 11974.

(13) Uchida, M.; Izumizawa, T.; Nakano, T.; Yamaguchi, S.; Tamao, K; Furukawa, K. *Chem. Mater,* **2001**, *13*, 2680.

(14) Tang, B. Z.; Zhan, X.; Yu, G.; Lee, P. P. S.; Liu, Y.; Zhu, D. *J. Mater. Chem.*, **2001**, *11*, 2974.

(15) Yamaguch, S.; Tamao, K. *J. Chem. Soc., Dalton Trans.* **1998**, 3693.

(16) For reviews of ECL, see: (a) Richter, M. M. *Chem. Rev.* **2004**, *104*, 3003; (b) *Electrogenerated Chemiluminescence*; Bard, A.; Marcel Dekker: New York, NY, 2004.

(17) Dietz, R. In *Organic Electrochemistry*; Baizer, M.; Ed.; Marcel Dekker: New York, NY, **1973**, pp 256-266.
(18) Eberson, L. In *Organic Electrochemistry*; Baizer, M.; Ed.; Marcel Dekker: New York, NY, **1973**, pp 448-465.
(19) Boydston, A. J.; Pagenkopf, P. L. *Angew. Chem. Int. Ed.* **2004**, *43*, 6336.
(20) Chen, S.-A.; Shy, H.-J. *J. Poly. Sci.: Poly. Chem. Ed.* **1985**, *23*, 2441.
(21) Sahami, S.; Weaver, M. *J. Electroanal. Chem.* **1981**, *122*, 155.
(22) (a) Rudolf, M. *J. Electroanal. Chem.* **2003**,*543,* 23; (b) Ruldolf, M. *J. Electroanal. Chem.* **2004**, *571*, 289; (c) Rudolf, M. *J. Electroanal. Chem.* **2003**, *558*, 171. (d) Rudolf, M. *J. Comp. Chem.* **2005**, *26*, 619; (e) Rudolf, M. *J. Comp. Chem.* **2005**, *26*, 233; (f) Rudolf, M. *J. Comp. Chem.* **2005**, *26*, 1193.
(23) Kadish, K.; Ding, J.; Malinski, T. *Anal. Chem.* **1984**, *56*, 1741.
(24) Bard, A. and Faulkner L.; *Electrochemical Methods: Fundamentals and Applications, 2nd Ed*; John Wiley & Sons, Inc.: NY, **2001**, pp 234-238.
(25) Cauquis, G. In *Organic Electrochemistry*; Baizer, M.; Ed.; Marcel Dekker: New York, NY, **1973**, pp 33-35.
(26) Bard, A. and Faulkner L.; *Electrochemical Methods: Fundamentals and Applications, 2nd Ed*; John Wiley & Sons, Inc.: NY, **2001**, pp 471-528.
(27) Bard, A. and Faulkner L.; *Electrochemical Methods: Fundamentals and Applications, 2nd Ed*; John Wiley & Sons, Inc.: NY, **2001**, pp 507.

Chapter 4: Spirobifluorene-linked Bisanthracene (spiro-FPA): A Possible Simultaneous Two-Electron Transfer?

4.1 Introduction

The electrogenerated chemiluminescence (ECL) of 2,2′-bis(10-phenylanthracen-9-yl)-9,9′-spirobifluorene (spiro-FPA, Figure 4.1) raises the interesting possibility of an outer sphere, simultaneous, two-electron transfer during the annihilation of the radical di-ion pairs. Electrochemical literature has popularized the notion that apparent two-electron transfers actually consist of two, one-electron transfers separated by a conformational change in the substrate compound. The determination of the individual redox potentials for these reactions reinforces this view.[1] However, despite the ubiquity of the one-electron transfer mechanism, simultaneous, two-electron transfer has never been proven impossible. In this paper, we show how the formation of excimers during the ECL of spiro-FPA provides strong evidence for simultaneous, two-electron transfer during the annihilation between its dianion and dication.

Spiro-FPA consists of two phenylanthracene redox centers linked by a spirobifluorene unit (PA~X~PA). The sp3 carbon of the spirobifluorene disrupts conjugation between the centers. The structure of each redox center is thus analogous to that of 9,10-diphenylanthracene (DPA), a highly luminescent, blue emitter ($\Phi_{PL} \approx 0.91$,[2] $\Phi_{ECL} \approx 0.014$[3]) with stable radical ions,[4] and one of the first

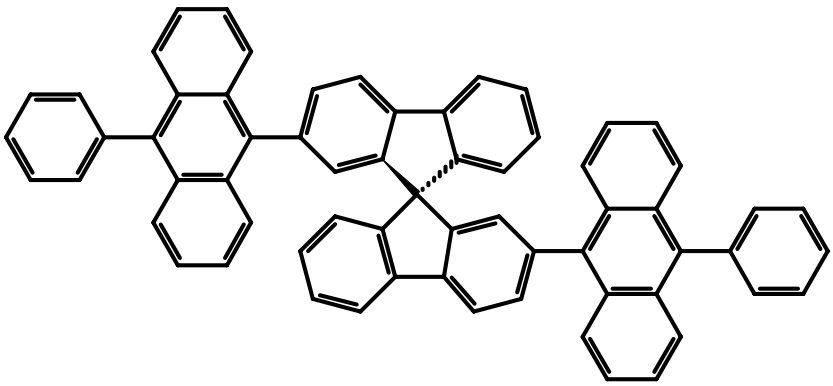

Figure 4.1. Structure of Spiro-FPA.

molecules from which ECL was observed.[5] The structural similarities between spiro-FPA and DPA lead to many similarities in the spectroscopy and electrochemistry of the two molecules. However, two notable differences are electroluminescence, where the greater structural rigidity and steric bulk improve spiro-FPA device stability over that of DPA,[6] and ECL, where the spirobifluorene linkage of two DPA centers encourages excimer formation, despite the additional steric bulk.

ECL is the production of light by the annihilation of electrochemically generated radical ions.[5,7] If ΔH_{ann}^{o}, the enthalpy of radical ion annihilation, exceeds the energy of the first excited singlet state, E_s, the annihilation can directly populate the singlet state (i.e., the system is energy sufficient). This is called S-route ECL.

$$R + e \rightarrow R^{\bullet -} \quad (4.1)$$

$$R - e \rightarrow R^{\bullet +} \quad (4.2)$$

$$R^{\bullet +} + R^{\bullet -} \rightarrow {}^1R^* + R \quad (4.3)$$

$${}^1R^* \rightarrow R + h\nu \quad (4.4)$$

If a coreactant is used, only one of the radical ions is necessary to generate ECL. For example, the coreactant, persulfate, can be electrochemically reduced to generate the powerful oxidizing agent, $SO_4^{\bullet -}$, as shown below. $SO_4^{\bullet -}$ can then oxidize the anion radical formed in the same potential step without directly generating the cation radical at the electrode surface. Coreactant ECL is used

when annihilation is difficult to achieve, due to a narrow solvent window or rapid homogeneous reactions of one of the radical ions. Because coreactants decrease annihilation, they have also been used to identify annihilation-specific phenomena, such as excimer formation, that occur during ECL but not during PL.[8]

$$R + e \rightarrow R^{\bullet -} \quad (4.5)$$

$$R^{\bullet -} + S_2O_8^{2-} \rightarrow R + SO_4^{2-} + SO_4^{\bullet -} \quad (4.6)$$

$$R^{\bullet -} + SO_4^{\bullet -} \rightarrow R^* + SO_4^{2-} \quad (4.7)$$

$$R^* \rightarrow R + h\nu \quad (4.8)$$

Generally, planar molecules such as 9,10-dimethylanthracene, will have a greater probability of forming excimers both in PL and ECL.[9,10] In DPA, however, the phenyl substituents are so bulky that they are rotated out of the anthracene plane by 68°,[11] and excimer formation is sterically inhibited.[12] Spiro-FPA possesses similar steric hindrance to that of DPA, but each spiro-FPA molecule consists of two redox centers, so the radical ions created at the electrode surface carry 2+ and 2- charges. The charges on the molecule are separated from one another by the spirobifluorene moiety, so we represent the dication as $PA^{\bullet +}$~X~$PA^{\bullet +}$ and the dianion analogously. The attraction between the radical di-ions is four times greater than that between mono-ions. If this additional attractive force is sufficient to overcome the steric hindrance created by the 9,10 substituents, excimer emission will be visible in the ECL spectrum. Thus, we can distinguish between mono-ion annihilation and di-ion annihilation.

Scheme 3 shows the pathways for excimer formation and emission. The activated complex is represented by vertically stacked spiro-FPA di-ions, as shown in reaction (9). Since an excimer created by a one-electron transfer between the di-ions should be immediately quenched by electron transfer from the other redox center, as shown in reactions (10) and (11), excimer emission from these molecules supports a simultaneous, two-electron transfer mechanism (reaction (12)).

Scheme 4.1. Pathways for spiro-FPA excimer formation and emission.

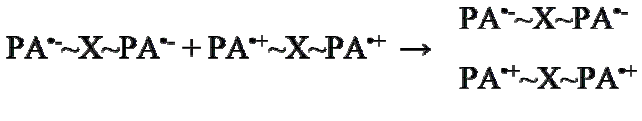

(9)

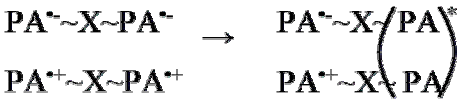

(10)

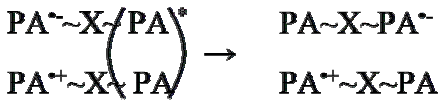

(11)

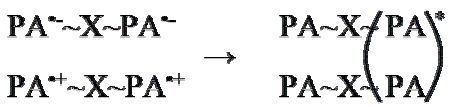

(12)

By varying the electrolyte concentration, we observe a correlation between the effective electrostatic attraction between geminate radical ion pairs and the relative excimer emission. Therefore, the ionic strength plays a significant role in overcoming the steric barrier to excimer formation. With this data, we show how

a molecule with multiple redox centers can be used to demonstrate simultaneous two-electron transfer.

4.2 Experimental Section

4.2.1 Materials.

Spiro-FPA was synthesized as reported in the literature.[6] Anhydrous MeCN was obtained from Aldrich (St. Louis, MO) and transferred directly into an inert atmosphere drybox (Vacuum Atmospheres Corp., Hawthorne, CA). Anhydrous PhH was obtained from Aldrich and distilled under vacuum to remove an electroactive impurity before transfer into the drybox. The supporting electrolyte, tetra-*n*-butylammonium perchlorate (TBAP), was obtained from Fluka and used as received. All solutions were prepared inside of the drybox and sealed in airtight cells for measurements outside of the drybox. Tetra-*n*-butylammonium peroxydisulfate ($TBA_2S_2O_8$) was prepared from tetrabutylammonium hydrogen sulfate and $K_2S_2O_8$ according to a literature procedure.[13]

4.2.2 Characterization.

Cyclic voltammograms (CVs) were performed on a CH Instruments 660 Electrochemical Workstation (Austin, TX). The working electrode (WE) was a 0.5 mm Pt disk, inlaid in glass. For ECL experiments, a 1.5 mm inlaid Pt disk WE was bent at 90˚ so it faced the detector. The WE in each case was polished on a felt pad with 0.3 μm alumina (Buehler, Ltd, Lake Bluff, IL), then sonicated in water followed by ethanol for 1 min each, before being rinsed with acetone and

transferred into the drybox. The counter electrode was a Pt wire. An Ag wire was used as a quasi-reference electrode and calibrated with ferrocene (0.342 V vs SCE).[14] All solutions for electrochemical experiments contained 0.5 mM spiro-FPA and 0.1 M TBAP in 3:1 PhH/MeCN. Coreactant ECL solutions also contained 10 mM $TBA_2S_2O_8$. Solutions were prepared in a glass cell inside of the dry box. The cells were closed with a Teflon cap fitted with a rubber o-ring to form an airtight seal, so measurements could be made outside of the box. Stainless steel rods were driven through the cap to form the electrode connections several centimeters above the solution level.

Absorbance spectra were collected on a DU 640 spectrophotometer (Beckman, Fullerton, CA), using a 56 μM solution of spiro-FPA in 3:1 PhH/MeCN in a 1 cm quartz cell, and a 52 μM solution of DPA in the same solvent. PL spectra of solutions of 560 nM spiro-FPA and 520 nM DPA, both in 3:1 PhH/MeCN were obtained using a QuantaMaster Spectrofluorimeter (Photon Technology International, Birmingham, NJ) with a 2 nm band pass at the excitation and emission slits.

ECL Spectra were obtained by pulsing the electrode potential 80 mV beyond the reduction and oxidation peak potentials, (i.e., between $E_{p,ox}$ + 80 mV and $E_{p,red}$ – 80 mV), using an Eco Chemie (The Netherlands) Autolab Potentiostat. Coreactant ECL spectra were generated by pulsing between 0 V and $E_{p,red}$ – 80 mV. ECL spectra were collected using a Princeton Instruments (Trenton, NJ)

charge-coupled device (CCD) camera cooled to -100˚C with an Acton SpectraPro-150 monochromator (Acton, MA). Each spectrum was calibrated with a Hg lamp after it was obtained.

4.2.3 Simulations.

2-D Digital simulations of the electrochemical processes were performed using the DigiElch software package.[15] The double-layer capacitance of 17.1 nF and the uncompensated resistance of 6155Ω were extracted from the current transient for a nonfaradaic potential step. The electrode area used in the simulations was determined from a Cottrell plot obtained in 1 mM ferrocene in MeCN taking the diffusion coefficient as 2.4×10^{-5} cm^2/s.[16] All electrochemical processes were treated as diffusion controlled and assigned heterogeneous electron transfer rate constants of k^o = 10 cm/s. The diffusion coefficient, D, and the redox potentials were adjusted until the best fit was obtained between experiment and simulation.

ECL simulations of the di-ion annihilation were performed using COMSOL Multiphysics 3.3 (COMSOL, Inc). The diffusing species were confined to a 2.4 mm 1-D cell consisting of 118 mesh elements. The mesh size was 10 nm at the electrode surface, and expanded by factors of 1.2 with increasing distance from the electrode. The Butler-Volmer equation was used as the electrode boundary condition, and spiro-FPA was assigned an electron transfer rate of k^o = 10 cm/s. The analyte was allowed two, separate, one-electron

reductions and oxidations at the electrode. The electrode potential was pulsed between -2.13 V and 1.30 V vs SCE at 5 Hz by using Heaviside functions to switch on one potential while the other was off. All data was taken from the fourth potential pulse (a reduction).

All annihilation reactions between anions and cations, as well as excited state quenching reactions, were assigned a rate constant, k_{ann}, of 2×10^8 $M^{-1}s^{-1}$.[17] Normal excited states were generated by mutual annihilation between mono-ions and by 50% of annihilations between a di-ion and a mono-ion of opposite charge. The other 50% created an ion and a neutral molecule, to reflect the possibility of electron transfer quenching if the excited state is created on the di-ion rather than the mono-ion. Monomer excited states were quenchable by electron transfer from any ion in solution. Mutual di-ion reactions were given the possibility of a one-electron transfer to create two ground state mono-ions, or a two-electron transfer to create an excimer. Additionally, di-ions were allowed to react with neutral molecules to comproportionate into two mono-ions. The equilibrium constant for this process was calculated from experimentally determined E^o values to be 7 for the dianion and 10 for the dication. Assuming that the difference between K_{eq} values is within experimental error, $K_{eq} = 8.5$ was assigned to both dianion and dication comproportionation, and maintained by choosing $k_{f,com} = 2.000\times10^6$ $M^{-1}s^{-1}$ and $k_{b,com} = 0.235\times10^6$ $M^{-1}s^{-1}$. The rate constant for emission from the excited state was chosen as $k_{em} = 1.4\times10^8$ s^{-1}.[18]

4.3 Results and Discussion

4.3.1 Electrochemistry

Cyclic voltammetry was used to assess the stability of the reduced and oxidized spiro-FPA species. A CV showing both oxidation and reduction of spiro-FPA is presented in Figure 4.2. Comparison between digital simulations and experimental CVs of the oxidation and reduction are shown in Figures 4.3 and 4.4, Supporting Information, respectively. The CV simulation mechanism assigned two, reversible, one-electron processes to both oxidation and reduction, with a ΔE^o between the two waves of 50 mV on the reduction side and 60 mV on the oxidation side, and $D = 8.5\times10^{-6}$ cm^2/s. Thus $E^o_{1,red} = -2.02$, $E^o_{2,red} = -2.07$ V vs SCE, $E^o_{1,ox} = 1.14$, and $E^o_{2,ox} = 1.20$ V vs SCE. The plots in Figures 4.3 and 4.4 indicate good fits between experimental and simulated CVs performed at scan rates (v) from 50 mV/s to 10 V/s. The small deviations that occur in the reduction simulations at high scan rates are likely due either to uncompensated resistance that was underestimated in the simulation or to slow heterogeneous electron transfer kinetics on the reduction.

For DPA, $E^o_{red} = -2.06$ V vs SCE, and $E^o_{ox} = 1.15$ V vs SCE. Since $E^o_{spiro\text{-}FPA} \approx E^o_{DPA}$ for oxidation and reduction, both redox centers of spiro-FPA are similar to an isolated DPA molecule; however, since $E_2^o - E_1^o > 35.6$ mV, some small interaction may exist between the two redox centers of spiro-FPA.[19]

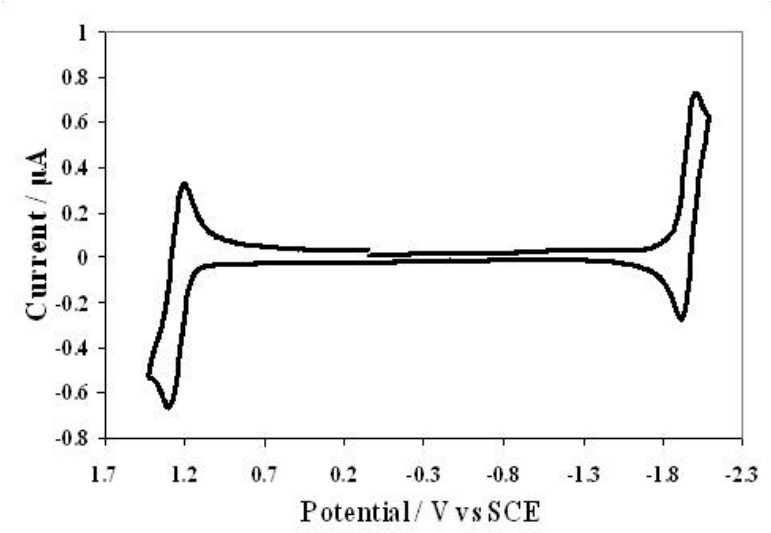

Figure 4.2. Cyclic voltammogram of 0.5 mM spiro-FPA in 3:1 benzene/acetonitrile. Scan rate = 200 mV/s.

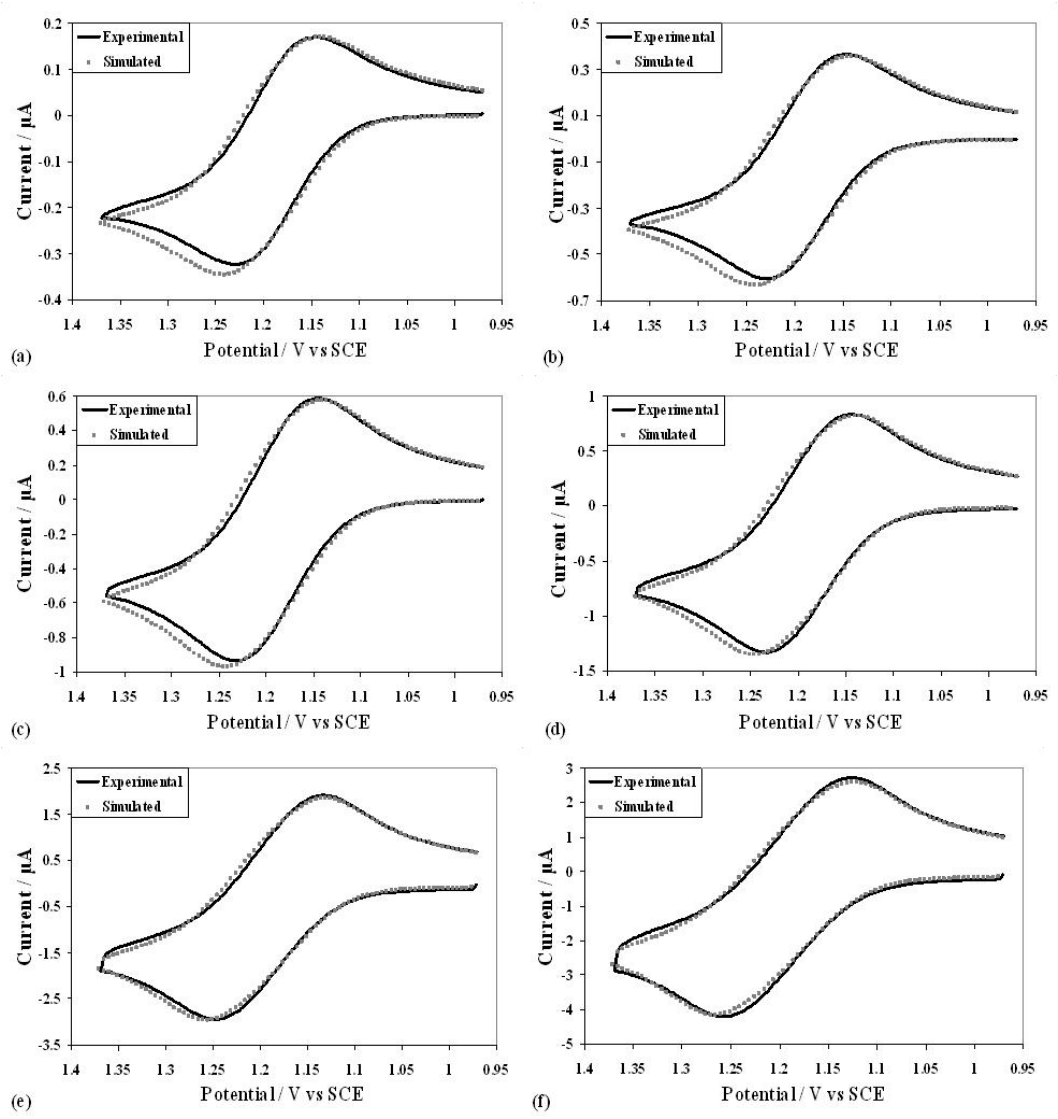

Figure 4.3. Simulation of 0.5 mM spiro-FPA oxidation at (a) 50 mV/s, (b) 200 mV/s, (c) 500 mV/s, (d) 1 V/s, (e) 5 V/s, (f) 10 V/s. Simulation mechanism is two one-electron oxidations with $D = 8.5\times10^{-6}$ cm^2/s, $E^o_{1,ox} = 1.14$ V vs SCE, $E^o_{2,ox} = 1.20$ V vs SCE, $k^o = 10^4$ cm/s, $\alpha = 0.5$, $R_u = 6155\Omega$, $C_d = 17.1$ nF.

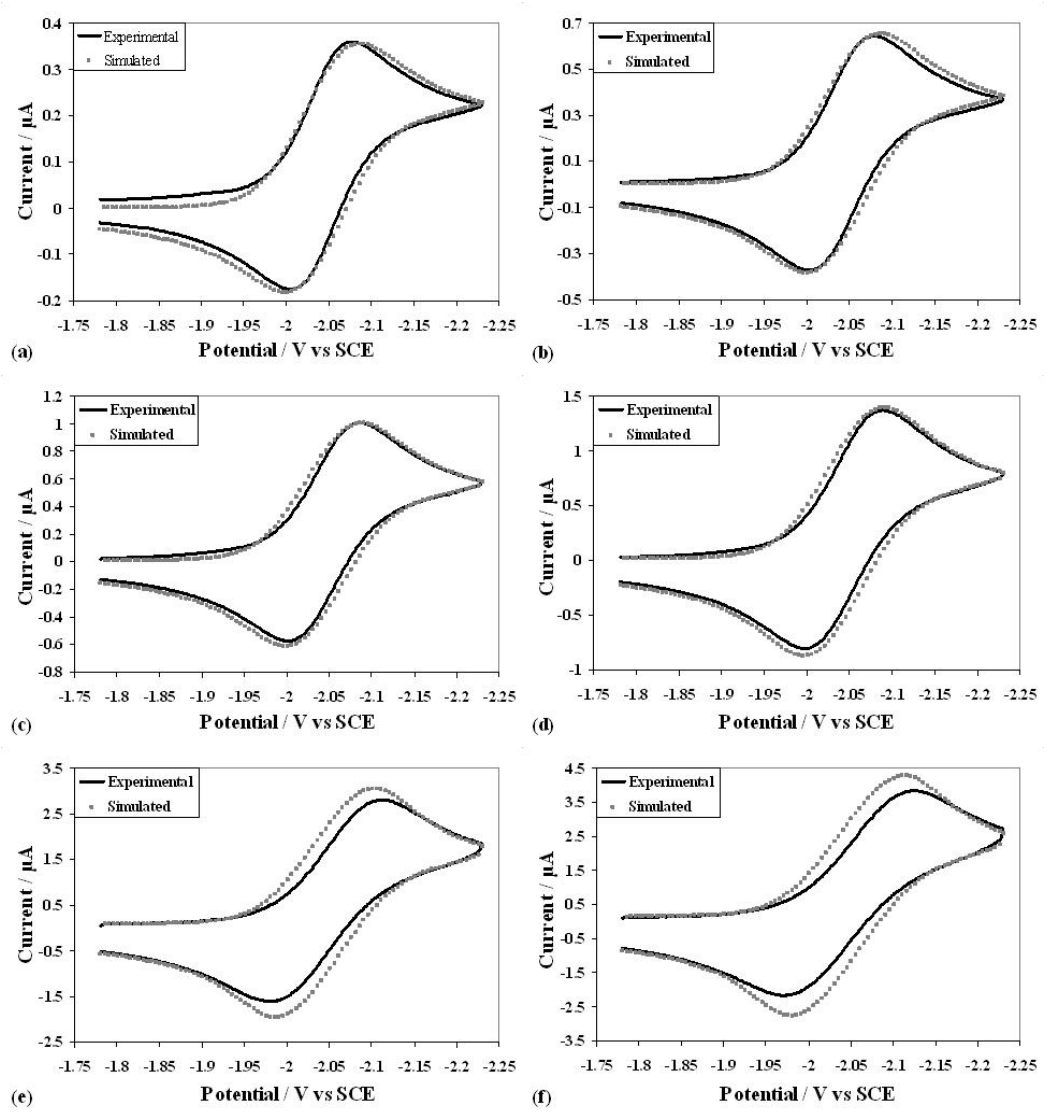

Figure 4.4. Simulations of 0.5 mM spiro-FPA reduction at (a) 50 mV/s, (b) 200 mV/s, (c) 500 mV/s, (d) 1 V/s, (e) 5 V/s, (f) 10 V/s. Simulation mechanism is two one-electron reductions, with $D = 8.5\times10^{-6}$ cm^2/s, $E^o_{1,red}$ = -2.02 V vs SCE, $E^o_{2,red}$ = -2.07 V vs SCE, $k^o = 10^4$ cm/s, $\alpha = 0.5$, $R_u = 6155\Omega$, $C_d = 17.1$ nF.

The potentials of the DPA second oxidation[20] and reduction[21] waves were compared to those of the corresponding spiro-FPA waves to assess whether the conjugation through the fluorene moiety or the presence of an additional, charged PA unit would affect the potentials of the second waves. Scanning the potential negative beyond the first reduction reveals no additional waves before the solvent window is reached. Since DPA gave the same result, the absence of additional reduction waves is attributed to adventitious water narrowing the solvent window. Scanning the potential positive beyond the first oxidation wave reveals a chemically irreversible second oxidation with peak potential E_p = 1.58 V vs SCE. DPA gives a second oxidation wave at E_p = 1.59 V vs SCE. The similarity between second oxidation potentials emphasizes the lack of communication between PA centers.

4.3.2 Spectroscopy

The spectroscopic characteristics of spiro-FPA were compared to those of DPA to determine the effects of the bifluorene linking group on the PA moieties. The data is summarized in Table 4.1. The absorbance maxima, $\lambda_{max,abs}$, for all three major peaks of both molecules are within three nanometers of each other, as shown in Figure 4.5. The extinction coefficients, ε, for each of the major vibronic bands of spiro-FPA are approximately twice as large as their DPA counterparts. Thus spiro-FPA has twice the number of effective chromophores in solution as the same concentration of DPA. The short wavelength absorbance of spiro-FPA

Table 4.1. Spectroscopic data for spiro-FPA and DPA.

	λ_{abs} / nm	ε / $M^{-1}s^{-1}$	λ_{PL} / nm	Φ_{PL}	Φ_{ECL}
DPA	356	8500	420	0.91	0.014
	374	13800			
	395	13100			
Spiro-FPA	358	16300	434	0.74	0.0042
	377	25700			
	397	24800			

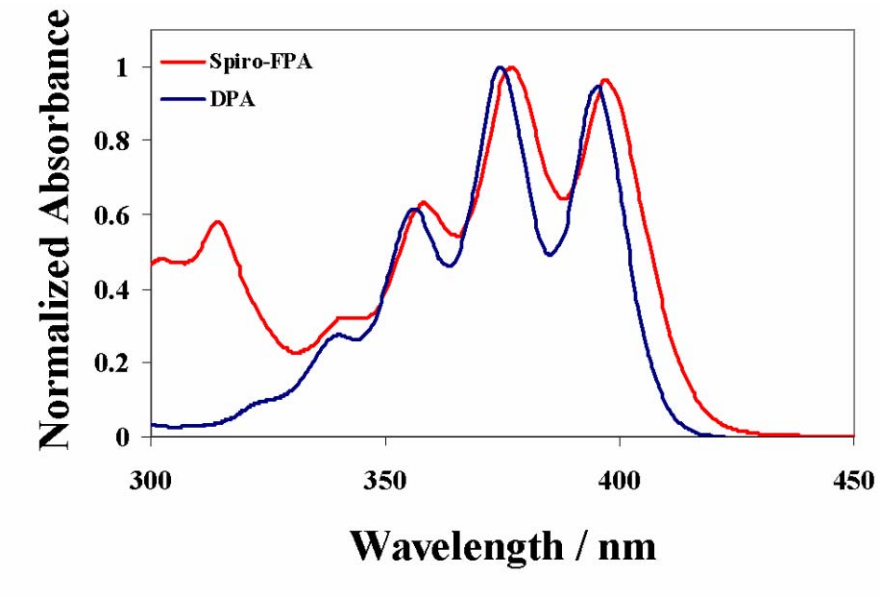

Figure 4.5. Absorbance spectra of solutions of 52 μM spiro-FPA and 56 μM DPA in 3:1 PhH/MeCN.

is attributed to absorption by the bifluorene moiety.

Photoluminescence spectra were generated by exciting DPA at 374 nm and spiro-FPA at 377 nm. The DPA emission maximum occurs at 420 nm, and the spiro-FPA emission maximum occurs at 434 nm, as shown in Figure 4.6. Since $\lambda_{max,abs}$ is the same for both molecules, the 15 nm bathochromic shift suggests that more structural rearrangement occurs in the excited state of spiro-FPA than in DPA. This greater flexibility may also increase internal conversion, as spiro-FPA exhibits a Φ_{PL} of 0.76.

The spiro-FPA ECL spectrum appears to be bathochromically shifted 15 nm from the PL spectrum, giving a λ_{max} of 450 nm. However, since the DPA spectrum does the same, this is attributed to the large self-absorption of the emission by the 0.5 mM ECL sample. A more significant difference between the ECL and PL spectra is the long wavelength ECL emission that extends to 720 nm (Figure 4.7). Long-wavelength ECL not observed in the PL typically results from either a side product of the electrochemistry[22] or the formation of excimers. The broad, structureless nature of the emission, as well as its absence when $TBA_2S_2O_8$ was used as a coreactant, suggest that the long-wavelength light comes from excimers.

The large steric hindrance to pi-stacking between two spiro-FPA molecules makes excimer formation improbable, especially since the steric hindrance of the similarly-structured DPA prevents it from forming excimers.

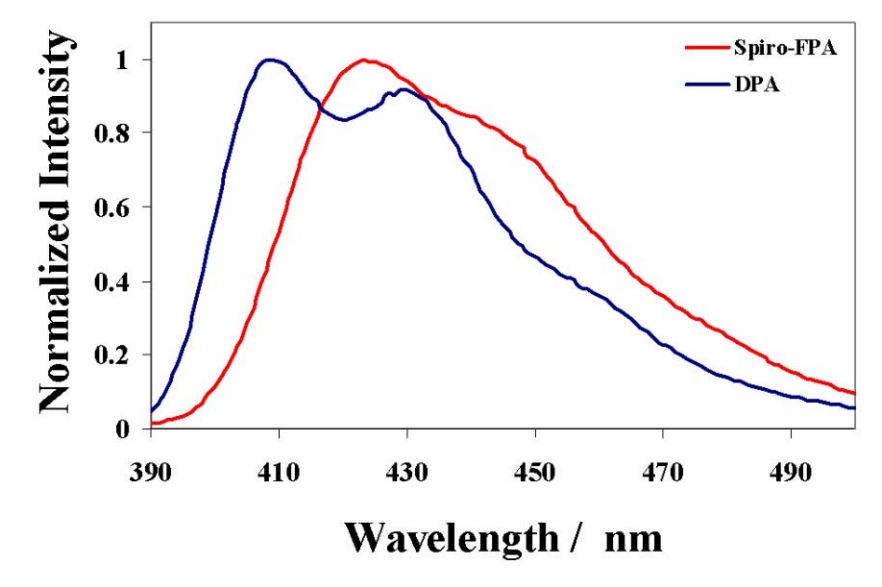

Figure 4.6. Fluorescence spectra of solutions of 0.52 μM spiro-FPA and 0.56 μM DPA in 3:1 PhH/MeCN.

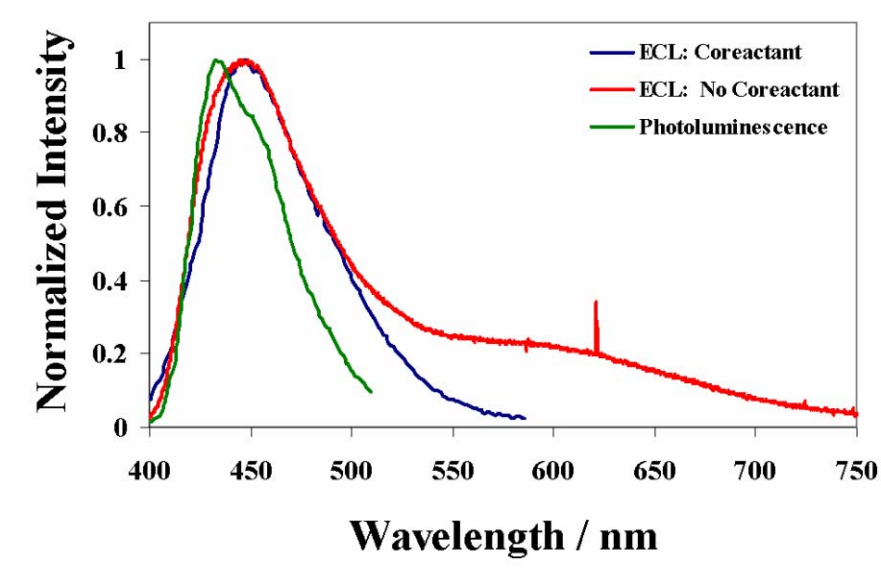

Figure 4.7. Photoluminescence spectrum of 0.52 μM spiro-FPA and ECL spectra of 0.5 mM spiro-FPA in 3:1 PhH/MeCN. ECL spectra were taken with and without 10 mM $S_2O_8^{2-}$ coreactant.

However, unlike DPA electrochemistry, spiro-FPA oxidation and reduction both generate di-ions. The attraction between 2+ and 2- charges is four times greater than that between their mono-ion counterparts, which may be sufficient to overcome the steric barrier to excimer formation.

This is confirmed by obtaining ECL spectra with different electrolyte concentrations. With low electrolyte concentration, the radical ions are less shielded from one another, so the stronger attraction between di-ions should become more apparent, yielding higher relative excimer emission. As shown in Figure 4.8, ECL spectra obtained in various concentrations of TBAP confirm this hypothesis only for experiments performed with the same pulse width. In 0.14 M TBAP, excimers were only observed at a pulse width of 0.01 s, and in 0.01 M TBAP, a large RC constant prevented the use of pulse widths shorter than 0.5 s, where no excimer emission was observed. These two boundaries present the useful concentration range for this experiment.

In Table 4.2, excimer formation is calculated as the background-subtracted intensity at 575 nm divided by the background-subtracted peak intensity (450 nm). Values around 0.05 indicate no excimer formation, whereas values around 0.2 were the maximum observed in these experiments. The data show greater relative excimer formation in samples with shorter pulse widths and lower electrolyte concentrations.

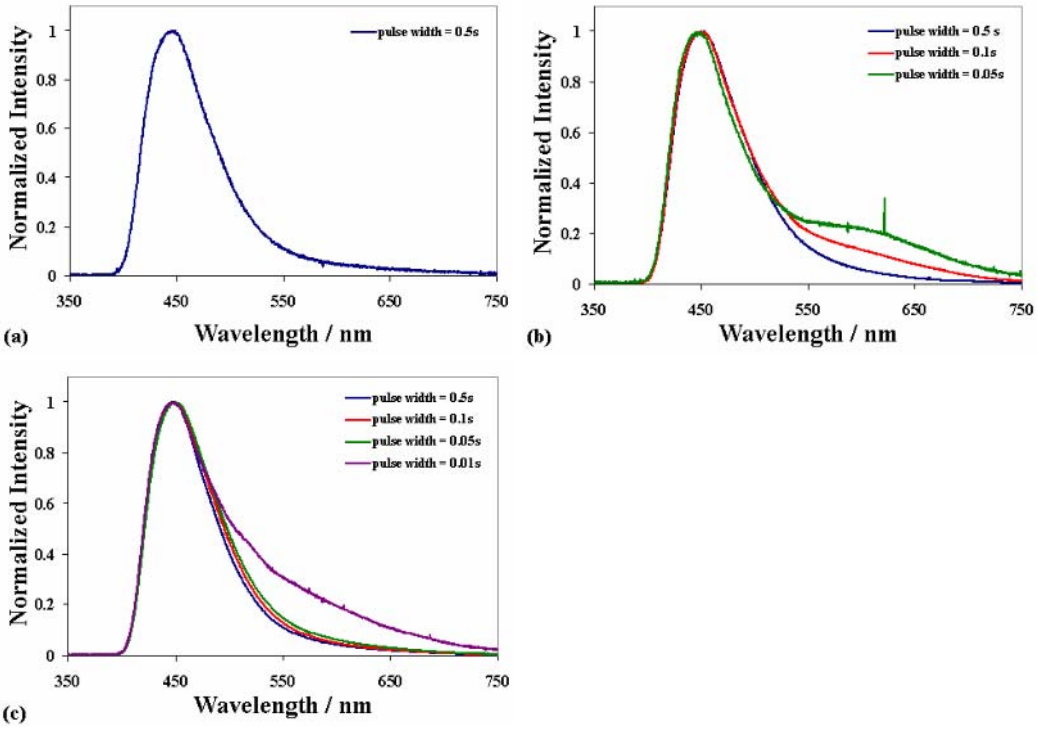

Figure 4.8. ECL spectra of 0.5 mM spiro-FPA obtained at various pulse widths using the following electrolyte concentrations: (a) 0.01 M TBAP (b) 0.05 M TBAP (c) 0.14 M TBAP.

Table 4.2. Relative excimer formation from 0.5 mM spiro-FPA in 3:1 PhH/MeCN at various pulse widths and concentrations of electrolyte, TBAP. Excimer fraction is defined as the intensity at 575 nm normalized by the peak intensity (450 nm).

Solution	**Pulse Width / s**	**Excimer Fraction**
0.01 M TBAP	0.5	0.06
0.05 M TBAP	0.5	0.09
	0.1	0.16
	0.05	0.23
0.14 M TBAP	0.5	0.06
	0.1	0.08
	0.05	0.09
	0.01	0.25
10 mM S_2O_8 and 0.1 M TBAP	0.1	0.004

4.3.3 ECL Simulations

To understand the pulse width dependence of the excimer formation, the concentration profiles of the excited monomer and excimer were examined using simulations of a potential pulse (Figure 4.9). A plot of the peak concentration of each species versus time (Figure 4.10) shows a more rapid decrease in excimer concentration than excited monomer concentration. This is probably due to the greater number of scavenging reactions available for di-ions than for mono-ions. Experiments that use shorter pulse widths yield a larger fraction of excimer emission because they occur in the time regime before the additional decomposition reactions prevent significant excimer formation. While the simulated decay rate confirms the proposed mechanism in terms of the experimental data, it cannot produce quantitatively accurate data because it does not include electrostatic effects. Therefore, the effects of TBAP concentration and the mutual attraction between di-ions are not considered in this simulation.

Once the molecules reach a conformation that allows excimer formation, a charge transfer is necessary to generate the excited state. The generation of an excited state via one-electron transfer is problematic, because the other two PA moities involved in the complex remain as unpaired radical ions, which could lead to electron transfer quenching. However, the simultaneous transfer of two electrons between each pair of phenylanthracenes could create a singlet excited state for the excimer.

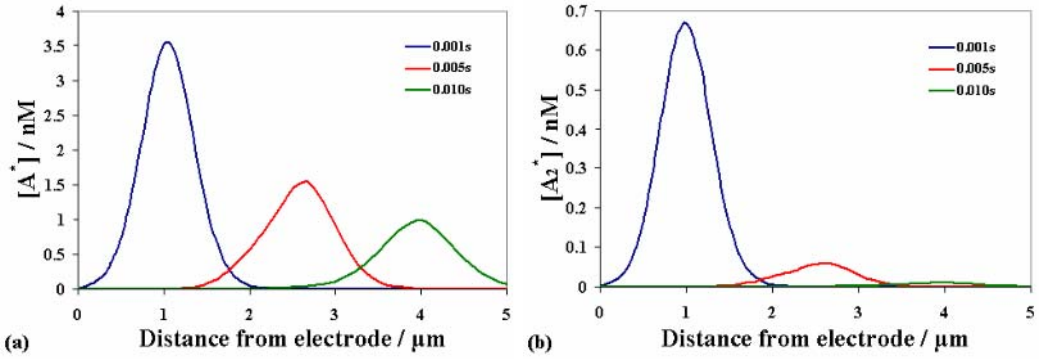

Figure 4.9. Concentration profiles for (a) the excited monomer and (b) the excimer generated during an ECL potential pulse in 0.5 mM spiro-FPA.

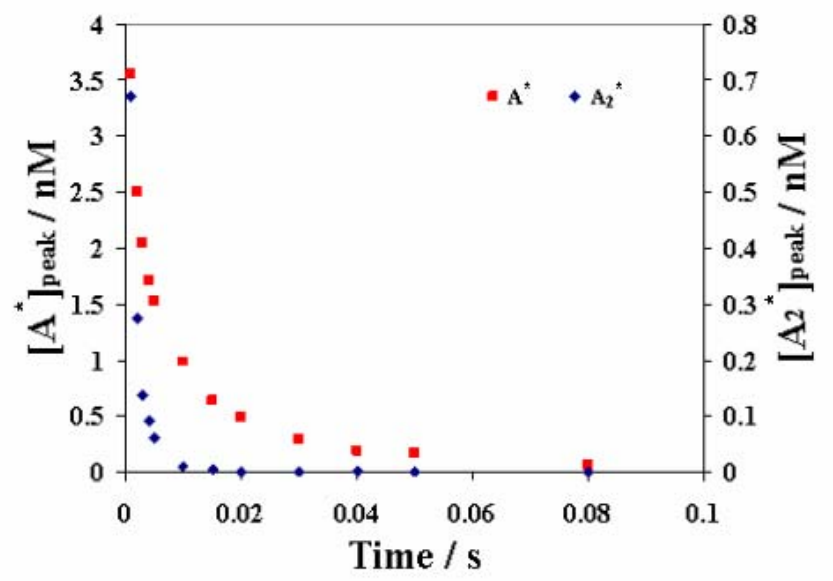

Figure 4.10. Simulated decay of spiro-FPA excimer and excited monomer concentration with time following an ECL potential pulse.

4.4 Conclusions

Spiro-FPA is comprised of two PA moieties, both of which undergo electrochemical processes at approximately the same potentials, indicating minimal interaction between them. Because there are two redox centers, di-ions are created during each potential pulse of an ECL experiment. The electrolyte concentration dependence of the excimer emission observed during annihilation ECL demonstrates the importance of high electrostatic charge to overcoming the steric hindrance to excimer formation. Solutions with lower electrolyte concentrations exhibit a larger fraction of excimer emission, because the greater electrostatic attraction between di-ions relative to mono-ions is more apparent in the absence of electrostatic shielding. Additionally, shorter pulse widths result in still higher relative excimer emission because the short time scales do not permit scavenging reactions to consume the di-ions prior to their annihilation. Since the annihilation occurs between di-ions, a single electron transfer to form an excimer should be quenched by transfer of the other electron prior to emission. Therefore, the presence of excimer emission in spiro-FPA suggests a simultaneous two-electron transfer.

4.5 References

(1) (a) Cauquis, G. Basic Concepts. In *Organic Electrochemistry*; Baizer, M., Ed.; Marcel Dekker, Inc.: New York, 1973; pp 43-48. (b) Bard, A.; Faulkner, L. *Electrochemical Methods: Fndamentals and Applications*, 2nd ed.; John Wiley & Sons, Inc.: New York, 2001; pp 108, 475-476. (c) Zanelo, P. *Inorganic Electrochemistry: Theory, Practice, and Application*; The Royal Society of Chemistry: Cambridge, UK, 2003; pp 99-100.

(2) Murov, S. L.; Carmichael, I.; Hug, G. L.; *Handbook of Photochemistry, 2nd Edition, Revised and Expanded*; Marcel Dekker, Inc.: NY, **1993**, p 9.

(3) Itoh, K.; Honda, K.; Sukigara, M. *Electrochimica Acta*. **1979**, *24*, 1195.

(4) (a) Phelps J.;Santhanam K. S. V.; Bard A. J. *J. Am. Chem. Soc.* **1967**, *89*, 1752; (b) Sioda, R. E. *J. Phys. Chem.* **1968**, *72*, 2322.

(5) Bard, A. J. *Electrogenerated Chemiluminescence,* Marcel Dekker, N.Y. 2004, p. 5.

(6) Shen, W.-J.; Dodda, R.; Wu, C.-C.; Wu, F.-I.; Liu, T.-H.; Chen, H.-H.; Chen, C. H.; Shu, C.-F. *Chem. Mater.* **2004**, *16*, 930.

(7) For reviews on ECL, see: (a) Richter, M. M. *Chem. Rev.* **2004**, *104*, 3003-3036; (b) Knight, A. W.; Greenway, G. M. *Analyst* **1994**, *119*, 879-890; (c) Faulkner, L. R.; Bard, A. J. *Electroanalytical Chemistry*; Marcel Dekker: New York, 1977; Vol. 10, p 1; (d) Bard, A. J.; Debad, J. D.; Leland, J. K.; Sigal, G. B.; Wilbur, J. L.; Wohlstadter, J. N. In *Encyclopedia of Analytical Chemistry: Applications, Theory and Instrumentation*; Meyers, R. A., Ed.; John Wiley & Sons: New York, 2000; Vol. 11, p 9842.

(8) (a) Keszthelyi C. P.; Bard, A. J. *Chem. Phys. Lett*. **1974**, *24*, 300. (a) Park, S. M.; Paffett, M. T.; Daub, G. H. *J. Am. Chem. Soc.* **1977**, *99*, 5394. (b) Choi, J.-P.; Wong, K.-T.; Chen, Y.-M.; Yu, J.-K.; Chou, P.-T.; Bard, A. J. *J. Phys. Chem. B.* **2003**, *107*, 14407.

(9) Werner, T.; Chang, J.; Hercules, D. *J. Am. Chem. Soc.* **1970**, *92*, 763.

(10) Birks, J. B. *Photophysics of Aromatic Molecules*; Wiley-Interscience: New York, 1970; Chapter 7.

(11) Bard, A.; Santhanam, K.; Maloy, J.; Phelps, J.; Wheeler, L. *Disc. Farad. Soc.* **1968**, *45*, 167.

(12) Chandross, E.; Longworth, J.; Visco, R. *J. Am. Chem. Soc.* **1965**, *87*, 3259.

(13) Park, M. Y.; Yang, S. G.; Jadhav, V.; Kin, Y. H. *Tetrahedron Letters*. **2004**, *45*, 4887.

(14) Sahami, S.; Weaver, M. *J. Electroanal. Chem.* **1981**, *122*, 155.

(15) (a) Rudolph, M. *J. Electroanal. Chem.* **2003**,*543,* 23; (b) Ruldolf, M. *J. Electroanal. Chem.* **2004**, *571*, 289; (c) Rudolph, M. *J. Electroanal. Chem.* **2003**, *558*, 171. (d) Rudolph, M. *J. Comp. Chem.* **2005**, *26*, 619; (e) Rudolph,

M. *J. Comp. Chem.* **2005**, *26*, 233; (f) Rudolph, M. *J. Comp. Chem.* **2005**, *26*, 1193.
(16) Kadish, K. M.; Ding, J. Q.; Malinski, T. *Anal. Chem.* **1984**, *56*, 1741.
(17) Collinson, M.; Wightman, M.; Pastore, P. *J. Phys. Chem.* **1994**, *98*, 11942. The reported value, 2×10^{10} $M^{-1}s^{-1}$ resulted in negative concentrations, but 10^{8} was deemed fast enough to adequately represent the data on the time scale of this experiment.
(18) Boens, N.; Qin, W.; Basaric, N.; Hofkens, J.; Ameloot, M.; Pouget, J.; Lefèvre, J.-P.; Valeur, B.; Gratton, E.; vandeVen, M.; Silva, N.; Engelborghs, Y.; Willaert, K.; Sillen, A.; Rumbles, G.; Phillips, D.; Visser, A.; van Hoek, A.; Lakowicz, J.; Malak, H.; Gryczynski, I.; Szabo, A.; Krajcarski, D.; Tamai, N.; Miura, A. *Anal. Chem.* **2007**, *79*, 2137.
(19) Bard, A. J.; Faulkner, L. R. *Electrochemistry: Fundamentals and Applications*; John Wiley & Sons: New York, NY, 2001; pp 245-246.
(20) Sioda, R. *J. Phys. Chem.* **1968**, *72*, 2322.
(21) Santhanam, K.; Bard, A. *J. Am. Chem. Soc.* **1966**, *88*, 2669.
(22) Faulkner, L. R.; Bard, A. J. *J. Am. Chem. Soc.* **1968**, *90*, 6284.

Chapter 5: Electrochemistry and Electrogenerated Chemiluminescence of (dppy)BTPA—a Bipolar, Solvatochromic Compound

5.1 Introduction

The bipolar molecule, (dppy)BTPA (Figure 5.1), consists of a 2,6-diphenolpyridine boron moiety[1] and a triphenylamine moiety. Molecular orbital calculations show that the dppy and Ph_3N act as electron donor and acceptor centers, respectively.[2] Their spatial separation lends strong charge transfer (CT) character to the excited state of (dppy)BTPA, resulting in highly solvatochromic emissions. This property, combined with the high electron and hole mobility of solid (dppy)BTPA, has been exploited to make an efficient, single-layer electroluminescent device.[3] They also make (dppy)BTPA an interesting candidate for electrogenerated chemiluminescence (ECL) studies.

ECL of organic molecules is typically brought about by reaction between a radical anion and cation to generate an emissive excited species.[4] The energy available for excited state generation is approximately equal to the enthalpy of annihilation: $-\Delta H^o = -\Delta G^o - T\Delta S^o$ ($T\Delta S^o \approx 0.1$ V). If $-\Delta H^o$ is greater than the energy of an excited state, E_S (singlet) or E_T (triplet), a molecule can achieve that state upon radical ion annihilation. If the singlet state is directly populated, the

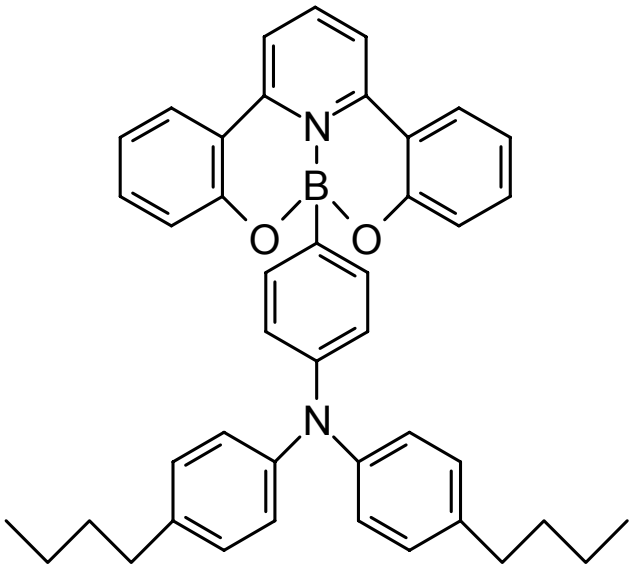

Figure 5.1. Structure of (dppy)BTPA

ECL mechanism is referred to as S-route ECL. If the triplet state is populated, triplet-triplet annihilation can occur to create a singlet state in what is known as T-route ECL. The radical ions are usually generated at a single electrode by alternately pulsing between oxidizing and reducing potentials. However, instability of either radical ion results in a rapid loss of ECL intensity with successive pulses. Using shorter pulse widths can overcome this problem by creating the other radical ion before the unstable one can decompose, but the RC time constant for charging the electrode surface limits the minimum pulse width. The use of small electrodes to reduce the time constant also lowers the overall light intensity.

If one radical ion is too unstable, ECL can also be generated with a coreactant, such as benzoyl peroxide (BPO), which forms a strong oxidizing agent (E^o = +0.8 V[5] or +1.5 V[6]) after being reduced.[7] This can react directly with the analyte anion and generate light without the radical cation. The general mechanism, using BPO, is give below:

$$BPO + e \rightarrow BPO^{\bullet -} \quad (5.1)$$

$$BPO^{\bullet -} \rightarrow C_6H_5CO_2^- + C_6H_5CO_2^{\bullet} \quad (5.2)$$

$$C_6H_5CO_2^{\bullet} + R^{\bullet -} \rightarrow C_6H_5CO_2^- + R^* \quad (5.3)$$

Solvatochromism is not often examined in ECL. Previous ECL studies of CT emitters have focused on quantum efficiencies and electron transfer rates of a

variety of molecules,[8] as well as the effects of solvent[9] and electrolyte.[10] However, these studies do not explore the solvatochromic shift of the ECL. The photoluminescence of (dppy)BTPA exhibits a linear bathochromic shift with respect to increasing solvent polarizability,[11] which permits comparison between efficiencies and emission wavelengths for the ECL and (dppy)BTPA.

In this paper, we investigate the ECL of (dppy)BTPA and compare the solvatochromic shift and quantum efficiency trends to those of the PL. In the process, we employ cyclic voltammetry to examine the stability of the radical ions and the mechanism of their decomposition.

5.2 Experimental

5.2.1 Materials

Anhydrous MeCN was obtained from Aldrich (St. Louis, MO) and transferred into a helium atmosphere drybox (Vacuum Atmospheres Corp., Hawthorne, CA) without further purification. Anhydrous benzene was obtained from Aldrich and distilled under vacuum to remove an electroactive impurity before being transferred to the drybox. All other solvents were obtained from Fisher (Fair Lawn, NJ) or Aldrich and used as received. Electrochemical grade tetra-*n*-butylammonium perchlorate (TBAP) was obtained from Fluka and transferred directly into the drybox. The compound, (dppy)BTPA, was synthesized according to literature procedures.[3] Benzoyl peroxide (BPO) was obtained from Aldrich and used as received.

5.2.2 Characterization

The electrochemical cell for cyclic voltammetry (CV) and ECL transients consisted of a 1.5 mm Pt disk inlaid in glass as the working electrode (WE), a coiled, Pt wire as the counter electrode (CE), and a Ag wire quasi-reference electrode (QRE). The potential of the QRE was calibrated by using ferrocene (0.342 V vs SCE) as an internal standard.[12] Before each experiment, the WE was polished with 0.3 μm alumina (Buehler, Ltd., Lake Bluff, IL), then sonicated in water, followed by ethanol, for 1 min each. The electrode was then rinsed with acetone before being transferred into the dry box. For ECL spectra, the working electrode was a 1.5 mm Pt disk inlaid in glass and bent at a 90˚ angle so the electrode surface faced the detector. A 25 μm ultramicroelectrode (UME) polished using 0.05 μm alumina was used for steady-state and fast scan experiments.

All solutions for electrochemical measurements consisted of 0.1 M TBAP as the supporting electrolyte and 1 mM (dppy)BTPA (except where otherwise noted) in various ratios of benzene to MeCN. Solutions were prepared inside the dry box. For measurements made outside of the box, the electrochemical cell was closed with a Teflon cap sealed with a rubber O-ring. Stainless steel rods driven through the cap formed the electrode connections. Cyclic voltammograms were performed using a CH Instruments Model 660 Electrochemical Workstation (Austin, TX).

Digital simulations of cyclic voltammograms were performed using the DigiElch software package [13] and DigiSim (Bioanalytical Systems). The uncompensated resistance and capacitance were determined from the current-time curve for a potential step in a non-faradaic potential region of the background solution. The diffusion coefficient of (dppy)BTPA (D = 5.8 $\times 10^{-6}$ cm^2/s) was obtained by averaging the D obtained from a potential step experiment with that obtained from the peak currents of CVs performed at scan rates from 50 mV/s to 10 V/s. For simulations, all products of the electrochemical processes were assigned the same diffusion coefficient as (dppy)BTPA. The electrode surface area was determined from a Cottrell plot of a potential step experiment in 1 mM ferrocene in MeCN ($D = 1.2 \times 10^{-5}$ cm^2/s).[14]

For spectroscopy, (dppy)BTPA solutions were prepared in a 1 cm quartz cell. Absorbance spectra were collected on a DU 640 spectrophotometer (Beckman, Fullerton, CA). Fluorescence spectra were collected on a QuantaMaster Spectrofluorimeter (Photon Technology International, Birmingham, NJ). The excitation source was a 70W xenon lamp, and the slits for excitation and emission were 0.2 mm for all samples, except those in MeCN and DMSO, which used 1 mm. Quantum efficiencies were determined with respect to $Ru(bpy)_3^{2+}$ ($\Phi_{PL} = 0.075$).[15]

To generate ECL, the working electrode was pulsed at 5 Hz between potentials 80 mV beyond the diffusion-limited peak potentials, E_p, corresponding

to the reduction and oxidation of (dppy)BTPA. Coreactant ECL experiments were performed with 1 mM (dppy)BTPA, 10 mM BPO, and 0.1 M TBAP in MeCN, and the pulses were between 0 V and $E_{p,red}$ – 0.08 V. The potential pulses were generated by an Eco Chemie Autolab potentiostat (The Netherlands). Spectra were collected on a Princeton Instruments Spec-10 CCD Camera (Trenton, NJ) with an Acton SpectraPro-150 monochromator (Acton, MA). The integration time for all spectra was 5 min. ECL spectra were calibrated using a Hg/Ar pen-ray lamp from Oriel (Stratford, CT). ECL transients were obtained by connecting the Autotolab potentiostat to the output of a power meter for a photomultiplier tube (PMT, Hamamatsu R4220p, Japan) placed beneath the working electrode. The PMT was supplied with -750 V from a high voltage power supply Series 225 (Bertan High Voltage Corp., Hucksville, NY).

ECL efficiencies were estimated from current-normalized peak light intensities (averaged if the peaks varied in height) of the transients. $Ru(bpy)_3^{2+}$ was used as the ECL standard with excited state generation efficiency $\Phi_{ECL,Ru} \approx 0.65$ at 25˚C.[15] All ECL efficiency experiments were performed with a UME pulsed at 5 Hz between the oxidation and reduction potentials of the analyte, which yielded the optimum light intensity in the most resistive solution. ECL efficiency will be described by two quantities: ECL quantum yield, $\Phi_{ECL,QY}$, which refers to photons emitted per electron transfer event, and ECL quantum

efficiency, Φ_{ECL}, which refers to excited states created per electron transfer. Both are defined as:

$$\Phi_{ECL,QY} = \frac{Ii_S}{I_S i}\Phi_{ECL,S}\Phi_{PL,S} \quad (5.4)$$

$$\Phi_{ECL} = \frac{I_X i_S \Phi_{PL,S}}{I_S i_X \Phi_{PL,X}}\Phi_{ECL,S} \quad (5.5)$$

where the subscript *s* refers to the ECL/PL standard, and the letters with no subscript refer to the analyte of interest. *I* refers to the light intensity measured by the power meter, and *i* refers to the observed faradaic current.

Bulk electrolysis was performed in a 3-compartment cell, with the compartments separated by fine porosity glass frits. The WE was a Pt wire grid placed in the first compartment. The RE, a Pt wire coated with polypyrrole,[16] was separated from the analyte solution by a glass tube sealed with a cracked glass junction. A magnetic stir bar was used to maintain uniform analyte concentration in the solution. The counter electrode was a Pt mesh placed in the third compartment. Each compartment contained MeCN with 0.1 M TBAP as the supporting electrolyte. The solution was electrolyzed for 15 min (until the current became constant) at $E_{p,red}$ – 100 mV.

5.3 Results and Discussion

5.3.1 Electrochemistry

Cyclic voltammetry was used to assess the energy of annihilation and determine the stability of the (dppy)BTPA radical ions in solution. A cyclic

voltammogram of (dppy)BTPA in MeCN is shown in Figure 5.2. The oxidation is a one-electron process occurring at E_{ox}^{o} = 0.72 V vs SCE that is reversible at scan rates, v, as low as 50 mV/s, indicating stable radical cations. According to MO calculations, the HOMO, and hence the oxidation site, is mainly localized over the triphenylamine moiety.[3] The unusual stability of the radical cation may be attributed to the (dppy)B and butyl substituents at the para positions of each phenyl on the nitrogen, which prevent the dimerization reactions that typically accompany phenylamine oxidation.[17,18]

The reduction wave peak height is essentially the same as that of the oxidation, hence it is also assigned as a one-electron process occurring at E_{red}^{o} = -1.72 V vs SCE. However, the reduction is less chemically reversible than the oxidation. In Figure 5.3, a plot of the anodic-to-cathodic peak current ratio (i_{pa}/i_{pc}) vs. v for various concentrations shows that for lower concentrations, i_{pa}/i_{pc} approaches unity at lower scan rates than for high concentrations, indicating greater radical anion stability at lower concentrations. Concentration-dependent reversibility implies an EC process in which a dimerization reaction follows the electrochemical step:

$$(dppy)BTPA + e \rightarrow (dppy)BTPA^{\bullet -} \qquad (5.6)$$

$$2(dppy)BTPA^{\bullet -} \rightleftharpoons [(dppy)BTPA]_2^{2-} \qquad (5.7)$$

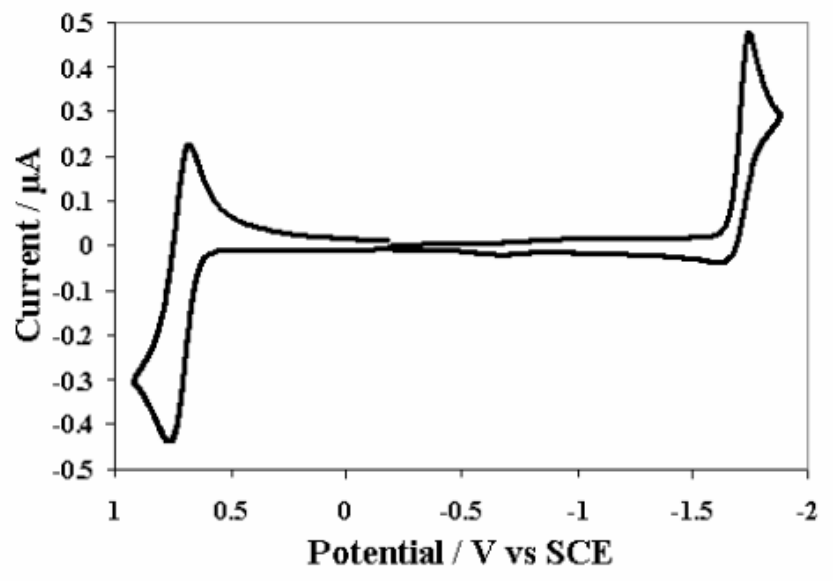

Figure 5.2. Cyclic voltammogram of 1 mM (dppy)BTPA in acetonitrile with 0.1 M TBAP at v = 50 mV/s. E_{ox}^{o} = 0.72 V vs SCE, E_{red}^{o} = -1.72 V vs SCE, k^{o} = 1.8×10^{4} $M^{-1}s^{-1}$.

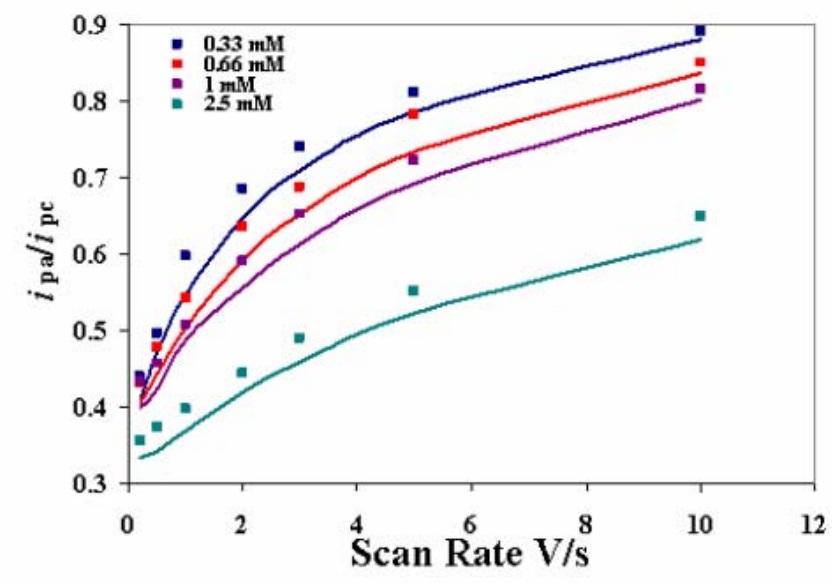

Figure 5.3. Experimental (squares) and simulated (lines) scan rate dependence of the peak current ratio of the (dppy)BTPA reduction wave at various concentrations.

CV simulations (Figures 5.4-5.7) using $K_{eq} = 10^5$ M^{-1} and $k_7 = 1.8\times10^4$ $M^{-1}s^{-1}$ for the dimerization reaction (5.7) are in good agreement with the experimental data for v = 0.05-10 V/s over the concentration range 0.33 mM to 2.5 mM.

After scan reversal of the reduction wave at scan rates where the $A^{\bullet-}$ oxidation wave is small, a second oxidation wave appears with a peak potential of -0.59 V vs SCE (Figure 5.8). The dimer created in (5.7) may undergo another following reaction, possibly with an impurity, X, that results in a species of lower oxidation potential.

Additional information is obtained from reductive bulk electrolysis. After electrolysis, the light yellow solution of (dppy)BTPA converts to dark blue over the course of several hours. Seconds after exposure to air, the blue solution reverts to the yellow color of (dppy)BTPA. A mass spectrum of the electrolyzed compound after exposure to air shows a parent peak at the molecular weight of (dppy)BTPA, indicating reversal of the reduction and any following reactions. The difficulty of performing MS and NMR analysis while maintaining an inert atmosphere prevented us from analyzing the electrolysis product directly. Since oxidation in air yields the starting material, the -0.59 V oxidation peak may also be a conversion of the product back to the starting material. This data can be described by adding the following reactions to the dimerization:

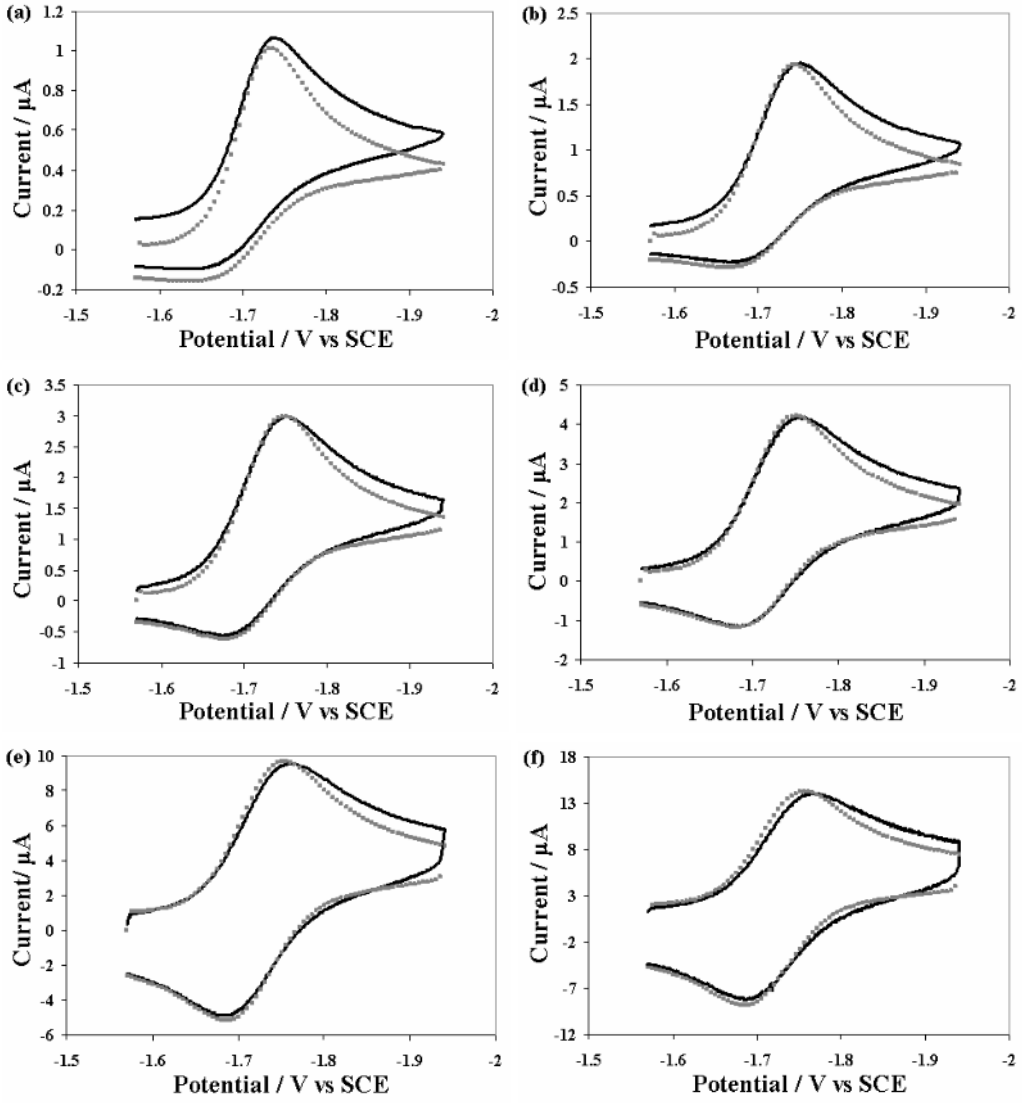

Figure 5.4. Experimental (black lines) and simulated (grey dots) CVs of 0.33 mM (dppy)BTPA in MeCN at (a) 0.05, (b) 0.2, (c) 0.5, (d) 1, (e) 5, and (f) 10 V/s.

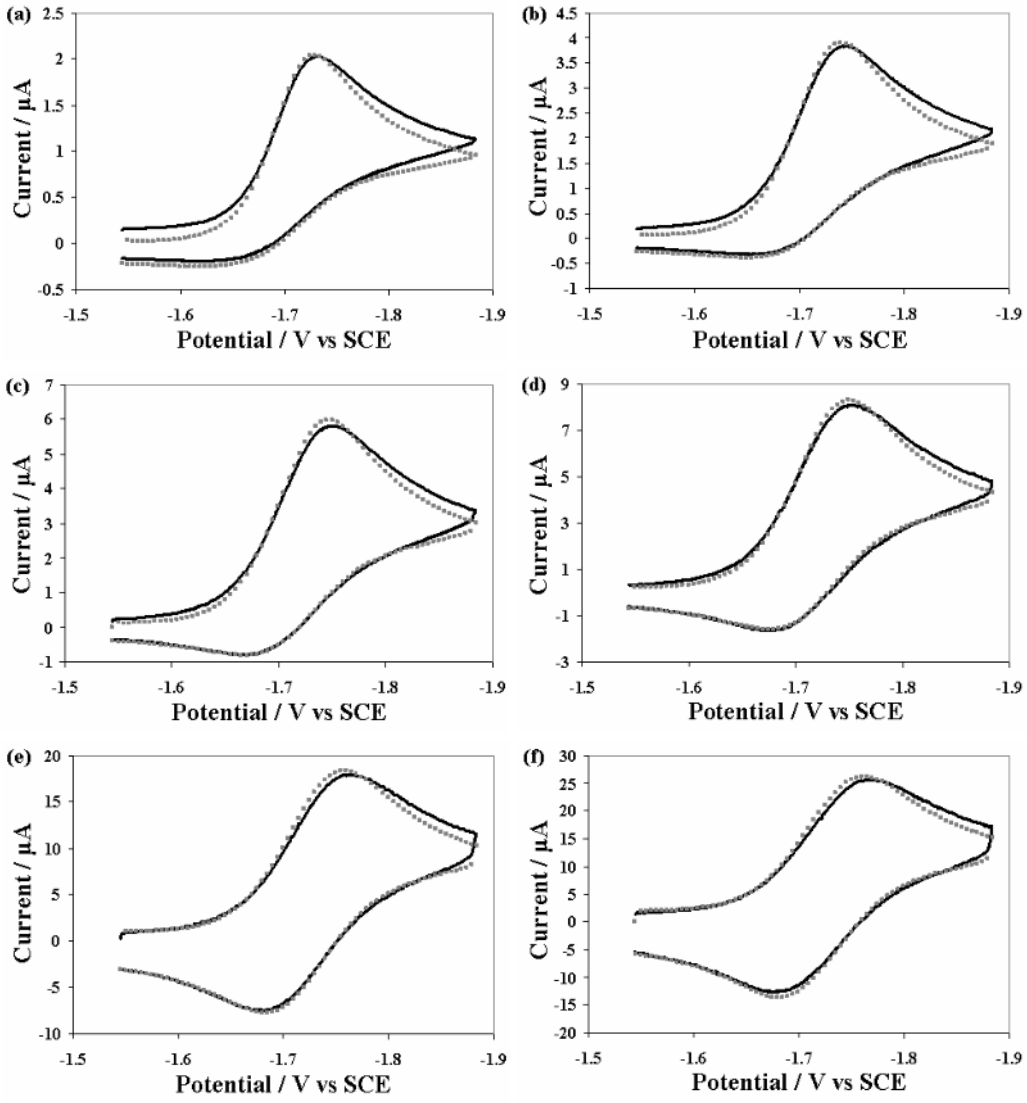

Figure 5.5. Experimental (black lines) and simulated (grey dots) CVs of 0.66 mM (dppy)BTPA in MeCN at (a) 0.05, (b) 0.2, (c) 0.5, (d) 1, (e) 5, and (f) 10 V/s.

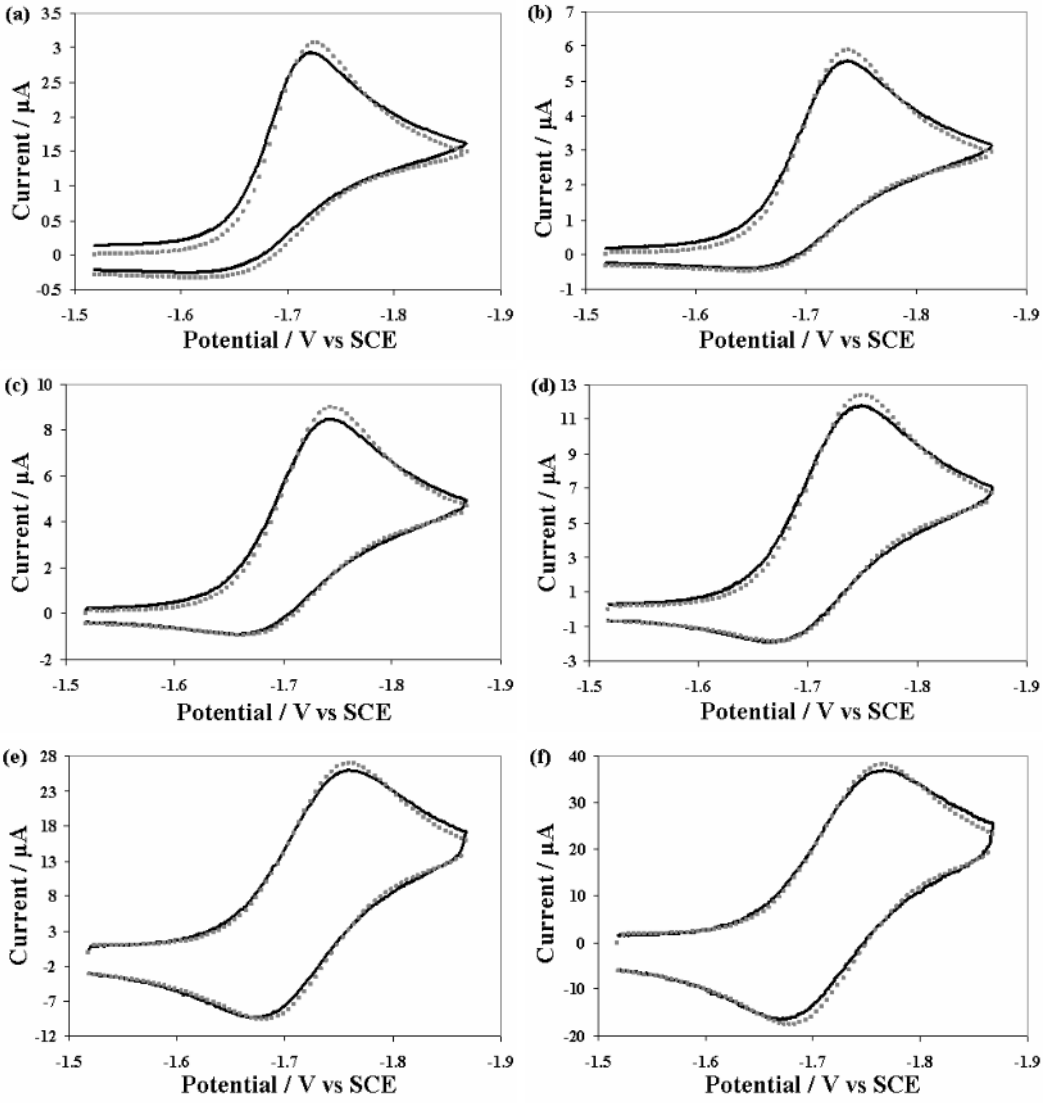

Figure 5.6. Experimental (black lines) and simulated (grey dots) CVs of 1 mM (dppy)BTPA in MeCN at (a) 0.05, (b) 0.2, (c) 0.5, (d) 1, (e) 5, and (f) 10 V/s.

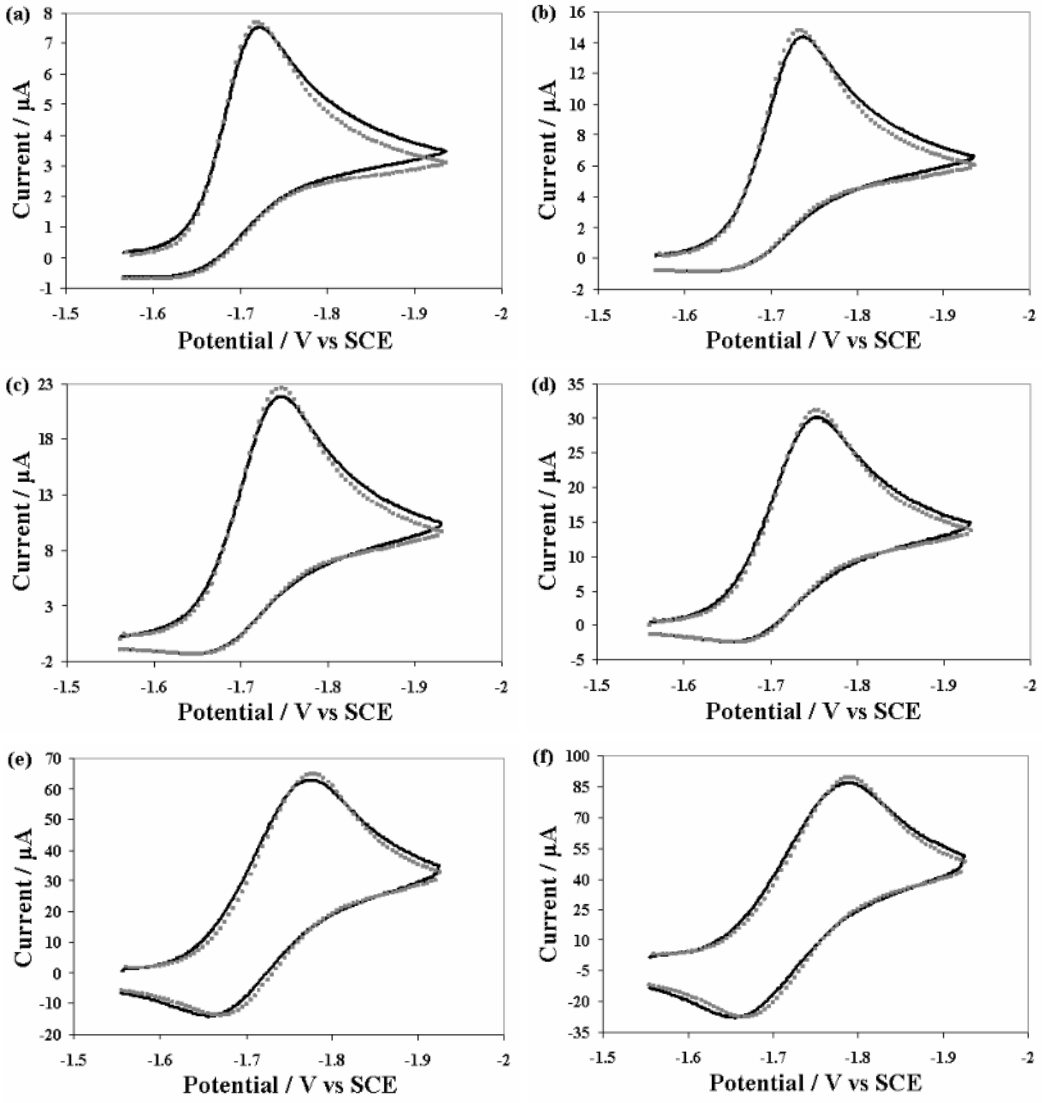

Figure 5.7. Experimental (black lines) and simulated (grey dots) CVs of 2.5 mM (dppy)BTPA in MeCN at (a) 0.05, (b) 0.2, (c) 0.5, (d) 1, (e) 5, and (f) 10 V/s.

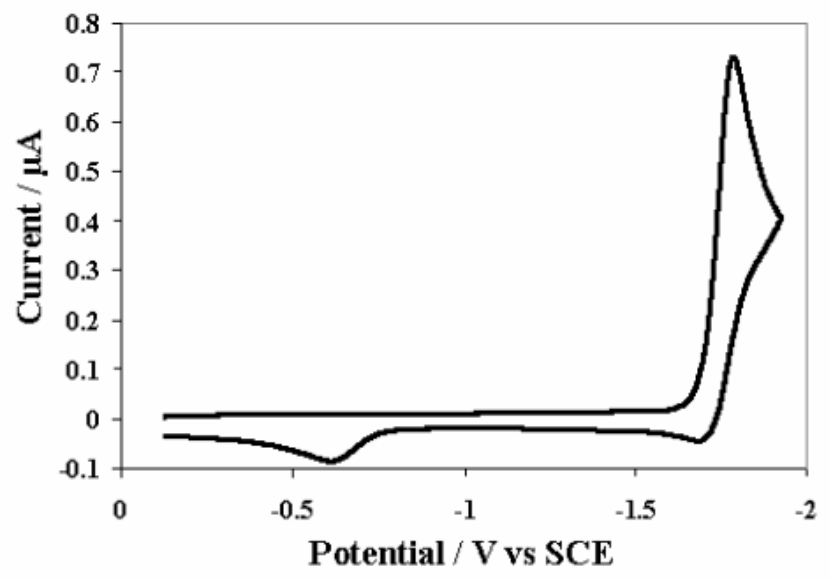

Figure 5.8. Reduction of 1 mM (dppy)BTPA in MeCN with 0.1 M TBAP. Second reverse wave appears at -0.59 V vs SCE.

$$[(dppy)BTPA]_2^{2-} \rightleftharpoons P \quad (5.8)$$

$$[(dppy)BTPA]_2^{2-} + X \rightleftharpoons [(dppy)BTPA]_2X^{2-} \quad (5.9)$$

$$[(dppy)BTPA]_2X^{2-} \rightarrow [(dppy)BTPA]_2X^{-} + e \quad (5.10)$$

$$[(dppy)BTPA]_2X^{-} \rightleftharpoons [(dppy)BTPA]X^{-} + (dppy)BTPA \quad (5.11)$$

$$[(dppy)BTPA]X^{-} \rightarrow [(dppy)BTPA]X + e \quad (5.12)$$

$$[(dppy)BTPA]X \rightleftharpoons (dppy)BTPA + X \quad (5.13)$$

The simulated and experimental data are compared in Figure 5.9. In the above mechanism, P represents a product generated in competition with Equation (5.9). While Equation (5.8) is not discussed in chemical terms, its inclusion is necessary to accurately simulate the cyclic voltammogram at low *v*. However, the same simulation results can be created if P is a product of $[(dppy)BTPA]_2X^{2-}$ decomposition. The simulated impurity, X, was assigned a concentration of 3 μM. Since X has not been identified, the actual reaction may not be as described in (5.9), but the close fit of the data suggests that the overall mechanism is correct. Product formation for reactions (5.8), (5.9), and (5.11) was treated as highly favorable and assigned K_{eq} of 10^5, regardless of their units. The rate constants assigned to these reactions are $k_8 = 0.045\ s^{-1}$, $k_9 = 10^8\ M^{-1}s^{-1}$, $k_{11} = k_{13} = 10^5\ s^{-1}$. Rate constants k_{11} and k_{13} were chosen arbitrarily, and only k_8 and k_9 were adjusted to fit the data. The first oxidation potential, $E_{10}^{o} = -0.55$ V vs SCE was

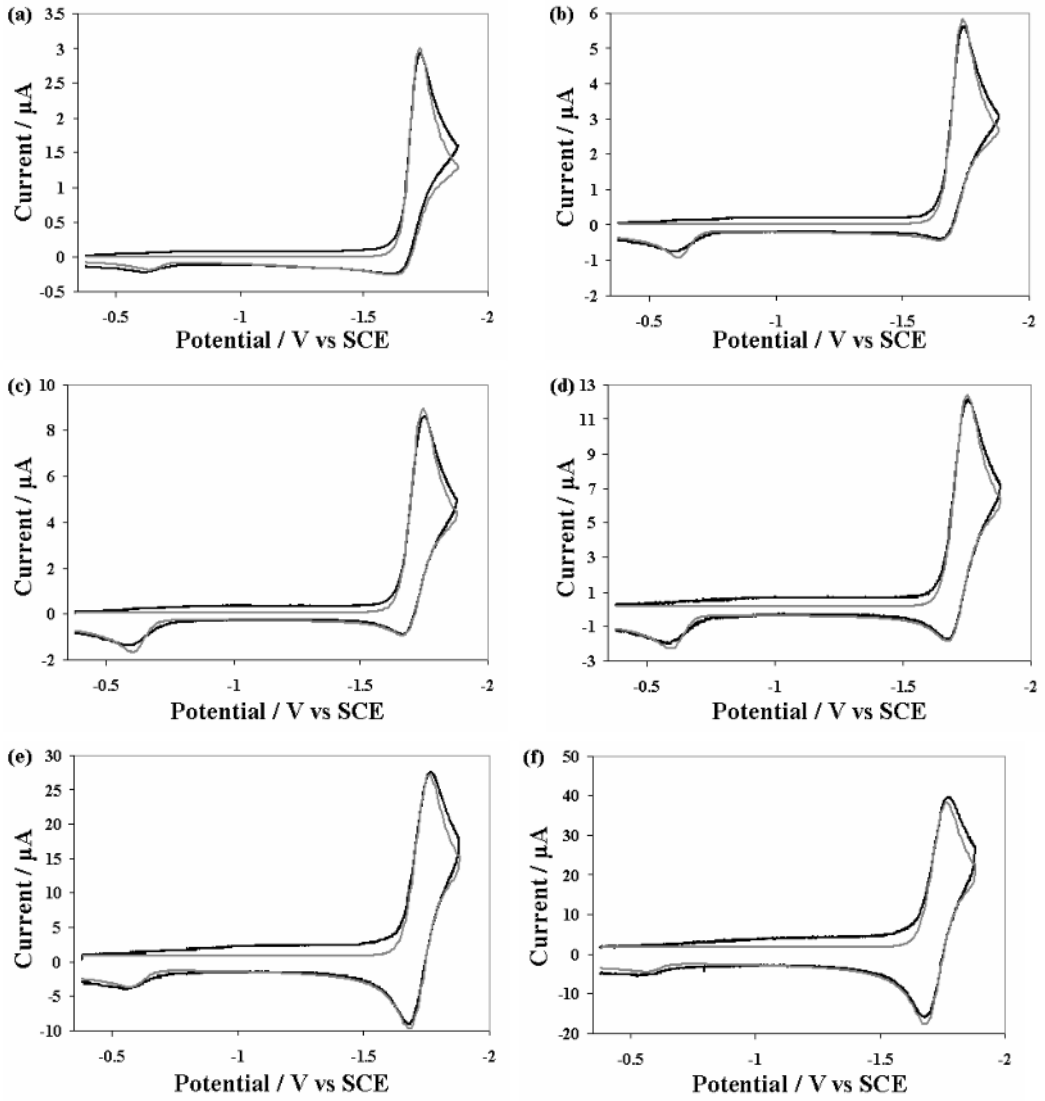

Figure 5.9. Experimental (black lines) and simulated (grey lines) CVs of the reduction of 1mM (dppy)BTPA in MeCN and both of its oxidations. Scan rates are (a) 0.05, (b) 0.2, (c) 0.5, (d) 1, (e) 5, and (f) 10 V/s.

adjusted to fit the data, while E_{12}^{o} = -1 V was assigned arbitrarily to create an ECE reaction. A 2-electron oxidation creates peaks that are too narrow to fit the data, and a 1-electron process does not generate sufficient current, even at high concentrations of X.

5.3.2 Spectroscopy

In pure MeCN, the absorbance spectrum of (dppy)BTPA, consists of a broad peak at 301 nm and a shoulder at 374 nm ($\varepsilon = 1.1\times10^{4}$ $M^{-1}cm^{-1}$), which are attributed to absorption to the LUMO+4 and LUMO levels, respectively.[19] The absorbance spectra displayed little dependence of peak location on solvent polarizability, as shown in Figure 5.10. The long wavelength absorbance peak varied from 374 nm in pure MeCN to 382 nm in pure benzene. Absorbance of (dppy)BTPA in CCl_4 is unique because the LUMO and LUMO+4 peaks are the same height.

The absorbance spectrum of the electrolysis reduction product, shown in Figure 5.11, features a peak at 301 nm similar to that of (dppy)BTPA, and additional peaks at 525, 569, and 612 nm. Excitation at those wavelengths yields no detectable luminescence. After exposure to air, the long-wavelength absorbance peaks disappear, and the 374 nm shoulder seen in (dppy)BTPA returns, indicating that the compound has reverted to its pre-electrolysis state. The (dppy)BTPA fluorescence exhibits a strong bathochromic shift and a decrease in intensity as the solvent polarizability increases, as shown in Figure

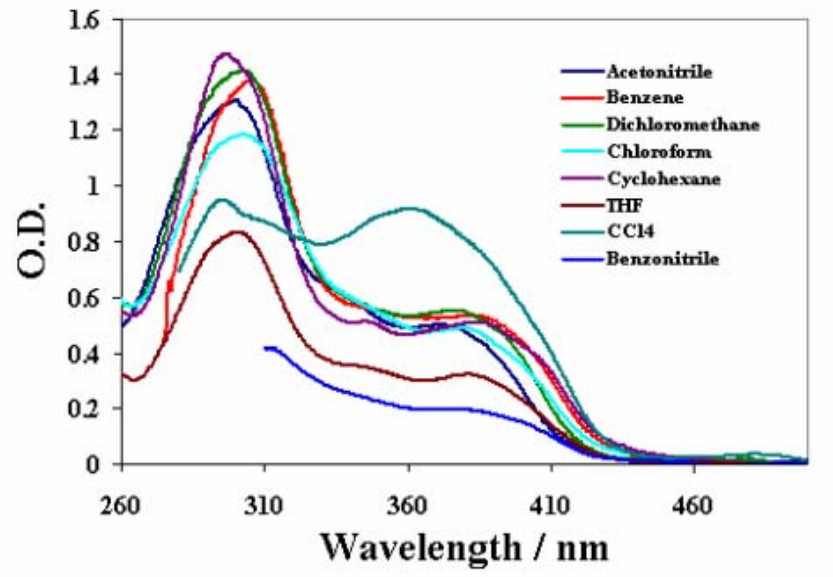

Figure 5.10. Absorbance spectra of 50 μM (dppy)BTPA in various solvents.

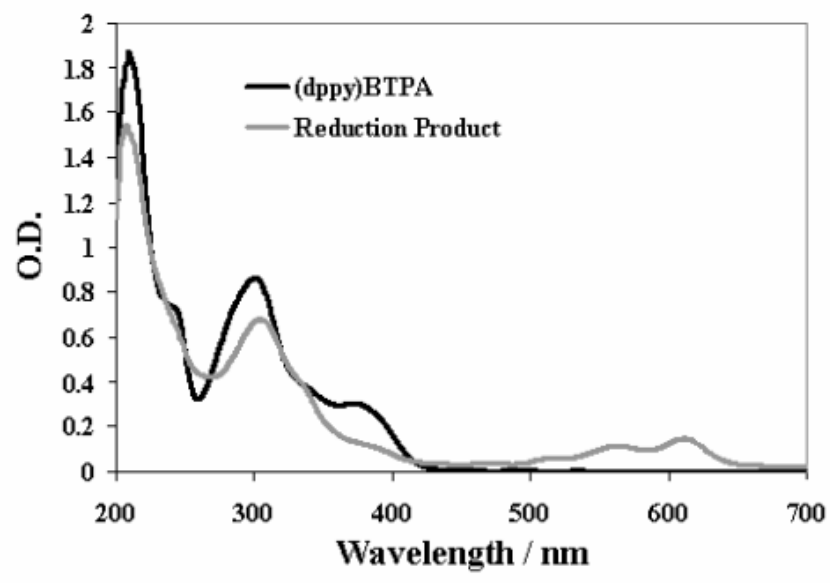

Figure 5.11. Absorbance spectra of (dppy)BTPA and its reduction product. Concentration ca. 25 μM.

5.12.

In most solvents, the Stokes' shift of (dppy)BTPA can be described using the Lippert Equation, which models the solvent relaxation of a molecule in an electronic excited state by the solvent polarizability.[11] The polarizability, Δf, is a function of the dielectric constant, ε, and refractive index, n. Solvent orientation has a greater effect on excited state energy for molecules with a strong dipole moment in the excited state, so CT emitters such as (dppy)BTPA are expected to have large Stokes' shifts, as shown by the Lippert Equation:

$$\bar{\nu}_a - \bar{\nu}_f \cong \frac{2}{hc}\frac{(\mu^* - \mu)^2}{a^3}\Delta f + const \qquad (4.14)$$

With the polarizability parameter,

$$\Delta f = \frac{\varepsilon - 1}{2\varepsilon + 1} - \frac{n^2 - 1}{2n^2 + 1} \qquad (4.15)$$

$\bar{\nu}_a$ and $\bar{\nu}_f$ are the absorbance and fluorescence wavenumbers, respectively, h is Plank's constant, c is the speed of light, a is the radius of the solvent cavity, and μ and μ^* are the ground and excited state dipole moments. The data are given in Table 5.1. For pure solvents, literature values of ε and n were used;[20] for mixed solvents, they were calculated using linear combinations of n and ε based on the volume fraction of each solvent. A linear fit to the data was obtained in all solvents except CCl_4 and cyclohexane, which deviate significantly from the other

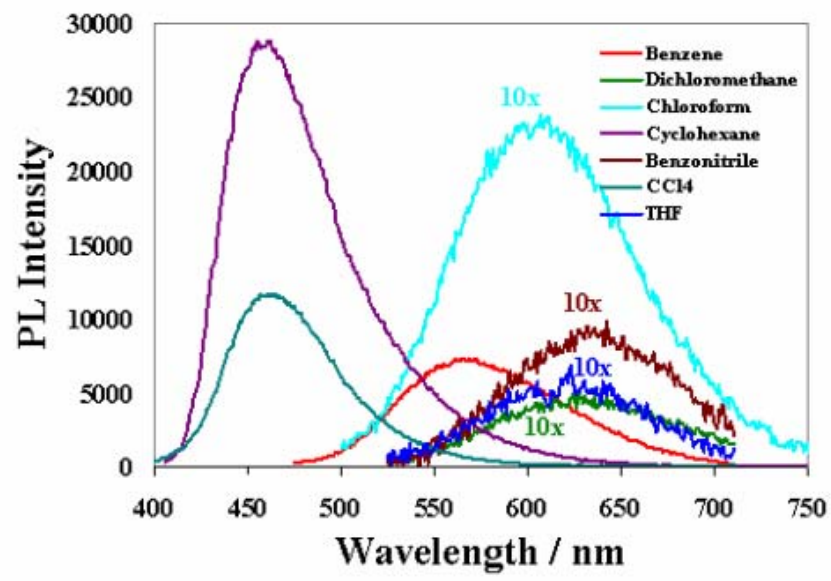

Figure 5.12. PL spectra of 10 μM (dppy)BTPA in various solvents. Spectra obtained in $CHCl_3$, benzonitrile, THF, and CH_2Cl_2 are magnified for clarity. Luminescence was not detected for (dppy)BTPA in acetonitrile under the concentration/slit width conditions used here.

Table 5.1. Absorbance and photoluminescence data for (dppy)BTPA in various solvents, and the properties of the solvents listed in order of decreasing solvent polarizability (Δf).

Solvent	λ_{abs} / **nm**	λ_{PL} / **nm**	Φ_{PL}	ε	n	Δf	$\Delta \bar{\nu}$ / 10^3 cm^{-1}
Acetonitrile[a]	374	654	0.00086	36.64	1.3442	0.3049	11.7
DMSO[a]	376	650	0.0012	47.24	1.4793	0.2633	11.6
1:1[a]	376	642	0.0042	19.46	1.4227	0.2596	11.2
Benzonitrile	377	634	0.051	25.9	1.5289	0.236	10.9
3:1[a]	377	628	0.020	10.87	1.4619	0.2184	10.8
CH_2Cl_2	378	628	0.024	8.93	1.4242	0.217	10.7
THF	382	626	0.029	7.52	1.405	0.210	10.3
9:1[a]	379	611	0.068	5.718	1.4854	0.1565	10.2
$CHCl_3$	380	606	0.13	4.8069	1.4459	0.14818	10.0
19:1[a]	381	599	0.12	4.000	1.4932	0.1081	9.7
CCl_4[b]	363	461	0.66	2.2379	1.4601	0.011034	6.1
Benzene[a]	382	564	0.40	2.2825	1.5011	0.0028580	8.8
Cyclohexane[b]	387	458	1.0[c]	2.0243	1.4235	-0.000240	4.3

[a]Φ_{PL} of these solvents was determined with respect to $Ru(bpy)_6(PF_6)_2$ in acetonitrile. All other Φ_{PL} were determined later, using (dppy)BTPA in benzene as the standard.

[b]These solvents deviate from the Stokes shift-polarizability trend.

[c]Rounded down from a measured value of 1.6. Impossible measured Φ_{PL} attributed to large error in successive normalizations.

solvents (Figure 5.13). The deviation could be due to scattering or the inability of the Lippert equation to account for specific interactions between the chromophore and the solvent. Since the electrolyte is insoluble in CCl_4 and cyclohexane, comparison between PL data and ECL data requires best fit lines that exclude the two outlying points. However, if the deviation is merely data scattering, the two points should be included, so the data has been plotted both ways. The cavity radius is estimated from x-ray data for (dppy)BTPA[3] to be 6 Å, which yields $\mu^* - \mu$ = 13 D if CCl_4 and cyclohexane are excluded from the fit, and 18 D if they are included. Both values are within the 9 D to 44 D range of $\mu^* - \mu$ reported for other chromophores.[11]

The significant quenching that accompanies the bathochromic shift in the spectra is not understood, and may consist of several factors. The primary contributor appears to be the energy gap law, which states that the non-radiative decay rate increases as the HOMO-LUMO energy gap decreases.[21] Plotting the fluorescence intensity against either solvent polarizability or viscosity did not yield a linear correlation. The apparent randomness of fluorescence intensity as a function of solvent viscosity rules out a twisted intramolecular charge transfer state as a quencher.[22] Furthermore, a solution of (dppy)BTPA in 60%/40% methanol/glycerol exhibited only 2× enhancement over (dppy)BTPA in pure methanol, whereas the lower viscosity 1:1 PhH/MeCN solutions lend a 5× enhancement in (dppy)BTPA emission over that of pure MeCN (Figure 4.14). On

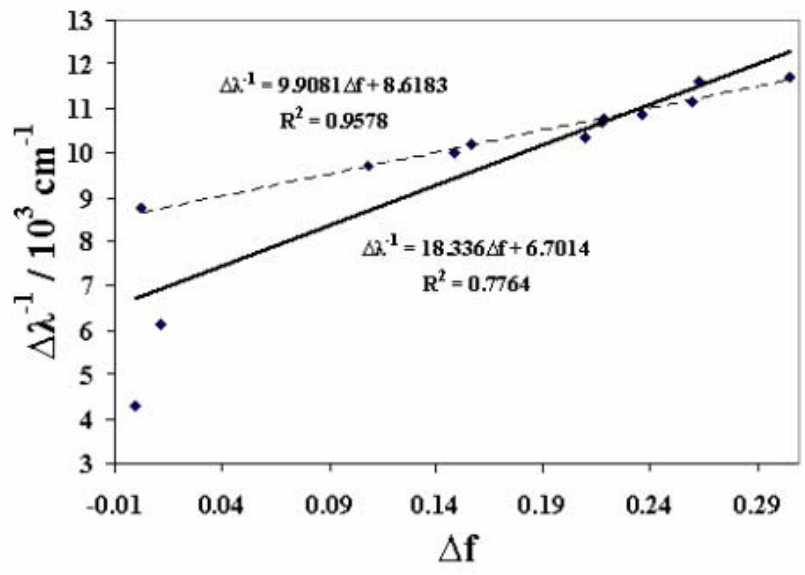

Figure 5.13. Lippert plot for (dppy)BTPA in various solvents without TBAP. The solid line fits all data points ($\mu^* - \mu$ = 18 D), and the dotted line fits all the data except CCl_4 and cyclohexane ($\mu^* - \mu$ = 13 D).

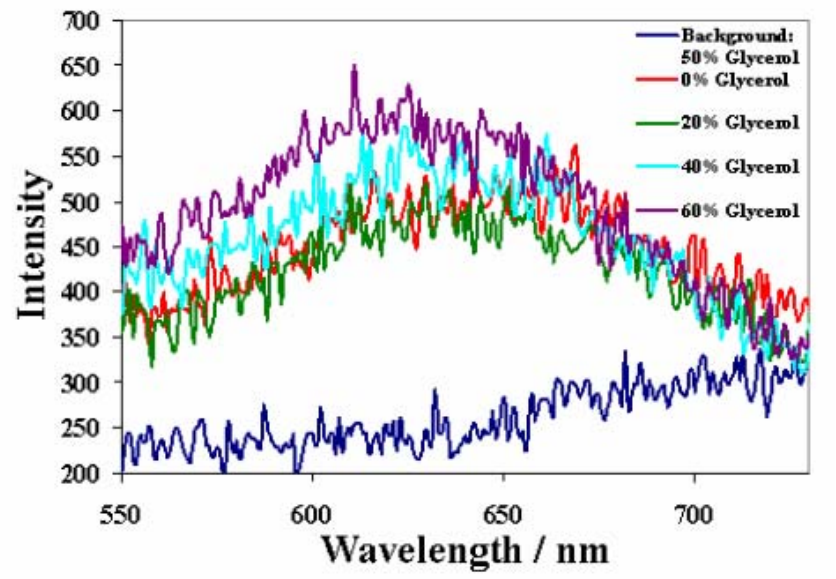

Figure 5.14. PL of 38 μM (dppy)BTPA in various methanol/glycerol (v/v) solutions.

the other hand, the addition of glycerol increases the polarizability of the glycerol-methanol solutions (Δf of glycerol = 0.74; Δf of methanol = 0.31), so the small enhancement contradicts the luminescence trend with respect to solvent polarizability, suggesting that viscosity does have a small effect. Adventitious water and oxygen are not significant quenchers, as MeCN solutions prepared in atmosphere are as luminescent as those prepared in the dry box. Strong PL quenching and a small bathochromic shift are also observed when the electrolyte, TBAP, is added to the solution (Figure 5.15). Both effects are attributed to both the increased solvent dielectric and specific interaction of the salt with the chromophore in a CT state.[23]

5.3.3 Electrogenerated Chemiluminescence (ECL)

The electrogenerated chemiluminescence of (dppy)BTPA was examined in solvents composed of various ratios of PhH to MeCN to examine the solvatochromism of the ECL. Table 5.2 summarizes the λ_{max}, quantum efficiency, and ECL data in the presence of 0.1 M TBAP. Intenssity-normalized spectra are shown in Figure 5.16. E_s was estimated as $hc(\bar{\nu}_a + \bar{\nu}_f)/2$.[24] According to these estimates, the annihilation energy is not sufficient to directly populate the excited singlet state, so the ECL must occur via T-route. $\Phi_{ECL,QY}$ increases as solvent polarizability decreases, following the trend observed for Φ_{PL}. However, Φ_{ECL} decreases when the PhH/MeCN ratio is greater than 1:1, though this may be due to the greater RC time constant and *i*R drop of low dielectric solvents.

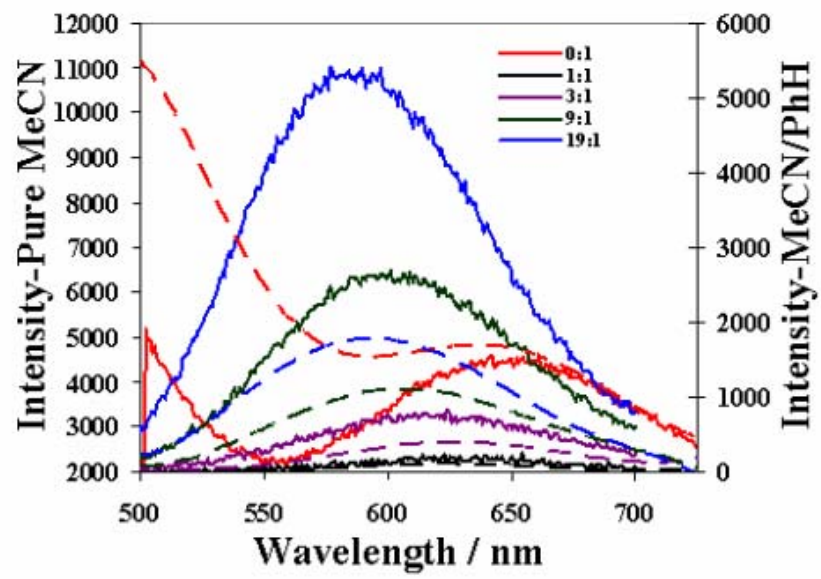

Figure 5.15. Fluorescence spectra of 10 μM (dppy)BTPA in various ratios of benzene:acetonitrile with (dotted lines) and without (solid lines) 0.1 M TBAP. Slit width for all mixed solvents was 0.2 mm. Slit width for pure MeCN data was 1 mm.

Table 5.2. ECL data for 1 mM (dppy)BTPA in various ratios of PhH/MeCN. PL data was obtained in solutions with 0.1 M TBAP.

	λ_{PL} / nm	λ_{ECL} / nm	E_s / eV	ΔH_{ann} / eV	Φ_{PL}	Φ_{ECL}	$\Phi_{ECL,QY}$
0:1	654	690	2.59	2.34	0.00086	0.075	2.8×10^{-5}
1:1	638	670	2.61	2.42	0.0042	0.23	2.7×10^{-4}
3:1	634	657	2.62	2.50	0.020	0.15	6.4×10^{-4}
9:1	616	646	2.64	2.49	0.068	0.12	0.0015
19:1	604	637	2.65	2.54	0.12	0.078	0.0015

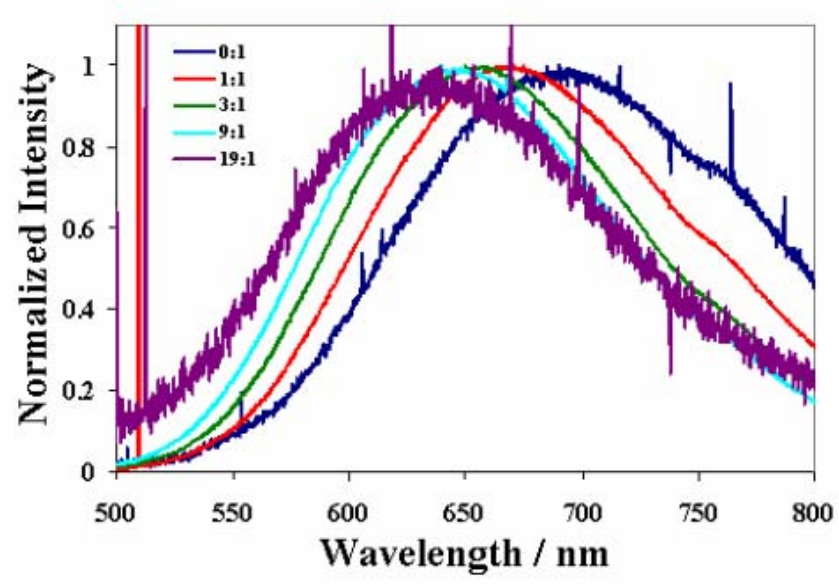

Figure 5.16. Normalized ECL spectra of (dppy)BTPA in various ratios of PhH/MeCN.

The ECL spectra exhibit the same solvatochromic shift as the PL spectra. The ~30 nm offset between the PL and ECL λ_{max} (Figure 5.17, Spectra in Figure 5.18) is attributed to an instrumental artifact, since $\lambda_{max,PL} = \lambda_{max,ECL}$ when the CCD camera was used as a detector for photoluminescence of (dppy)BTPA in 19:1 PhH/MeCN excited by a Hg/Ar lamp (Figure 5.19). Since absorbance is not relevant to ECL, $\bar{\nu}_f$, rather than the Stokes' shifts, is plotted against Δf. Since $\bar{\nu}_a$ is fairly constant, this should have little effect on the slope. The values for $\mu^* - \mu$ are 11 D for the PL plot and 10 D for the ECL plot.

The ECL spectra show solvent-independent emission beyond 725 nm that is not present in the PL spectra. Long wavelength features specific to ECL usually originate from annihilation phenomena, such as exciplex formation brought about by the proximity of the radical ions, reaction of a radical ion with an impurity, or emission from an intermediate or side product. However, this emission was also observable at the same relative intensity when BPO was used as a coreactant with (dppy)BTPA to generate emission without annihilation. On the other hand, annihilation can still occur if the coreactant oxidizes the analyte, so this is not conclusive.[25]

The strong dipole moment in the excited state and the proximity of two radical ions during annihilation are conducive to exciplex formation. Emission from a side product cannot be ruled out, however, since $[(dppy)BTPA]_2X^{2-}$ may

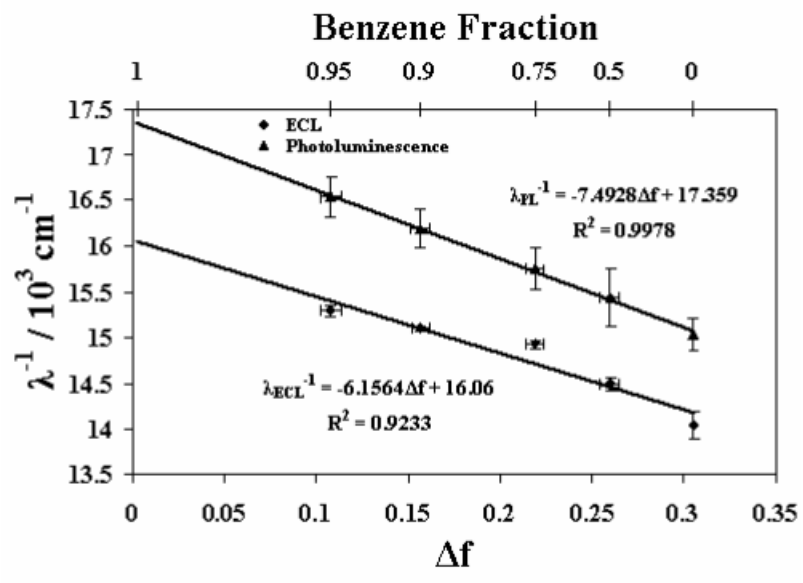

Figure 5.17. Lippert plots for PL and ECL of (dppy)BTPA in various mixtures of benzene/acetonitrile with 0.1 M TBAP. The y-axis is the fluorescence wavenumber rather than the Stokes shift, since ECL has no absorbance. $\mu^* - \mu =$ 11 D for PL and 10 D for ECL.

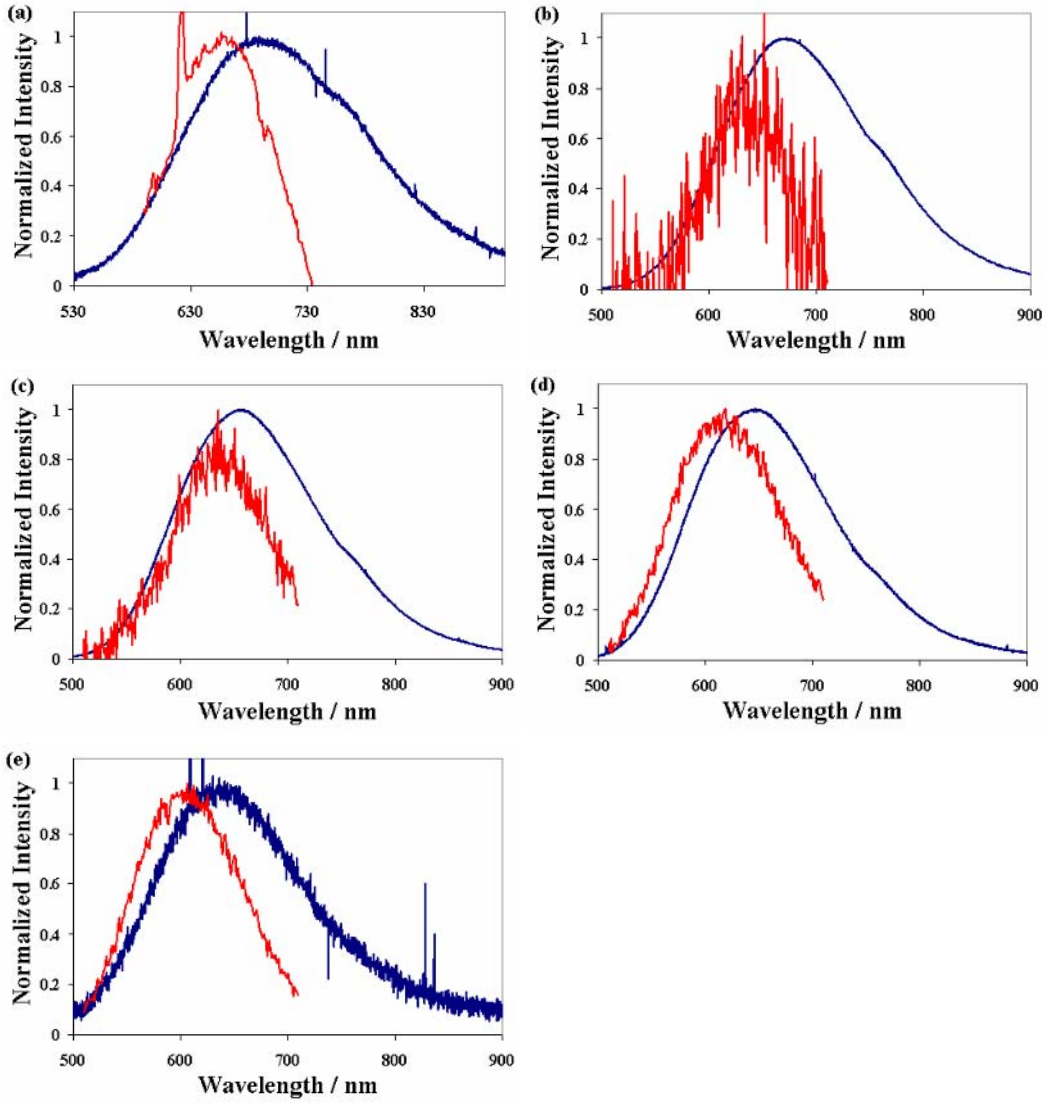

Figure 5.18. PL (red) and ECL (blue) spectra for (dppy)BTPA in (a) 0:1, (b) 1:1, (c) 3:1, (d) 9:1, and (e) 19:1 PhH/MeCN.

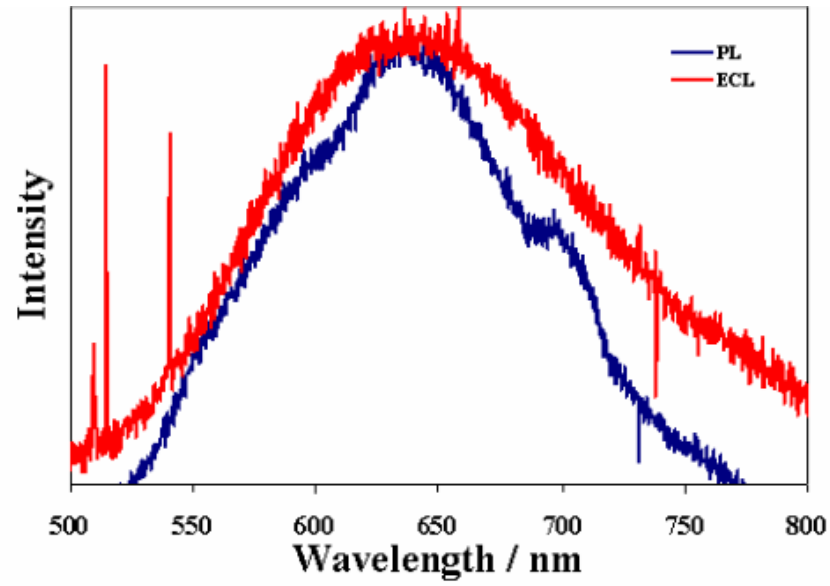

Figure 5.19. ECL and PL of (dppy)BTPA in 19:1 PhH/MeCN with 0.1 M TBAP. Both spectra were obtained on the CCD camera. The PL spectrum was excited using a Hg/Ar pen ray lamp, and the additional peak in the PL spectrum is probably leakage from the source.

produce detectable emission during ECL, even though it was too dilute to detect in the PL spectrum of the electrolyzed solution.

5.4 Conclusions

The strong CT character of (dppy)BTPA leads to a bathochromic shift in PL and ECL, as well as dramatic excited state quenching as the solvent polarizability is increased. While the radical cation of (dppy)BTPA is surprisingly stable, the radical anion dimerizes with $k_f = 1.8\times10^4$ $M^{-1}s^{-1}$. The dimer can either react with impurities to form a species that is oxidizable back to (dppy)BTPA, or at a much slower rate, it can form another product that may be a polymer. The ECL spectrum closely resembles the fluorescence spectrum in each solvent, but has the added feature of a shoulder at long wavelength that may result from an intermediate following the radical anion decomposition.

5.5 References

(1) Li, Y.; Bu, W.; Guo, J.; Wang, Y. *Chem. Commun.* **2000**, 1551.

(2) Yang, G.; Liao, Y.; Su, Z.; Zhang, H.; Wang, Y. *J. Phys. Chem. A*. **2006**, *110*, 8758.

(3) Zhang, H.; Huo, C.; Zhang, J.; Zhang P.; Tian, W.; Wang, Y. *Chem. Commun.* **2006**, 281.

(4) For reviews on ECL, see: (a) *Electrogenerated Chemiluminescence*; Bard, A., Ed.; Marcel Dekker, Inc.: New, York, NY, **2004**. (b) Richter, M. M. *Chem. Rev.* **2004**, *104*, 3003-3036; (c) Knight, A. W.; Greenway, G. M. *Analyst* **1994**, *119*, 879-890; (d) Faulkner, L. R.; Bard, A. J. *Electroanalytical Chemistry*; Marcel Dekker: New York, 1977; Vol. 10, p 1; (e) Bard, A. J.; Debad, J. D.; Leland, J. K.; Sigal, G. B.; Wilbur, J. L.; Wohlstadter, J. N. In *Encyclopedia of Analytical Chemistry: Applications, Theory and Instrumentation*; Meyers, R. A., Ed.; John Wiley & Sons: New York, 2000; Vol. 11, p 9842.

(5) Akins, D. L.; Birke, R. L. *Chem. Phys. Lett.* **1974**, *29*, 428.

(6) Chandross, E.; Sonntag, F. *J. Am. Chem. Soc.* **1966**, *88*, 1089.

(7) Choi, J.-P.; Wong, K.-T.; Chen, Y.-M.; Yu, J.-K.; Chou, P.-T.; Bard, A. *J. Phys. Chem. B*. **2003**, *107*, 14407.

(8) (a) Kapturkiewicz, A.; Grabowski, Z.; Jasny, J. *J. Electroanal. Chem.* **1990**, *279*, 55. (b) Kapturkiewicz, A. *J. Electroanal. Chem.* **1991**, *302*, 131. (c) Kapturkiewicz, A. *Chemical Physics*. **1992**, *166*, 259. (d) Kapturkiewicz, A.; Herbich, J.; Nowacki, J. *Chem. Phys. Lett.* **1997**, *275*, 355.

(9) Kapturkiewicz, A. *Z. Physik. Chem. NF*. **1991**, *170*, 87.

(10) Kapturkiewicz, A. *J. Electroanal. Chem.* **1990**, *290*, 135.

(11) Lackowicz, J. R. *Principles of Fluorescence Spectroscopy*; Plenum Press: New York, 1983; pp 189-208.

(12) Sahami, S.; Weaver, M. *J. Electroanal. Chem.* **1981**, *122*, 155.

(13) (a) Rudolph, M. *J. Electroanal. Chem.* **2003**,*543,* 23; (b) Ruldolph, M. *J. Electroanal. Chem.* **2004**, *571*, 289; (c) Rudolph, M. *J. Electroanal. Chem.* **2003**, *558*, 171. (d) Rudolph, M. *J. Comp. Chem.* **2005**, *26*, 619; (e) Rudolph, M. *J. Comp. Chem.* **2005**, *26*, 633; (f) Rudolph, M. *J. Comp. Chem.* **2005**, *26*, 1193.

(14) Kadish, K.; Ding, J.; Malinski, T. *Anal. Chem.* **1984**, *56*, 1741.

(15) Wallace, W.; Bard, A. *J. Phys. Chem.* **1979**, *83*, 1350.

(16) Ghilane, J.; Hapiot, P.; Bard, A. *Anal. Chem.* **2006**, *78*, 6868.

(17) Eberson, L. In *Organic Electrochemistry*; Baizer, M.; Ed.; Marcel Dekker: New York, NY, **1973**, pp 518-520.

(18) Seo, E.; Nelson, R.; Fritsch, J.; Marcoux, L.; Adams, R. *J. Am. Chem. Soc.* **1966**, *88*, 3498.

(19) Yang, G.; Liao, Y.; Su, S.; Zhang H.; Wang, Y. *J. Phys. Chem. A*. **2006,** *110*, 8758.
(20) Handbook of Chemistry and Physics, 87th Edition, 2006-2007. http://www.hbcpnetbase.com/ (Accessed 10/23/06).
(21) (a) Caspar, J.; Kober, E.; Sullivan, B.; Meyer, T. *J. Am. Chem. Soc.* **1982**, *104*, 630. (b) Englman, R.; Jortner, J. *Molecular Physics*, **1970**, *18*, 145.
(22) (a) Morimoto, A.; Biczók, L.; Yatsuhashi, T.; Shimada, T.; Baba, S.; Tachibana, H.; Tryk, D.; Inoue, H. *J. Phys. Chem. A*. **2002**, *106*, 10089. (b) Willets, K.; Callis, P.; Moerner, W. *J. Phys. Chem. B*. **2004**, *108*, 10465. (c) Anni, M.; Sala, F.; Raganato, M.; Fabiano, E.; Lattante, S.; Cingolani, R.; Gigli, G. *J. Phys. Chem. B*. **2005**, *109*, 6004.
(23) (a) Chapman, C.; Maroncelli, M. *J. Phys. Chem.* **1991**, *95*, 9095. (b) Huppert, D.; Bart, E. *Chem. Phys. Lett.* **1992**, *195*, 37. (c) Lavallee, R.; Zimmt, M. *J. Phys. Chem.* **1994**, *98*, 4254.
(24) Marcus, R. A. *J. Phys. Chem.* **1989**, *93*, 3078.
(25) Fabrizio, E.; Prieto, I.; Bard, A. *J. Am. Chem. Soc.* **2000**, *122*, 4996.

Chapter 6: Electrogenerated chemiluminescence of a BODIPY-based molecule

6.1 Introduction

The electrogenerated chemiluminescence (ECL) spectrum of the modified BODIPY molecule, B^8amide (Figure 6.1a), exhibits a strong, long-wavelength emission that is absent from the photoluminescence (PL). In addition, the ECL transients alternate between high and low intensity when generated by alternating oxidation and reduction potential pulses. Generally, in potential pulse ECL experiments, drastic alternation in the light intensities results from an unstable radical ion, and the light intensity observed on both the forward and reverse pulses rapidly diminishes over the course of a few cycles.[1] The radical ions of B^8amide are highly stable, and the ECL pulses remain visible for at least 20 minutes of potential pulsing. Moreover, B^8amide is structurally similar to the laser dye, PM567 (Figure 6.1b), which gives the expected ECL transients for a molecule with stable radical ions, and does not exhibit any additional, long-wavelength emission.[2] Because of the similarities between PM567 and B^8amide, we made a comparison of their electrochemical and spectroscopic characteristics to try to understand the differences in their ECL.

BODIPY molecules are characterized by high fluorescence quantum efficiency, and they have been studied for their use in biological[3] and light-

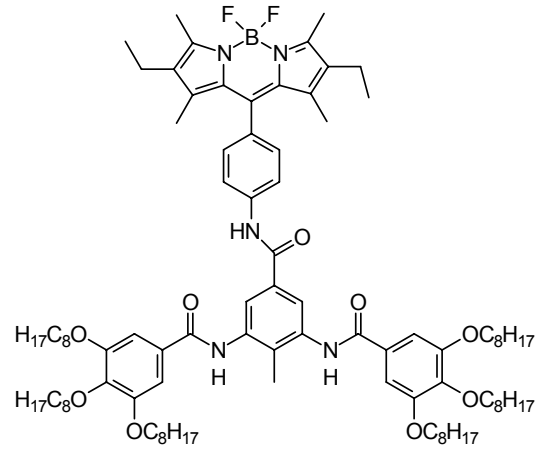

(a)

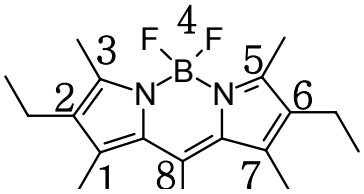

Figure 6.1. Structures of (a) B^8amide (b) PM567.

harvesting[4] applications. The strong absorbance and emission,[5] combined with the ease of tuning the emission wavelength,[6] make BODIPY an ideal molecule for use as a laser dye. Variations of BODIPY have been synthesized with interest in tuning its numerous properties.[7] PM567 is a particularly promising variation,[5b] due to its high fluorescence efficiency (Φ_{PL} = 0.87 in MeCN),[8] and it has since been characterized in many environments to expand its applications.[9] One recent variation is the addition of a large 3,5-diacylamidotoluene group to PM567 to create B[16]amide, which forms a luminescent gel in nonane.[10] The superscript "16" refers to the length of the aliphatic chains attached to the two phenyl rings. The molecule used in this study, B[8]amide, does not form gels,[11] but its greater solubility in high dielectric solvents makes it more convenient for ECL study.

ECL is typically generated through the annihilation of electrochemically generated radical anions and cations. If the enthalpy of annihilation, $-\Delta H_{ann} = -\Delta G - T\Delta S$ ($T\Delta S \approx 0.1$ eV) is greater than the excited state singlet energy, E_S, then the compound is said to be energy sufficient, and the singlet excited state can be directly populated by radical ion annihilation in what is known as S-route ECL.[12] If the compound is not energy sufficient, the annihilation may still produce a triplet state, and the singlet state can be generated via triplet-triplet annihilation. This pathway is called T-route ECL.

$$A + e \rightarrow A^{\bullet -} \quad (6.1)$$

$$A - e \rightarrow A^{\bullet +} \quad (6.2)$$

$$A^{\bullet-} + A^{\bullet+} \rightarrow {}^1A^* \quad (6.3)$$

$$A^{\bullet-} + A^{\bullet+} \rightarrow {}^3A^* \quad (6.4)$$

$${}^3A^* + {}^3A^* \rightarrow {}^1A^* \quad (6.5)$$

$${}^1A^* \rightarrow A + h\nu \quad (6.6)$$

While the above mechanism applies to most ECL systems, a classical exception is the formation of excimers during ECL.[13,14] Especially interesting are relatively planar molecules, such as 9,10-dimethylanthracene, which are too sterically hindered to produce excimers during PL, but readily produce them in ECL.[15] This occurs when the electrostatic attraction between the anion and a cation is sufficient to overcome the steric barrier that prevents excimer formation in PL. Excessive steric hindrance, as seen in 9,10-diphenylanthracene, prevents π-stacking even in ECL, and such molecules are unable to form excimers.[16] Steric hindrance to excimer formation is not always obvious, however, and some molecules that appear too sterically hindered still give excimer emission during ECL.[14,17] Excimer ECL can be identified by generating ECL with a coreactant, such as benzoyl peroxide (BPO), which can be reduced to create a powerful oxidizing agent. Thus a reduction step can create the anion of the molecule and the oxidizing agent in the same step, allowing the formation of the excited state without anion-cation annihilation, as shown below. An excimer peak will therefore not be observed when ECL is generated in the presence of a coreactant.

$$BPO + e \rightarrow BPO^{\bullet-} \quad (6.7)$$

$$BPO^{\bullet-} \rightarrow C_6H_5COO^- + C_6H_5COO^{\bullet} \quad (6.8)$$

$$C_6H_5COO^{\bullet} + A^{\bullet-} \rightarrow A^* + C_6H_5COO^- \quad (6.9)$$

With the basic rules of ECL behavior well-established, systems in which ECL behavior deviates from those expectations are of current interest. While there are many cases of ECL excimers forming despite steric hindrance, to our knowledge, there are no reports in which sterically hindered molecules formed excimers while the mostly planar parent molecules did not. Furthermore, the behavior of ECL transients as a function of time for stable and unstable systems is also well-established. The ECL of B^8amide presents exceptions to both of these generalizations. By studying its electrochemistry and absorbance and fluorescence spectroscopy, we attempt to understand the unusual features of its ECL.

6.2 Experimental

6.2.1 Materials

Anhydrous MeCN (99.93%) was obtained from Aldrich (St. Louis, MO) and transferred directly into a He atmosphere drybox (Vacuum Atmospheres Corp., Hawthorne, CA). Anhydrous benzene was obtained from Aldrich and distilled under vacuum to remove an electroactive impurity before it was transferred into the drybox. Electrochemical grade tetra-*n*-butylammonium hexafluorophosphate ($TBAPF_6$) was obtained from Fluka and used as received. Benzoyl peroxide (BPO) was obtained from Aldrich and used as received. The

modified BODIPY, B^8amide was synthesized according to literature procedure.[10] PM567 was obtained from Exciton, Inc (St. Louis, MO) and used as received.

6.2.2 Characterization

The electrochemical cell consisted of a Pt wire counter electrode (CE), a Ag wire quasi-reference electrode (RE) calibrated using ferrocene as an internal standard (0.342 V vs SCE),[18] and a Pt disk working electrode (WE) inlaid in glass. For cyclic voltammetry, the WE was 1.8 mm in diameter; for ECL experiments, the WE was 2 mm in diameter and bent at a 90˚ angle so the electrode surface faced the detector. In each case, the WE was polished with 0.3 μm alumina, then sonicated in water and ethanol for 1 min each before being rinsed with acetone and transferred into the drybox.

Solutions for electrochemical experiments consisted of 2:1 PhH/MeCN with 0.1 M $TBAPF_6$ and 0.5 mM B^8amide. Electrochemical experiments with PM567 consisted of 1 mM PM567 in pure MeCN with 0.1 M $TBAPF_6$. Solutions for coreactant experiments also contained 10 mM BPO. All solutions were prepared inside of the drybox in glass cells and sealed by a Teflon cap with a rubber O-ring for measurements made outside of the drybox. Stainless steel rods driven through the cap formed the electrode connections. Cyclic voltammograms were recorded on a CH Instruments Model 660 Electrochemical Workstation (Austin, TX).

Due to the high solution resistance, bulk electrolysis was performed in a two-compartment cell. The potential was controlled using an Eco Chemie Autolab PGSTAT100 potentiostat (The Netherlands). For oxidation and reduction, a potential in the diffusion-limited region was applied for 400 s, which was estimated to electrolyze most of the solution while ensuring minimal leakage between compartments. The compartments were separated by a glass frit of fine porosity. Mesh electrodes were used as the WE and CE. The RE was a Pt wire coated with polypyrrol and enclosed in a glass tube separated from the solution by a cracked-glass junction.[19] The WE and RE were placed in the same compartment with 0.8 mM B^8amide and 0.1 M $TBAPF_6$ in 2:1 PhH/MeCN. The CE compartment contained 0.1 M $TBAPF_6$ in MeCN.

Digital simulations of cyclic voltammograms were performed using the DigiElch software package.[20] The uncompensated resistance (1.5 kΩ) and double-layer capacitance (120 nF) were determined from the current response to a potential step made in a non-faradaic region. The diffusion coefficients, D, of B^8amide (2.3×10^{-6} cm^2/s) and PM567 (6.6×10^{-6} cm^2/s) were determined from a Cottrell plot of an oxidizing potential step applied for 1 s. All products of the electrochemical processes were assigned the same D as the parent. The electrode surface area was determined from a Cottrell plot of a potential step experiment in 1 mM ferrocene in MeCN ($D = 1.2 \times 10^{-5}$ cm^2/s).[21]

For spectroscopy experiments, B^8amide and PM567 solutions were prepared in a 1 cm quartz cell. Absorbance spectra were collected on a DU 640 spectrophotometer (Beckman, Fullerton, CA). Fluorescence spectra were collected on a QuantaMaster Spectrofluorimeter (Photon Technology International, Birmingham, NJ). The excitation source was a 70W xenon lamp, and the excitation and emission slits were set to 0.5 mm.

ECL was generated by pulsing the electrode potential 80 mV beyond the diffusion-limited peak potentials, E_p, for oxidation and reduction of the analyte at 5 Hz. For samples containing BPO, the potential was pulsed between 0 V and $E_{p,red}$ – 80 mV. Spectra were collected on a Princeton Instruments Spec-10 CCD Camera (Trenton, NJ) with an Acton SpectraPro-150 monochromator (Acton, MA). ECL spectra were calibrated using a Hg/Ar pen-ray lamp from Oriel (Stratford, CT). ECL transients were collected using a photomultiplier tube (PMT, Hamamatsu R4220p, Japan) supplied with -750 V from a Kepco (New York) high voltage power supply and recorded, along with the electrochemical data, on the Autolab potentiostat.

Molecular modeling calculations were performed using Hyperchem 5 (Hypercube, Inc., Gainesville, FL). The initial geometry for PM567 was chosen as planar, with the ethyl substituents facing downwards. MM+ followed by AM1 geometry optimizations using the Fletcher-Reeves conjugate gradient algorithm were used to find the conformation of the neutral molecule. The radical ion

geometries were optimized by the same method, using the neutral geometry as the starting geometry.

6.3 Results and Discussion

6.3.1 Electrochemistry.

The electrochemistry of B[8]amide was studied by CV and compared to that of PM567. The reversibility of the CVs of both molecules at scan rates as low as 50 mV/s demonstrates high stability of the radical ions. A CV of both redox processes of B[8]amide is presented in Figure 6.2. As summarized in Table 6.1, the reduction potential, E^{o}_{red}, of B[8]amide is -1.40 V vs SCE, and the oxidation potential, E^{o}_{ox}, is 0.96 V vs SCE, as estimated from a point half-way between the forward and reverse peak potentials. For PM567, E^{o}_{red} = -1.37, and E^{o}_{ox} = 0.94 V vs SCE.[2,22] The 30 mV differences between the two compounds may result from the higher resistance of the solvent used for B[8]amide. For both compounds, the anodic peak current becomes larger than the cathodic peak current at high scan rates. Digital simulations of the CVs performed at scan rates from 50 mV/s to 10 V/s show that the oxidation simulation can fit the experimental data using only the experimentally determined data and a heterogeneous electron transfer (HET) rate constant, k^{o}, of 10^{4} cm/s, as shown in Figure 6.3. The rate constant in this case is an arbitrarily large number chosen to ensure reversibility. Fitting the reduction CVs, however, requires k^{o} = 0.01 cm/s (Figure 6.4).

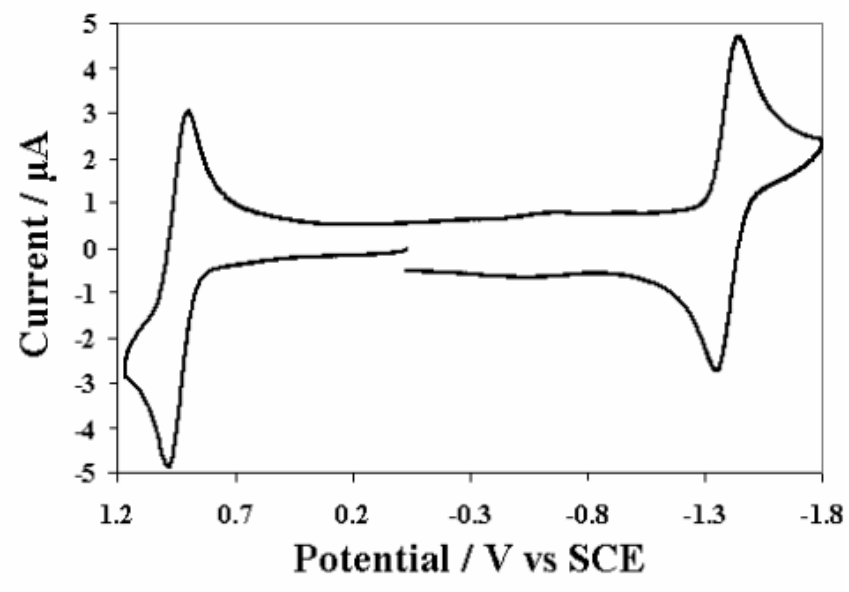

Figure 6.2. Cyclic voltammogram of 0.5 mM B^8amide in 2:1 PhH/MeCN with 0.1 M $TBAPF_6$. Scan rate was 200 mV/s.

Table 6.1. Electrochemical, spectroscopic, and ECL data for PM567 and B^8amide.

	$E_{1/2}$ / V vs SCE		$\lambda_{max,abs}$	ε_{max}
	$A/A^{\bullet-}$	$A/A^{\bullet+}$	(nm)	($M^{-1}cm^{-1}$)
B^8amide	-1.40	0.96	526	7.0×10^4
PM567	-1.37	0.94	516	7.9×10^4

	$\lambda_{max,PL}$ (nm)	Φ_{PL}	E_s (eV)	E_{ann} (eV)	λ_{ECL} (nm)	Φ_{ECL}
B^8amide	537	0.84	2.33	2.26	551, 741	0.006
PM567	533	0.87	2.37	2.37	555	0.009

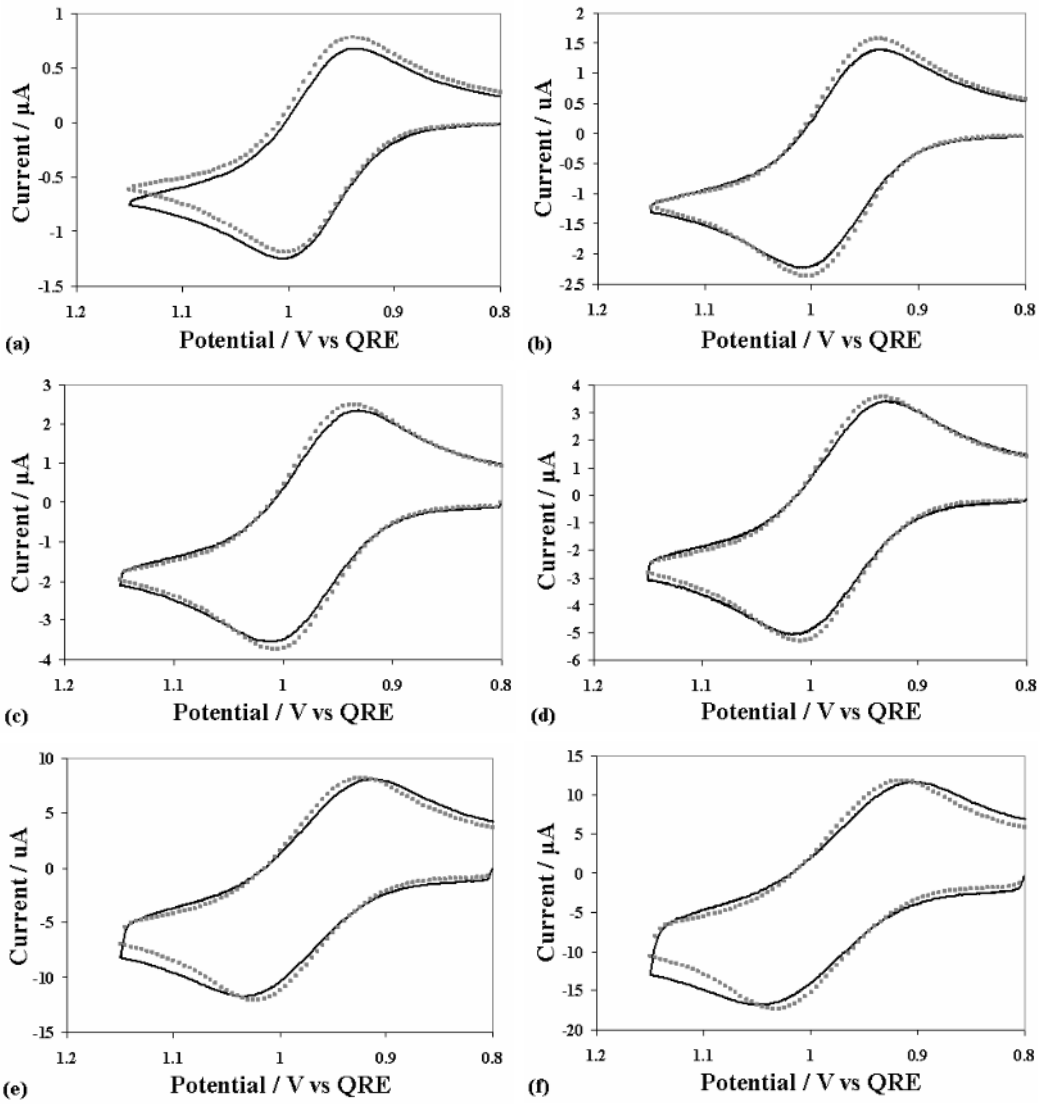

Figure 6.3. Simulated (gray squares) and experimental (black lines) cyclic voltammograms for 0.49 mM B[8]amide in 2:1 PhH/MeCN with 0.1 M $TBAPF_6$ at scan rates (a) 0.05 (b) 0.2 (c) 0.5 (d) 1 (e) 5 (f) 10 V/s. The simulation parameters are $D = 2.3\times10^{-6}$ cm^2/s, $k^o = 10^4$ cm/s (arbitrarily chosen to ensure diffusion control), $R_u = 1.6$ kΩ, $C_d = 120$ nF.

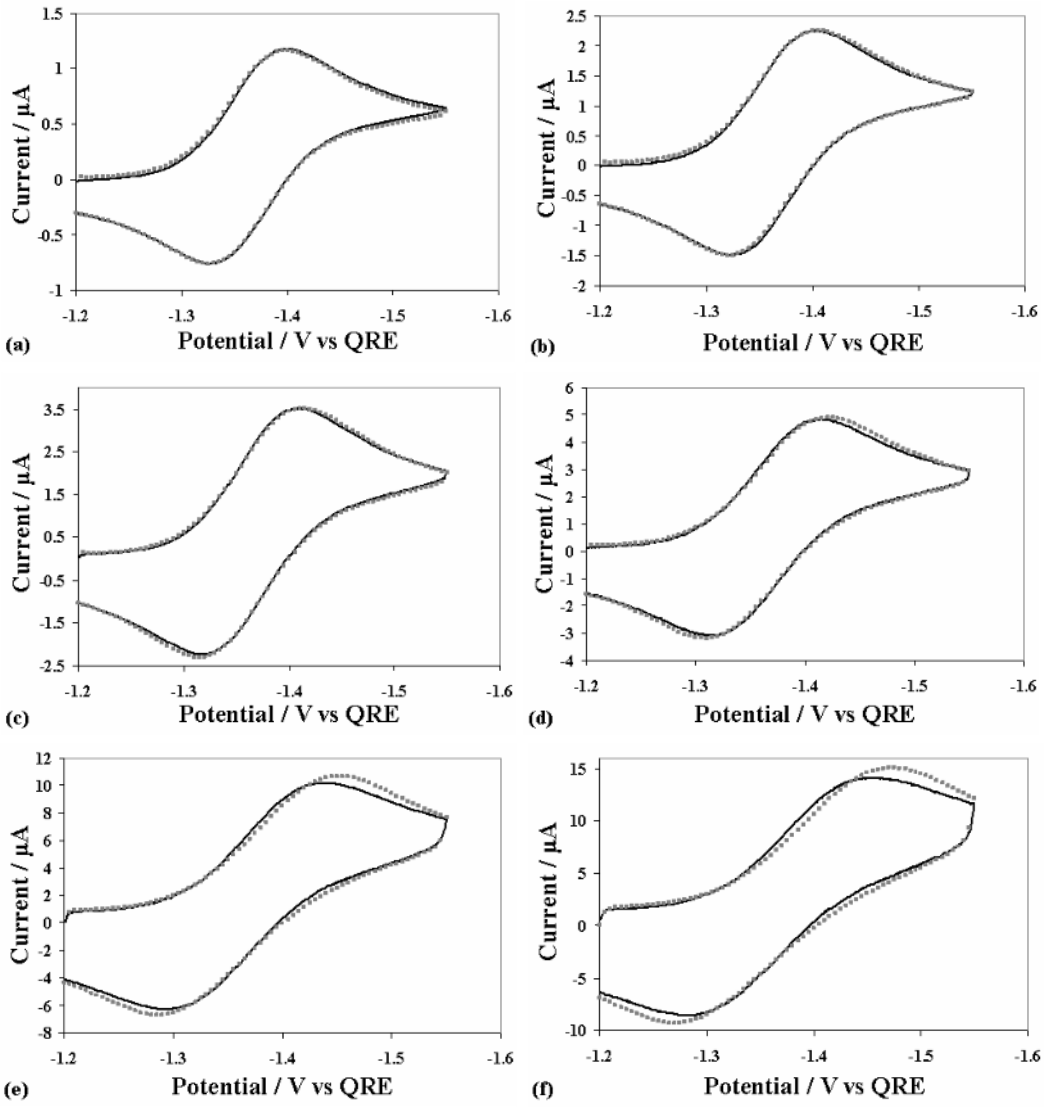

Figure 6.4. Simulated (gray squares) and experimental (black lines) cyclic voltammograms for 0.49 mM B[8]amide in 2:1 PhH/MeCN with 0.1 M $TBAPF_6$ at scan rates (a) 0.05 (b) 0.2 (c) 0.5 (d) 1 (e) 5 (f) 10 V/s. The simulation parameters are $D = 2.3\times10^{-6}$ cm^2/s, $k^o = 0.01$ cm/s, $R_u = 1.6$ kΩ, $C_d = 120$ nF.

Since PM567 reduction also requires a small k^o, the additional reorganizational energy responsible for the slow kinetics of B^8amide must come from the BODIPY moiety, rather than the 3,5-diacylamidotoluene substituent. The poor solvation of organic molecules minimizes the affect of solvent reorganization on electron transfer kinetics,[23] so a conformational change in the molecule is the more likely cause. To investigate this possibility, AM1 geometry optimizations were performed on PM567 and its radical ions. Figure 6.5a depicts an end-on view of the molecule, in which the boron is in front. From this perspective, the structural changes can be change in the position of the boron relative to the rest of the molecule. The torsion angle between the boron and the carbon at position 8 is 6˚ for the neutral dye, 2˚ for the cation (Figure 6.5b), and 27˚ for the anion (Figure 6.5c). As shown in Figure 5c, the boron of the anion is shifted above the plane of the molecule. We attribute the slower HET kinetics of the reduction to the greater internal reorganization energy required to form the anion.

Bulk reduction of B^8amide (Figure 6.6a) produced a dark purple solution that reverted to its original color upon exposure to oxygen, indicating that the bulk electrolysis produced stable radical anions that were oxidized in air. Bulk oxidation initially resulted in a red solution, but overnight, the solution turned slightly green. The green solution did not revert to its original color when exposed to oxygen, indicating that the radical cation slowly decomposed to a

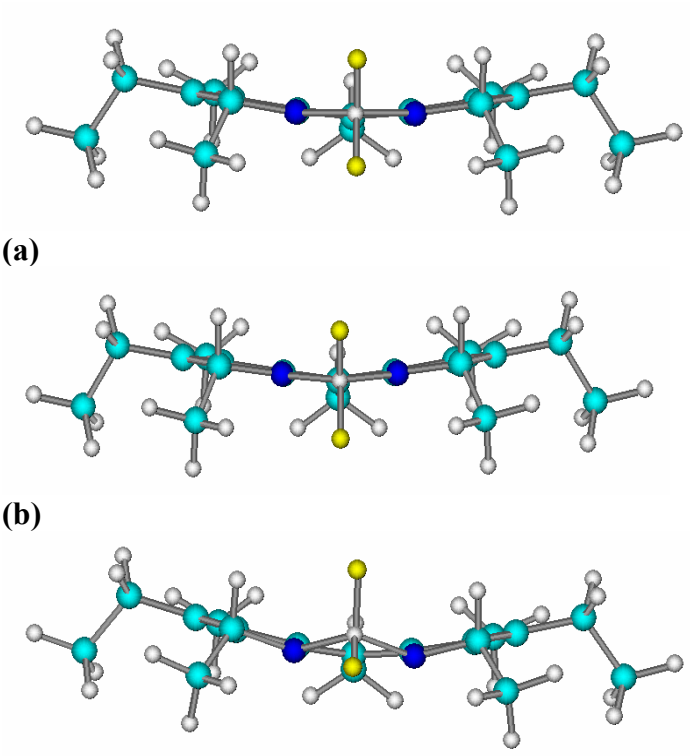

Figure 6.5. End-on view of AM1 geometries of (a) neutral PM567 (b) PM567 cation (c) PM567 anion. Boron (gray) is in the middle, flanked by two nitrogens (dark blue). The fluorines attached to boron are yellow. Hydrogens (also gray) are shown attached to each carbon.

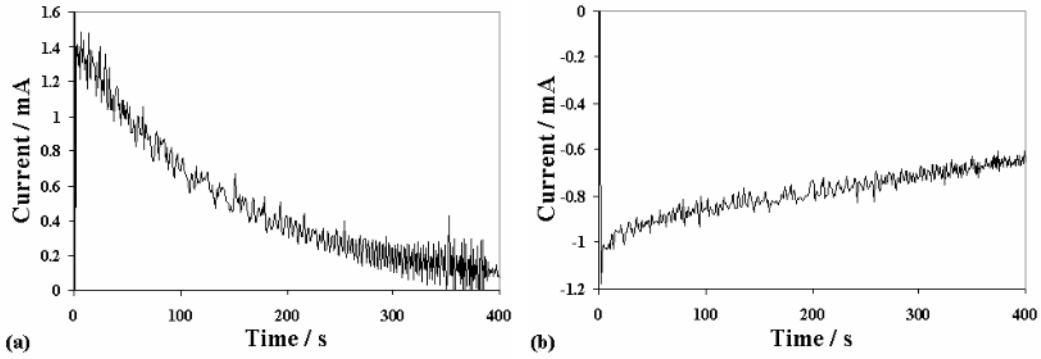

Figure 6.6. Bulk (a) reduction (0.196 C) and (b) oxidation (0.319 C) of 0.8 mM B^8 amide in 2:1 PhH/MeCN. 0.232 C required for total electrolysis in either direction.

stable product. In addition, the *i-t* curve describing the bulk oxidation did not decay to background as rapidly as expected (Figure 6.6b), and the charge passed during this process was 0.319 C, which is greater than the 0.232 C expected for total electrolysis of the solution. This could indicate a catalytic process, in which the oxidized species is reduced by something else in the solution and is then reoxidized at the electrode, thus generating more than the expected current. However, since a two compartment cell was used, the apparent catalytic behavior could also be due to diffusion of material from the counter electrode compartment into the working electrode compartment. The same electrolysis curve was observed from PM567 oxidation, though the color change to green occurred during the electrolysis, rather than after. The difference in color change rates is likely because the greater steric hindrance of B^8amide inhibits secondary reactions. Oxidative polymerization has been observed for less-substituted BODIPY molecules,[2] and the product was believed to be analogous to polypyrrole.[6]

Chemical ionization mass spectra (MS) of the parent compounds and their oxidation products were obtained to determine if polymerization occurred. A mass spectrum of the PM567 oxidation product yielded a peak around m/z = 630, which is approximately twice the molecular weight of PM567 (318 g/mol), while the MS of pure PM567 gave only the peaks near 318. Thus a dimer, and possibly a polymer, was created upon bulk oxidation of PM567. However, the MS of pure B^8amide and its oxidation product both exhibited peaks around m/z = 3041—

approximately twice the molecular weight of pure B^8amide (1521 g/mol). The presence of the 3041 peak in both compounds indicates that a dimer of B^8amide is created in the MS, so its creation by electrolysis cannot be verified in this way.

6.3.2 Spectroscopy.

The absorbance and PL of B^8amide and PM567 (Figure 6.7) were obtained to better understand the ECL. The absorbance spectrum of B^8amide has a λ_{max} at 526 nm, compared with 516 nm for PM567, and an extinction coefficient, ε, of 70,000 $M^{-1}cm^{-1}$, compared with 79,000 $M^{-1}cm^{-1}$ for PM567. The PL spectrum features a single, intense peak that is a mirror image of the absorbance spectrum, with a λ_{max} at 537 nm (533 nm for PM567) and a Φ_{PL} of 0.84, determined with respect to PM567 (Φ_{PL} = 0.87[8]). The longer wavelength absorbance and PL of B^8amide suggest partial conjugation between the BODIPY moiety and the attached phenyl group. The Stokes shift of PM567 is greater than that of B^8amide, which implies slightly more solvent relaxation around the excited state of the smaller molecule. This is attributed to shielding of the chromophore by the large substituents of B^8amide. The spectroscopic characteristics of B^8amide in 2:1 PhH/MeCN are similar to those observed in CH_2Cl_2, with the exception of the quantum efficiency, which is higher than the reported value of 0.62.[11]

The absorbance and fluorescence spectra of the B^8amide and PM567 oxidation products were obtained to determine whether or not the products produced the anomalous, 741 nm ECL. The absorbance spectra of the products

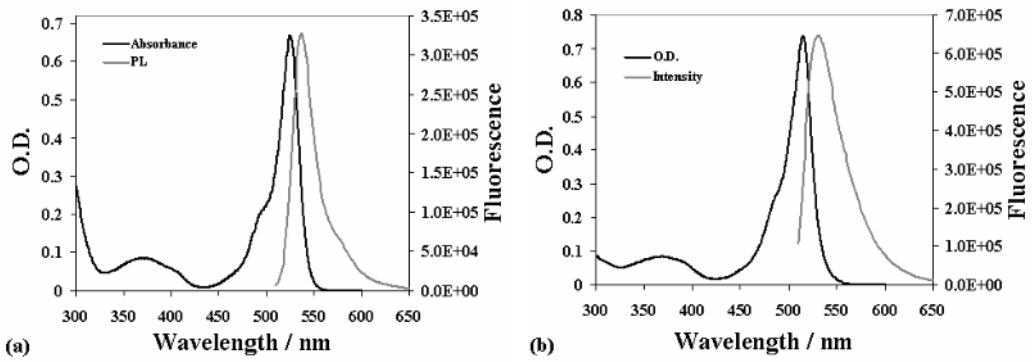

Figure 6.7. Absorbance and fluorescence spectra of (a) 9.5 μM (absorbance) and 0.95 μM (PL) B^8amide in 2:1 PhH/MeCN and (b) 9.4 μM (absorbance) and 0.61 μM (PL) of PM567 in MeCN.

differed from the parent compounds only by the addition of a new peak at 545 nm for PM567, (Figure 6.8a) and new peaks at 560 and 588 nm (Figure 6.8b) for B^8amide. Excitation spectra of the products were obtained with the detector monitoring 741 nm, but none of the observed emissions were significantly above background, suggesting that the extra ECL peak is not emission from the product. Furthermore, if the ECL emission at 741 nm results from a product formed during ECL, it should affect the ECL of PM567 even more noticeably than it affects the ECL of B^8amide, since PM567 is less sterically inhibited from product formation. As discussed in the next section, the ECL spectrum of PM567 does not exhibit a 741 nm peak.

6.3.3 Electrogenerated Chemiluminescence (ECL).

The ECL spectrum of B^8amide has a λ_{max} at 551 nm, which is comparable to that observed in the PL (Figure 6.9). The 14 nm red shift of the ECL spectrum from the PL is attributed to the inner filter effect due to the high concentration of B^8amide used for the ECL solution. The PM567 ECL λ_{max} appears at longer wavelength than B^8amide, despite having a shorter PL λ_{max} and a larger Stokes shift. This is likely because PM567 solutions were more concentrated than B^8amide solutions, thus enhancing the inner filter effect. As shown in Table 6.1, Φ_{ECL} for PM567 (0.009) and B^8amide (0.006) are approximately equal, given the large uncertainty of ECL efficiency measurements. E_s was estimated from $hc(\bar{\nu}_a + \bar{\nu}_f)/2$,[24] assuming $T\Delta S \approx 0$ for the electronic excitation. The data indicate that

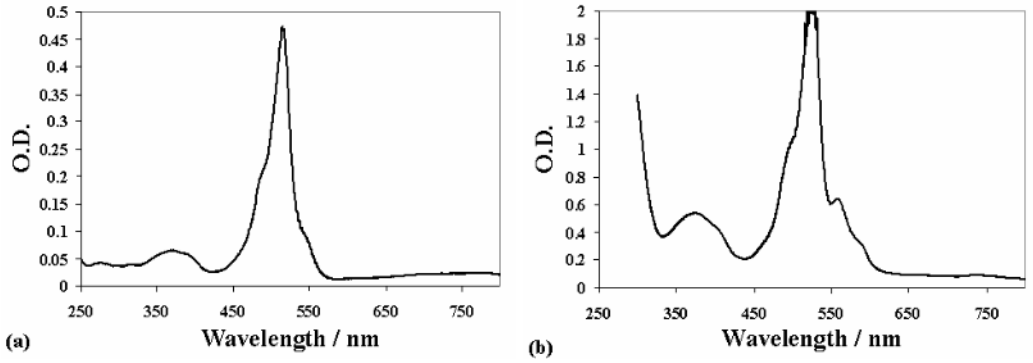

Figure 6.8. Absorbance spectra of (a) 10 μM PM567 and (b) 37 μM B^8amide.

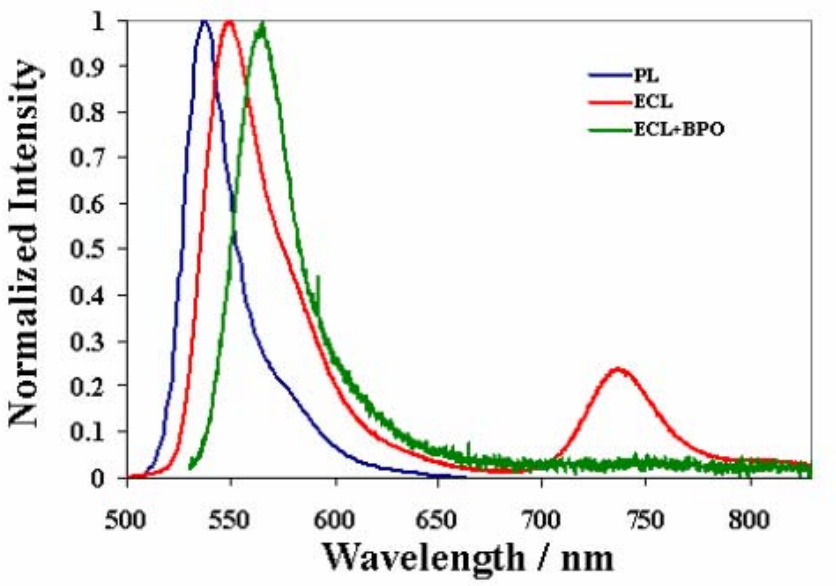

Figure 6.9. B^8amide in 2:1 PhH/MeCN PL spectrum (blue line, 1 μM), ECL spectrum (red line, 0.5 mM), and ECL spectrum generated with the coreactant, BPO (green line, 0.5 mM B^8amide, 10 mM BPO). ECL spectra were integrated 5 min using a 1 mm slit width.

the annihilation is not energy sufficient either compound, so the emission must occur through T-route ECL.

Unlike PM567, the ECL of B^8amide features an additional peak at 741 nm, which has a shoulder extending to even longer wavelengths. When B^8amide ECL is generated using the coreactant, BPO, only the first peak is visible, though for unknown reasons, it appears at 566 nm, rather than 551. The disappearance of the long wavelength peak when a coreactant is used suggests that the emission originates from excimers, but it remains unclear why a compound as sterically hindered as B^8amide would form excimers, while the more planar PM567 does not.

The tendency of some B^namide molecules to aggregate in certain solutions[10] led us to examine the concentration dependence of the relative ECL of the two peaks to see if aggregation played a role in the 741 nm peak. A series of experiments was run using 0.02 mM, 0.1 mM, and 0.5 mM B^8amide. In each case, the ECL spectrum was obtained after five minutes of integration, and the ratio of the peak intensties, I_{741}/I_{551}, is plotted in Figure 6.10. This was repeated several times at each concentration, since the relative intensities varied with each integration. The solution was shaken between integrations to ensure that the starting conditions remained the same for each experiment. The data is plotted against the total integration time after each interval. For the 0.02 mM and 0.5 mM sets, the intensity ratio increases with each successive integration until about

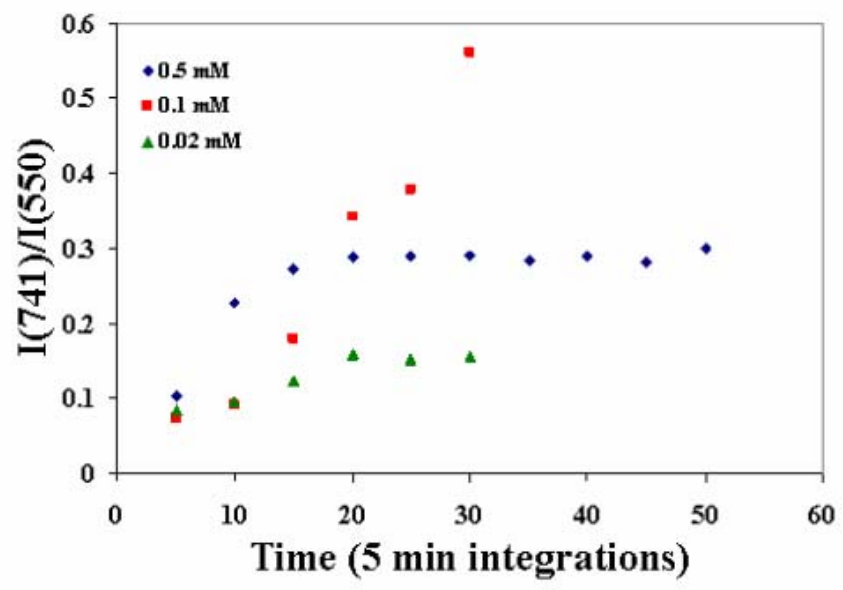

Figure 6.10. Ratio of the 741 and 550 nm peak intensities observed in the ECL spectrum plotted as a function of integration time for 0.5 mM (blue), 0.1 mM (red), and 0.02 mM (green).

20 minutes, at which point the same relative intensity is obtained every time. Based on the data for 0.02 mM and 0.5 mM, there is an overall greater relative 741 nm emission present for higher concentrations of B^8amide, suggesting that an excimer or aggregate is responsible for the long-wavelength peak.

However, interpretation of the data is complicated by the 0.1 mM sample, which deviated dramatically from the expected trend. The relative ECL intensity of this sample continues to increase for each measurement obtained. We cannot propose a mechanism that explains this deviation. In light of this data, and various, isolated experiments, in which the peak intensity ratio was almost unity, we assume that some variables of this experiment are still not under control, despite the consistency of the 0.02 and 0.5 mM data.

All three data sets are consistent in that the ECL intensity ratio increases with pulsing time. If the 741 nm emitter is a solution phase aggregate or product, any variation in relative intensity should have been only due to experimental uncertainty. The gradual increase in relative intensity with each experiment suggests the formation of a film on the electrode, since that would continue to thicken with time, regardless of any shaking of the solution. If the long-wavelength ECL originates from a film on the electrode, then an ECL transient should still be generated if a film-coated electrode is then transferred to a solution with no analyte. However, this experiment did not give the expected light pulse.

Part of the difficulty in detecting ECL from the proposed film on the electrode may be seen in the asymmetry of the ECL transients (Figure 6.11). After oxidation, very little light appears on reduction. However, after reduction, a large pulse of light appears on oxidation. This emission is 30 times the intensity of the next reduction pulse, but the emission is very stable with continued pulsing. Eventually, the oxidation pulse light intensity grows, which is usually attributed to the removal of impurities from the electrode surface. The reduction pulse, meanwhile, slowly decreases in intensity, which is often due to unstable radical ions. However, the cyclic voltammetry and bulk electrolysis demonstrate that both radical ions are stable on the time scale of the experiment. Furthermore, the light intensity remains visible for at least 20 min, which is far longer than would be expected from a molecule with such unstable radical ions. Another inconsistency is the normal ECL transient behavior of PM567, which exhibits no alternation in pulse intensity, despite its more rapid oxidative polymerization.

After about 20 min of continuous cycling, the oxidation light intensity of B^8amide has decreased below the intensity of the reduction pulse (Figure 6.12a), and both pulses are stable. If the experiment is stopped and restarted, the new reduction pulses again have lower intensities than the oxidation pulses. However, their intensity relative to the oxidation pulses is much greater than in the initial series of pulses. This agrees with the spectral ECL data, which shows that some product of the long term pulsing was retained by the electrode even after stopping

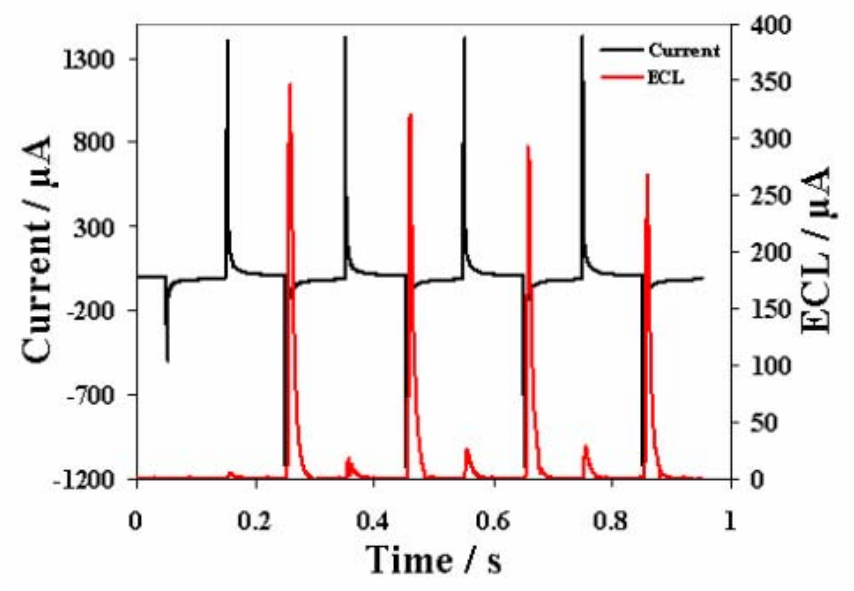

Figure 6.11. Current (black) and ECL (red) transients for 0.5 mM B^{8}amide in 2:1 PhH/MeCN pulsed between oxidation and reduction at 5 Hz.

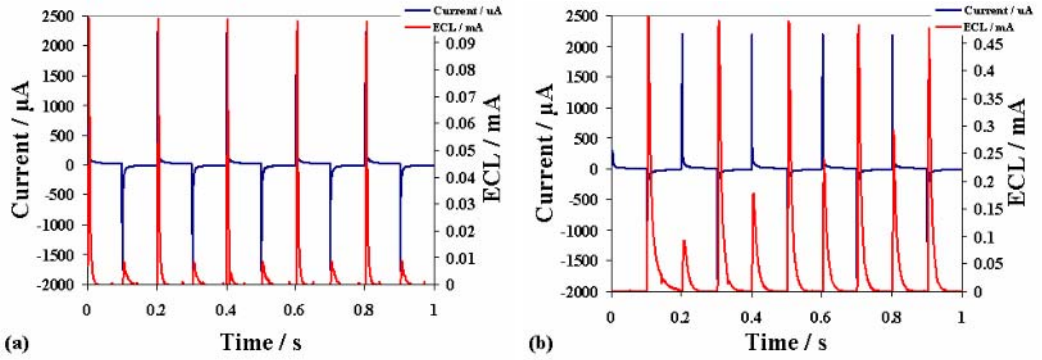

Figure 6.12. ECL transients of (a) the last second of a continuous 20 min pulsing experiment and (b) the first 1 s pulsing experiment performed after the 20 min pulsing experiment. Pulse width = 0.1s.

the experiment. It suggests that the proposed film must be oxidized or reduced before it can interact with an oxidized species in solution. One possible explanation for the alternating light intensities is that the radical cation is a stronger quencher than the anion. However, we were unable to obtain a PL spectrum of the radical cation solution prior to its decomposition, and the decomposition product did not demonstrate significant quenching.

The alternating intensity of the ECL pulses may be responsible for the absence of light during the experiments to determine whether or not a film on the electrode accounted for the 741 nm emission. If the weak (reduction) pulse is the one that originates from a film on the electrode, then light from the reduction pulses must primarily occur at 741 nm. However, the use of a longpass filter to screen all but the long-wavelength light reduced the intensity of both emissions almost equally, suggesting that each potential pulse generates light at both wavelengths.

6.4 Conclusions

We have observed two unique ECL phenomena from B^8amide. The first is the presence of a second strong peak at 741 nm that we cannot explain. The B^8amide cation slowly decomposes to a product, but that product does not appear to emit in the region of interest. Furthermore, PM567 undergoes the same decomposition even more rapidly than B^8amide, and it does not exhibit the second ECL peak. The growth of the second peak with continued potential cycling

suggests that the long-wavelength ECL involves film formation on the electrode. The second phenomenon of interest is the stability of ECL transients that alternate in intensity. During continuous pulsing, very little light is observed from the reduction, initially, while a large pulse of light accompanies the oxidation. Despite this dramatic asymmetry, the ECL is still visible after 20 minutes of pulsing. More experiments should be done to understand this intriguing behavior.

6.5 References

(1) Cruser, S.; Bard, A. *J. Am. Chem. Soc.* **1969**, *91*, 1969.
(2) Lai, R.; Bard, A. *J. Phys. Chem. B.* **2005**, *107*, 5036.
(3) Karolin, J.; Johansson, L.; Strandberg, L.; Ny, T. *J. Am. Chem. Soc.* **1994**, *116*, 7801.
(4) Wagner, R.; Lindsey, J. *Pure Appl. Chem.* **1996**, *68*, 1373.
(5) (a) Guggenheimer, S.; Boyer, J.; Thangaraj, K.; Shah, M.; Soong, M.; Pavlopoulos, T. *Applied Optics.* **1993**, *32*, 3942. (b) O'Neil, M. *Optics Letters*. **1993**, *18*, 37.
(6) Burghart, A.; Kin, H.; Welch, M.; Thoresen, L.; Reibenspies, J.; Burgess, K. *J. Org. Chem.* **1999**, *64*, 7813.
(7) Ziessel, R.; Ulrich, G.; Harriman, A. *New J. Chem.* **2007**, *31*, 496.
(8) Arbeloa, T.; Arbeloa, F.; Arbeloa, I.; García-Moreno, I.; Costela, A.; Sastre, R.; Amat-Guerri, F. *Chem. Phys. Lett.* **1999**, *299*, 315.
(9) Arbeloa, F.; Arbeloa, T.; Arbeloa, I.; García-Moreno, I.; Costela, A.; Sastre, R.; Amat-Guerri, F. *Chem. Phys.* **1998**, *236*, 331.
(10) Camerel, F.; Bonardi, L.; Schmutz, M.; Ziessel, R. *J. Am. Chem. Soc.* **2006**, *128*, 4548.
(11) Camerel, F.; Bonardi, L.; Ulrich, G.; Charbonnière, L.; Donnio, B.; Bourgogne, C.; Gillon, D.; Retailleau, P.; Ziessel, R. *Chem. Mater.* **2006**, *18*, 5009.
(12) For reviews on ECL, see: (a) *Electrogenerated Chemiluminescence*; Bard, A., Ed.; Marcel Dekker, Inc.: New, York, NY, **2004**. (b) Richter, M. M. *Chem. Rev.* **2004**, *104*, 3003-3036; (c) Knight, A. W.; Greenway, G. M. *Analyst* **1994**, *119*, 879-890; (d) Faulkner, L. R.; Bard, A. J. *Electroanalytical Chemistry*; Marcel Dekker: New York, 1977; Vol. 10, p 1; (e) Bard, A. J.; Debad, J. D.; Leland, J. K.; Sigal, G. B.; Wilbur, J. L.; Wohlstadter, J. N. In *Encyclopedia of Analytical Chemistry: Applications, Theory and Instrumentation*; Meyers, R. A., Ed.; John Wiley & Sons: New York, 2000; Vol. 11, p 9842.
(13) (a) Werner, T.; Chang, J.; Hercules, D. *J. Am. Chem. Soc.* **1970**, *92*, 763. (b) Werner, T.; Chang, J.; Hercules, D. *J. Am. Chem. Soc.* **1970**, *92*, 5560.
(14) Choi, J.-P.; Wong, K.-T.; Chen, Y.-M.; Yu, J.-K.; Chou, P.-T.; Bard, A. *J. Phys. Chem. B* **2003**, *107*, 14407.
(15) Werner, T.; Chang, J.; Hercules, D. *J. Am. Chem. Soc.* **1970**, *92*, 763.
(16) Chandross, E.; Longworth, J.; Visco, R. *J. Am. Chem. Soc.* **1965**, *87*, 3259.
(17) (a) Prieto, I.; Teetsov, J.; Fox, M.; Vanden Bout, D.; Bard, A. *J. Phys. Chem. A*, **2001**, *105*, 520. (b) Fungo, F.; Wong, K.-T.; Ku, S.-Y.; Hung, Y.-Y.; Bard, A. *J. Phys. Chem. B*, **2005**, *109*, 3984. (c) Sartin, M.; Shen, W.-J.; Dodda, R.;

Wu, C.-C.; Wu, F.-I.; Liu, T.-H.; Chen, H.-H.; Chen, C.; Shu, C.-F.; Bard, A. **Manuscript in preparation**.
(18) Sahami, S.; Weaver, M. *J. Electroanal. Chem.* **1981**, *122*, 155.
(19) Ghilane, J.; Hapiot, P.; Bard, A. *Anal. Chem.* **2006**, *78*, 6868.
(20) (a) Rudolf, M. *J. Electroanal. Chem.* **2003**,*543,* 23; (b) Ruldolf, M. *J. Electroanal. Chem.* **2004**, *571*, 289; (c) Rudolf, M. *J. Electroanal. Chem.* **2003**, *558*, 171. (d) Rudolf, M. *J. Comp. Chem.* **2005**, *26*, 619; (e) Rudolf, M. *J. Comp. Chem.* **2005**, *26*, 633; (f) Rudolf, M. *J. Comp. Chem.* **2005**, *26*, 1193.
(21) Kadish, K.; Ding, J.; Malinski, T. *Anal. Chem.* **1984**, *56*, 1741.
(22) The actual values used in reference (2) have been adjusted here, because the authors of reference (2) chose ferrocene as 0.424 V vs SCE, whereas we used 0.342 V vs SCE.
(23) Cauquis, G. In *Organic Electrochemistry*; Baizer, M.; Ed.; Marcel Dekker: New York, NY, **1973**, pp 33-35.
(24) Marcus, R. A. *J. Phys. Chem.* **1989**, *93*, 3078.

Chapter 7: Concluding Remarks

The ECL of a series of silole-based chromophores was examined to understand the effects of steric hindrance on the PL, electrochemistry, and ECL of these molecules. For the ethylene substituted siloles, increasing the number of phenyl substituents on the chromophore decreased the radical ion stability and the Φ_{PL}, hence lowering the ECL emission. Because the double-bonded substituent introduces a bend between the silole moiety and the phenyl, a rotation in the substituent moves the phenyl out of the plane of conjugation with the silole moiety. Adding phenyls to the double bond forced the substituent to rotate in order to alleviate steric crowding. However, doing so exposes the double bonds to secondary reactions following oxidation. For the ethynyl-substituted siloles, the conjugation path from the silole moiety to the phenyl group is linear, and conjugation remains no matter how the phenyls rotate to alleviate steric stress. As a result, increasing steric crowding caused the phenyls to rotate in a way that protected the triple bonds from secondary reactions. Additionally, with enough steric crowding, the molecule became rigid, which reduced internal conversion.

Spiro-FPA consists of two DPA redox centers linked by a spirobifluorene moiety. Since these are uncoupled centers, both reductions occur at the same potential, as do both oxidations. As a result, all spiro-FPA electrochemistry results in the creation of di-ions. The electrostatic attraction between di-ions is

much greater than that between mono-ions, which allows spiro-FPA to form excimers where equally sterically hindered DPA does not. Because the spiro-FPA excimer formed during annihilation is not quenched by electron transfer from the other chromophore, the presence of excimer emission provides evidence for a simultaneous two-electron transfer.

The boron-containing molecule, (dppy)BTPA, shows solvatochromic trends, both in emission wavelength and intensity. A Lippert plot of peak emission wavelengths gave good agreement with the expected trend for various mixtures of acetonitrile and benzene. When a variety of solvents were used, however, some data points at low polarizabilities gave large deviations from the rest, and the dipole moments are different from the values obtained for the ECL plots. In addition to the wavelength peak, high polarizability solvents and the addition of electrolyte strongly quench the emission relative to what is observed in pure benzene.

The ECL of B^8amide shows several interesting phenomena that are not yet understood. The ECL spectrum has an intense, long-wavelength emission. The emission is absent if the ECL spectrum is generated with the aid of a coreactant, which would suggest excimer formation, but the molecule is sterically very bulky. Moreover, PM567, a similar, less sterically hindered molecule, does not exhibit any new peaks during ECL. The growth of this peak as a function of potential pulsing time suggests that it is generated by film formation, but we were unable to

verify this theory. An additional unusual phenomenon is seen in the ECL transients for a potential pulse experiment. The ECL pulse observed on oxidation is approximately 30 times higher than that observed on reduction. Alternating high and low intensities with each pulse typically indicates an unstable radical ion, but the radical ions of B^8amide appear stable on the time scale of the experiment. In addition, simulations of ECL transients for systems with unstable radical ions predict a rapid decay of the total ECL with time. However, the ECL transients in B^8amide recover completely after each weak pulse, and light is still clearly visible after at least 20 min.

Appendix A Simulation Parameters

In this section is a complete list of the parameters used to construct the ECL simulations presented in Chapter 2. The parameters and values here are given exactly as they appear in the Multiphysics program and are intended for use in reproducing the results. A more detailed discussion of the methods used is presented in Chapter 2.

Application mode type: Diffusion (Chemical Engineering Module)

Application mode name: chdi

Mesh Statistics.
Number of degrees of freedom: 525
Number of mesh points: 53
Number of elements: 52
Number of boundary elements: 2
Element length ratio: 0

Application mode properties.
Default element type: Lagrange—Quadratic
Analysis type: Transient
Equilibrium assumption: Off
Frame: Frame (ref)
Weak constraints: Off

Dependent variables: cN (neutral concentration), cA (anion concentration), cC (cation concentration), cE (excited state concentration), cF (decomposition product concentration)

Shape functions: shlag(2,'cN'), shlag(2,'cA'), shlag(2,'cC'), shlag(2,'cE'), shlag(2,'cF')

Interior boundaries not active

Table A.1. Constants used in simulations.

Name	Value	Description
alpha	0.5	electron transfer coefficient
FAR	96485 C/mol	Faraday's const.
R	8.314 J/mol*K	Gas constant
T	298.15 K	Temperature
f	38.92 V^{-1}	F/RT
E0A	-0.8 V	$E^o(A/A^{\bullet -})$[1]
E0C	0.8 V	$E^o(A/A^{\bullet +})$[1]
D	10^{-5} cm^2/s	diffusion coefficient
kann	2×10^8 $M^{-1}s^{-1}$	annihilation rate const.
kem	1.4×10^8 s^{-1}	emission rate const.
k0	10 cm/s	standard ET rate const.
Na	6.022×10^{23} mol^{-1}	Avogadro's
n	1	number of electrons
ERevA	-1.3 V	cathodic switching potential
ERevC	1.3 V	anodic switching potential
kd	100 s^{-1}	cation decomposition rate
krq	2×10^{10} $M^{-1}s^{-1}$	radical ion quenching of excited state

[1]E0A refers to "anion" and E0C refers to "cation".

Table A.2. Expressions used in simulations.

Name	Expression	Description
kfA	k0×exp(-alpha×f×(E-E0A))	forward rate constant for reduction
kbA	k0×exp((1-alpha)×f×(E-E0A))	reverse rate constant for reduction
kfC	k0×exp((1-alpha)×f×(E-E0C))	forward rate constant for oxidation
kbC	k0×exp(-alpha×f×(E-E0C))	reverse rate constant for oxidation
Hred	flc1hs(sin(10×pi×t),5e-4)	reduction potential step[1]
Hox	flc1hs(sin(-10×pi×t),5e-4)	oxidation potential step[1]
E	ERevA×Hred+ERevC×Hox	Potential step function
Current	n×FAR×(ndflux_cC_chdi-ndflux_cA_chdi)	Calculation of current from oxidation and reduction diffusive flux[2]

[1]"flc1hs" is the notation for Heaviside function

[2]"ndflux_cC_chdi" represents the normal diffusive flux for the cation (cA is concentration of the anion). ndflux is positive when the analyte is moving away from the electrode.

Table A.3. Boundary settings.

Point		**1**	**2**
Inward Flux (N)	mol/(m^2s)	{'-(kfA+kfC)*cN+kbA*cA+kbC*cC';'-kbA*cA+kfA*cN';'-kbC*cC+kfC*cN';0;0}	{0;0;0;0;0}
Conc.	mol/m^3	{0;0;0;0;0}	{1;0;0;0;0}
Style		{0,{0,0,255}}	{0,{0,0,0}}

Table A.4. Subdomain Settings.

Subdomain		**1**
Diffusion coefficient (D)	m^2/s	{'D';'D';'D';'D';'D'}
Reaction rate (R)	$mol/(m^3 \times s)$	{'kann*cA*cC+kem*cE+krq*(cE*cA+cE*cC)';'-kann*cA*cC';'-kann*cA*cC-kd*cC';'kann*cA*cC-kem*cE-krq*(cA*cE+cC*cE)';0}

Subdomain initial value: cN = 1; cA = cC = cE = cF = 0

Integration coupling variables.
Variable name: ECL (calculates ECL intensity throughout subdomain)
Expression: kem*Na*cE
Order: 4
Global: No
Destination Subdomain: 1 (Geom1)

Solver settings
Analysis type: Transient
Auto select solver: On
Solver: Time dependent
Solution form: Automatic
Symmetric: Auto
Adaption: Off

Parameters
Pivot threshold: 0.1
Memory allocation factor: 0.7

Time stepping parameters:
Times: 0:0.001:1 (for 1 second pulsing incremented in millisecond time steps)
Relative tolerance: 0.01
Absolute tolerance: 0.0010
Times to store in output: Specified times
Time steps taken by solver: Free
Manual tuning of step size: Off
Initial time step: 0.0010
Maximum time step: 1.0
Maximum BDF order: 5
Singular mass matrix: Maybe
Consistent initialization of DAE systems: Backward Euler
Error estimation strategy: Include algebraic
Allow complex numbers: Off

Advanced Settings
Constraint handling method: Elimination
Null space function: Automatic
Assembly block size: 5000
Use Hermitian transpose of constraint matrix and in symmetry detection: Off
Use complex functions with real input: Off
Stop if error due to undefined operation: On
Type of scaling: Automatic
Row equilibration: On
Manual control of reassembly: Off
Load constant: On
Constraint constant: On
Mass constant: On
Damping (mass) constant: On
Jacobian constant: On
Constraint Jacobian constant: On

Appendix B List of Symbols

Roman Symbols

a	Solvent cavity radius
A	Neutral, ground state molecule in solution
$A^{\bullet-}$	Radical anion of molecule in solution
$A^{\bullet+}$	Radical cation of molecule in solution
A_2^*	Excimer
$^1A^*$	Excited singlet state of molecule
$^3A^*$	Excited triplet state of molecule
c	Speed of light
C_d	Double-layer capacitance
D	Diffusion coefficient
E	Potential
E_{ox}^o	Standard oxidation potential
E_p	Peak potential
ΔE_p	Peak potential separation
E_{red}^o	Standard reduction potential
E_s	Excited singlet energy
E_T	(1) Excited triplet energy
	(2) Transition energy

E_T^N	Normalized transition energy
Δf	Polarizability parameter
F	Faraday's constant
Fc	Ferrocene
ΔG	Change in free energy
h	Planck's constant
ΔH	Change in enthalpy
i	Current
i_s	Current from ECL standard
I	ECL intensity
I_s	ECL intensity of standard
$i_{p,a}$	Anodic peak current
$i_{p,c}$	Cathodic peak current
k	Homogeneous reaction rate constant
k^o	Standard, heterogeneous electron transfer rate constant
k_{ann}	Radical ion annihilation rate constant
k_b	Electron transfer rate constant for back reaction
$k_{b,com}$	Rate constant for comproportionation back reaction
k_{em}	Radiative decay rate constant
k_f	Electron transfer rate constant for forward reaction
$k_{f,com}$	Rate constant for comproportionation forward reaction

k_{rq}	Rate constant radical ion quenching of excited states
K_{eq}	Equilibrium constant
n	Refractive index
N_a	Avogadro's constant
P	Arbitrary reaction product
R	Ideal gas constant
R_u	Uncompensated resistance
ΔS	Change in entropy
S_0	Solvent-relaxed ground state
$S_{0,FC}$	Franck-Condon ground state
S_1	Solvent-relaxed first excited singlet state
$S_{1,FC}$	Franck-Condon first excited singlet state
T	Temperature
v	Scan rate
X	Arbitrary impurity in solution

Greek Symbols

α	Transfer coefficient
ε	(1) Dielectric constant
	(2) Extinction coefficient
$\lambda_{max,abs}$	Wavelength at maximum absorbance
$\lambda_{max,PL}$	Wavelength at maximum fluorescence intensity

v	Wavenumber
$\overline{v}_a$	Wavenumber at maximum absorbance
$\overline{v}_f$	Wavenumber at maximum fluorescence intensity
Φ_{ECL}	ECL quantum efficiency
$\Phi_{ECL,QY}$	ECL quantum yield
Φ_{PL}	PL quantum efficiency

Glossary

AM1	Austin Model 1
B^8amide	3,5-diacylamidotoluene-substituted PM567
BODIPY	4,4-difluoro-1,3,5,7-tetramethyl-4-bora-3a,4a-diaza-s-indacene
BPO	Benzoyl peroxide
CCD	Charge-coupled device
CE	Counter electrode
CT	Charge transfer
CV	Cyclic voltammetry
DPA	9,10-diphenylanthracene
(dppy)BTPA	2,6-diphenolpyridineborontriphenylamine
ECL	Electrogenerated chemiluminescence
HET	Heterogeneous electron transfer
HOMO	Highest occupied molecular orbital
LUMO	Lowest unoccupied molecular orbital
MeCN	Acetonitrile
MS	Mass spectrometry
NMR	Nuclear magnetic resonance
PA	Phenylanthracene
PA~X~PA	Spiro-FPA

$PA^{\bullet-}$~X~$PA^{\bullet-}$	Spiro-FPA dianion
$PA^{\bullet+}$~X~$PA^{\bullet+}$	Spiro-FPA dication
PhH	Benzene
PL	Photoluminescence
PM567	4,4-difluoro-2,6-diethyl-1,3,5,7,8-pentamethyl-4-bora-3a,4a-diaza-s- indacene
RE	Reference electrode
Spiro-FPA	2,2′-bis(10-phenylanthracen-9-yl)-9,9′-spirobifluorene
TBAP	Tetra-*n*-butylammonium perchlorate
$TBAPF_6$	Tetra-*n*-butylammonium hexafluorophosphate
TMS	Tetramethylsilane
WE	Working electrode
UME	Ultramicroelectrode

References

Chapter 1

(1) Dufford, R. T.; Nightingale, D.; Gaddum, W. L. *J. Am. Chem. Soc.* **1927**, *49*, 1858.
(2) Harvey, N. *J. Phys. Chem.* **1929**, *33*, 1456.
(3) Hercules, D. M. *Science*. **1964**, *145*, 808.
(4) Rubinstein, I.; Bard, A. *J. Am. Chem. Soc.* **1981**, *103*, 512.
(5) White, H.; Bard, A. *J. Am. Chem. Soc.* **1982**, *104*, 6891.
(6) Leland, J.; Powell, M. *J. Electrochem. Soc.* **1990**, *137*, 3127.
(7) For reviews of ECL applications, see: (a) Fahnrich, K.; Pravda, M.; Guilbault, G. *Talanta*. **2001**, *54*, 531. (b) Knight, A. *TrAC* **1999**, *18*, 47. (c) Richter, M. *Chem. Rev.* **2004**, *104*, 3025.
(8) Obenauer-Kutner, L.; Jacobs, S.; Kolz, K.; Tobias, L.; Bordens, R. *J. Immunol. Methods* **1997**, *206*, 25.
(9) Motmans, K.; Raus, J.; Vandevyver, C. *J. Immunol. Methods* **1996**, *190*, 107.
(10) Chandross, E.; Sonntag, F. *J. Am. Chem. Soc.* **1966**, *88*, 1089.
(11) White, H.; Bard, A. *J. Am. Chem. Soc.* **1982**, *104*, 6892.
(12) Leland, J.; Powell, M. *J. Electrochem. Soc.* **1990**, *137*, 3127.
(13) Rubenstein, I.; Bard, A. *J. Am. Chem. Soc.* **1981**, *103*, 512.
(14) Akins, D.; Birke, R. *Chem. Phys. Lett.* **1974**, *29*, 428.
(15) Choi, J.-P.; Wong, K.-T.; Chen, Y.-M.; Yu, J.-K.; Chou, P.-T.; Bard, A. *J. Phys. Chem. B* **2003**, *107*, 14407.
(16) Chandoross E.; Longworth, J.; Visco, R. *J. Am. Chem. Soc.* **1965**, *87*, 3259.
(17) Maloy, J.; Bard, A. *J. Am. Chem. Soc.* **1971**, *93*, 5968.
(18) Faulkner, L.; Bard, A. *J. Am. Chem. Soc.* **1968**, *90*, 6284.
(19) Lakowicz, J.; *Principles of Fluorescence Spectroscopy*. Plenum Press: NY, **1983**, pp 189-215.
(20) Lippert, V. *Z. Electrochem.* **1957**, *61*, 962.
(21) Seliskar, C.; Brand, L. *J. Am. Chem. Soc.* **1971**, *93*, 5414.
(22) Schuddeboom, W.; Jonker, S.; Warman, J.; Leinhos, U.; Kühnle, W.; Zachariasse, K. *J. Phys. Chem.* **1992**, *96*, 10809.
(23) Subuddh, U.; Haldar, S.; Sankararaman, S.; Mishra, A. *Photochem. Photobiol. Sci.* **2006**, *5*, 459.
(24) Reichardt, C. *Chem. Rev.* **1994**, *94*, 2319.
(25) Ravi, M.; Soujanya, T.; Samanta, A.; Radhakrishnan, T. *J. Chem. Soc. Faraday Trans.* **1995**, *91*, 2739.
(26) Rave, M.; Samanta, A.; Radhakrishnan, T. *J. Phys. Chem.* **1994**, *98*, 9133.

Chapter 2

(1) Maloy, J. In *Electrogenerated Chemiluminescence*; Bard, A.; Ed.; Marcel Dekker: New York, NY, **2004**, pp. 101-106.
(2) Feldberg, S. *J. Am. Chem. Soc.* **1966**, *88*, 390.
(3) Feldberg, S. *J. Phys. Chem.* **1966**, *12*, 3928.
(4) Cruser, S.; Bard, A. *J. Am. Chem. Soc.* **1969**, *91*, 267.
(5) (a) Rudolph, M.; Reddy, D.; Feldberg, S. *Anal. Chem.* **1994**, *66*, 589A; (b) Bott, A.; Feldberg, S.; Manfred, R. *Curr. Sep.* **1996**, *15*, 67; (c) Ketter, J.; Forry, S.; Wightman, M.; Feldberg, S. *Electrochem. Solid-State Lett*. **2003**, *7*, E18.
(6) (a) Rudolph, M. *J. Electroanal. Chem.* **2003**,*543,* 23; (b) Ruldolf, M. *J. Electroanal. Chem.* **2004**, *571*, 289; (c) Rudolph, M. *J. Electroanal. Chem.* **2003**, *558*, 171. (d) Rudolph, M. *J. Comp. Chem.* **2005**, *26*, 619; (e) Rudolph, M. *J. Comp. Chem.* **2005**, *26*, 233; (f) Rudolph, M. *J. Comp. Chem.* **2005**, *26*, 1193.
(7) (a) Svir, I.; Oleinick, A.; Klimenko, A. *J. Electroanal. Chem.* **2001**, *513*, 119.
(8) Collinson, M.; Wightman, R.; Paolo, P. *J. Phys. Chem.* **1994**, *98*, 11942.
(9) Boens, N.; Qin, W.; Basarić, N.; Hofkens, J.; Ameloot, M.; Pouget, J.; Lefèvre, J.-P.; Valeur, B.; Gratton, E.; vandeVen, M.; Silva, N.; Engelborghs, Y.; Willaert, K.; Sillen, A.; Rumbles, G.; Phillips, D.; Visser, A.; van Hoek, A.; Lakowicz, J.; Malak, H.; Gryczynski, I.; Szabo, A.; Krajcarski, D.; Tamai, N.; Miura, A. *Anal. Chem.* **2007**, *79*, 2137.

Chapter 3

(1) Yamaguchi, S.; Tomonori, E.; Uchida, M.; Izumizawa, T.; Furukawa, K.; Tamao, K. *Chem. Eur. J.* **2000**, *6*, 1683.
(2) Zhan, X.; Risko, C.; Amy, F.; Chan, C.; Zhao W.; Barlow, S.; Kahn, A.; Brédas, J.-L.; Marder, S. *J. Am. Chem. Soc.* **2005**, *127*, 9021.
(3) Yu, G.; Yin, S.; Liu Y.; Chen J.; Xu, X.; Sun, X.; Ma D.; Zhan, X.; Peng, Q.; Shuai, Z.; Tang, B.; Zhu, D.; Fang, W.; Luo, Y. *J. Am. Chem. Soc.* **2005**, *127*, 6335.
(4) Lee, J.; Liu, Q.-D.; Motala, M.; Dane, J.; Gao, J.; Kang, Y.; Wang, S. *Chem. Mater.* **2004**, *16*, 1869.
(5) Chen, J.; Law, C.; Lam, J.; Dong, Y.; Lo, S.; Williams, I.; Zhu, D.; Tang, B. *Chem. Mater.* **2003**, *15*, 1535.
(6) Janzen, E.; Harrison, W.; Dubose, C. *J. Organometal. Chem.* **1972**, *40*, 281.
(7) Yamaguch, S.; Endo, T.; Uchida, M.; Izumizawa, T.; Furukawa, K.; Tamao, K. *Chem. Lett.* **2001**, 98.
(8) Dhiman, A.; Zhang, Z.-R.; West, R.; Becker, J. Y. *J. Electroanal. Chem.* **2004**, *569*, 15-22.
(9) Tamao, K.; Yamaguchi, S.; Shiro, M. *J. Am. Chem. Soc.* **1994**, *116*, 11715.

(10) a) S. Yamaguchi, T. Endo, M. Uchida, T. Izumizawa, K. Furukawa, K. Tamao, *Chem. Eur. J.* **2000**, *6*, 1683-1692; b) J. Lee, Q.-D. Liu, M. Motala, J. Dane, J. Gao, Y. Kang, S. Wang, *Chem. Mater.* **2004**, *16*, 1869-1877. Increased quantum yields (21%) have been obtained from 3,4-diarylsiloles via aggregation-induced emission, see: a) J. Luo, Z. Xie, J. W. Y. Lam, L. Cheng, H. Chen, Q. Chengfeng, H. S. Kwok, X. Zhan, Y. Lui, D. Zhu, B. Z. Tang, *Chem. Commun.* **2001**, 1740-1741; b) J. Chen, Z. Xie, J. W. Y. Lam, C. C. W. Law, B. Z. Tang, *Macromolecules* **2003**, *36*, 1108-1117; c) J. Chen, C. C. W. Law, J. W. Y. Lam, Y. Dong, S. M. F. Lo, I. D. Williams, D. Zhu, B. Z. Tang, *Chem. Mater.* **2003**, *15*, 1535-1546.

(11) Boydston, A. J.; Pagenkopf, P. L. *Angew. Chem. Int. Ed.* **2004**, *43*, 6336.

(12) Tamao, K.; Uchida, M.; Izumizawa, T.; Furukawa, K.; Yamaguchi, S. *J. Am. Chem. Soc.* **1996**, *118*, 11974.

(13) Uchida, M.; Izumizawa, T.; Nakano, T.; Yamaguchi, S.; Tamao, K; Furukawa, K. *Chem. Mater,* **2001**, *13*, 2680.

(14) Tang, B. Z.; Zhan, X.; Yu, G.; Lee, P. P. S.; Liu, Y.; Zhu, D. *J. Mater. Chem.*, **2001**, *11*, 2974.

(15) Yamaguch, S.; Tamao, K. *J. Chem. Soc., Dalton Trans.* **1998**, 3693.

(16) For reviews of ECL, see: (a) Richter, M. M. *Chem. Rev.* **2004**, *104*, 3003; (b) *Electrogenerated Chemiluminescence*; Bard, A.; Marcel Dekker: New York, NY, 2004.

(17) Dietz, R. In *Organic Electrochemistry*; Baizer, M.; Ed.; Marcel Dekker: New York, NY, **1973**, pp 256-266.

(18) Eberson, L. In *Organic Electrochemistry*; Baizer, M.; Ed.; Marcel Dekker: New York, NY, **1973**, pp 448-465.

(19) Boydston, A. J.; Pagenkopf, P. L. *Angew. Chem. Int. Ed.* **2004**, *43*, 6336.

(20) Chen, S.-A.; Shy, H.-J. *J. Poly. Sci.: Poly. Chem. Ed.* **1985**, *23*, 2441.

(21) Sahami, S.; Weaver, M. *J. Electroanal. Chem.* **1981**, *122*, 155.

(22) (a) Rudolf, M. *J. Electroanal. Chem.* **2003**,*543,* 23; (b) Ruldolf, M. *J. Electroanal. Chem.* **2004**, *571*, 289; (c) Rudolf, M. *J. Electroanal. Chem.* **2003**, *558*, 171. (d) Rudolf, M. *J. Comp. Chem.* **2005**, *26*, 619; (e) Rudolf, M. *J. Comp. Chem.* **2005**, *26*, 233; (f) Rudolf, M. *J. Comp. Chem.* **2005**, *26*, 1193.

(23) Kadish, K.; Ding, J.; Malinski, T. *Anal. Chem.* **1984**, *56*, 1741.

(24) Bard, A. and Faulkner L.; *Electrochemical Methods: Fundamentals and Applications, 2nd Ed*; John Wiley & Sons, Inc.: NY, **2001**, pp 234-238.

(25) Cauquis, G. In *Organic Electrochemistry*; Baizer, M.; Ed.; Marcel Dekker: New York, NY, **1973**, pp 33-35.

(26) Bard, A. and Faulkner L.; *Electrochemical Methods: Fundamentals and Applications, 2nd Ed*; John Wiley & Sons, Inc.: NY, **2001**, pp 471-528.

(27) Bard, A. and Faulkner L.; *Electrochemical Methods: Fundamentals and Applications, 2nd Ed*; John Wiley & Sons, Inc.: NY, **2001**, pp 507.

Chapter 4

(1) (a) Cauquis, G. Basic Concepts. In *Organic Electrochemistry*; Baizer, M., Ed.; Marcel Dekker, Inc.: New York, 1973; pp 43-48. (b) Bard, A.; Faulkner, L. *Electrochemical Methods: Fndamentals and Applications*, 2nd ed.; John Wiley & Sons, Inc.: New York, 2001; pp 108, 475-476. (c) Zanelo, P. *Inorganic Electrochemistry: Theory, Practice, and Application*; The Royal Society of Chemistry: Cambridge, UK, 2003; pp 99-100.

(2) Murov, S. L.; Carmichael, I.; Hug, G. L.; *Handbook of Photochemistry, 2nd Edition, Revised and Expanded*; Marcel Dekker, Inc.: NY, **1993**, p 9.

(3) Itoh, K.; Honda, K.; Sukigara, M. *Electrochimica Acta*. **1979**, *24*, 1195.

(4) (a) Phelps J.;Santhanam K. S. V.; Bard A. J. *J. Am. Chem. Soc.* **1967**, *89*, 1752; (b) Sioda, R. E. *J. Phys. Chem.* **1968**, *72*, 2322.

(5) Bard, A. J. *Electrogenerated Chemiluminescence,* Marcel Dekker, N.Y. 2004, p. 5.

(6) Shen, W.-J.; Dodda, R.; Wu, C.-C.; Wu, F.-I.; Liu, T.-H.; Chen, H.-H.; Chen, C. H.; Shu, C.-F. *Chem. Mater.* **2004**, *16*, 930.

(7) For reviews on ECL, see: (a) Richter, M. M. *Chem. Rev.* **2004**, *104*, 3003-3036; (b) Knight, A. W.; Greenway, G. M. *Analyst* **1994**, *119*, 879-890; (c) Faulkner, L. R.; Bard, A. J. *Electroanalytical Chemistry*; Marcel Dekker: New York, 1977; Vol. 10, p 1; (d) Bard, A. J.; Debad, J. D.; Leland, J. K.; Sigal, G. B.; Wilbur, J. L.; Wohlstadter, J. N. In *Encyclopedia of Analytical Chemistry: Applications, Theory and Instrumentation*; Meyers, R. A., Ed.; John Wiley & Sons: New York, 2000; Vol. 11, p 9842.

(8) (a) Keszthelyi C. P.; Bard, A. J. *Chem. Phys. Lett*. **1974**, *24*, 300. (a) Park, S. M.; Paffett, M. T.; Daub, G. H. *J. Am. Chem. Soc.* **1977**, *99*, 5394. (b) Choi, J.-P.; Wong, K.-T.; Chen, Y.-M.; Yu, J.-K.; Chou, P.-T.; Bard, A. J. *J. Phys. Chem. B*. **2003**, *107*, 14407.

(9) Werner, T.; Chang, J.; Hercules, D. *J. Am. Chem. Soc.* **1970**, *92*, 763.

(10) Birks, J. B. *Photophysics of Aromatic Molecules*; Wiley-Interscience: New York, 1970; Chapter 7.

(11) Bard, A.; Santhanam, K.; Maloy, J.; Phelps, J.; Wheeler, L. *Disc. Farad. Soc.* **1968**, *45*, 167.

(12) Chandross, E.; Longworth, J.; Visco, R. *J. Am. Chem. Soc.* **1965**, *87*, 3259.

(13) Park, M. Y.; Yang, S. G.; Jadhav, V.; Kin, Y. H. *Tetrahedron Letters*. **2004**, *45*, 4887.

(14) Sahami, S.; Weaver, M. *J. Electroanal. Chem.* **1981**, *122*, 155.

(15) (a) Rudolph, M. *J. Electroanal. Chem.* **2003**,*543,* 23; (b) Ruldolf, M. *J. Electroanal. Chem.* **2004**, *571*, 289; (c) Rudolph, M. *J. Electroanal. Chem.* **2003**, *558*, 171. (d) Rudolph, M. *J. Comp. Chem.* **2005**, *26*, 619; (e) Rudolph,

M. *J. Comp. Chem.* **2005**, *26*, 233; (f) Rudolph, M. *J. Comp. Chem.* **2005**, *26*, 1193.
(16) Kadish, K. M.; Ding, J. Q.; Malinski, T. *Anal. Chem.* **1984**, *56*, 1741.
(17) Collinson, M.; Wightman, M.; Pastore, P. *J. Phys. Chem.* **1994**, *98*, 11942. The reported value, 2×10^{10} $M^{-1}s^{-1}$ resulted in negative concentrations, but 10^{8} was deemed fast enough to adequately represent the data on the time scale of this experiment.
(18) Boens, N.; Qin, W.; Basaric, N.; Hofkens, J.; Ameloot, M.; Pouget, J.; Lefèvre, J.-P.; Valeur, B.; Gratton, E.; vandeVen, M.; Silva, N.; Engelborghs, Y.; Willaert, K.; Sillen, A.; Rumbles, G.; Phillips, D.; Visser, A.; van Hoek, A.; Lakowicz, J.; Malak, H.; Gryczynski, I.; Szabo, A.; Krajcarski, D.; Tamai, N.; Miura, A. *Anal. Chem.* **2007**, *79*, 2137.
(19) Bard, A. J.; Faulkner, L. R. *Electrochemistry: Fundamentals and Applications*; John Wiley & Sons: New York, NY, 2001; pp 245-246.
(20) Sioda, R. *J. Phys. Chem.* **1968**, *72*, 2322.
(21) Santhanam, K.; Bard, A. *J. Am. Chem. Soc.* **1966**, *88*, 2669.
(22) Faulkner, L. R.; Bard, A. J. *J. Am. Chem. Soc.* **1968**, *90*, 6284.

Chapter 5

(1) Li, Y.; Bu, W.; Guo, J.; Wang, Y. *Chem. Commun.* **2000**, 1551.
(2) Yang, G.; Liao, Y.; Su, Z.; Zhang, H.; Wang, Y. *J. Phys. Chem. A*. **2006**, *110*, 8758.
(3) Zhang, H.; Huo, C.; Zhang, J.; Zhang P.; Tian, W.; Wang, Y. *Chem. Commun.* **2006**, 281.
(4) For reviews on ECL, see: (a) *Electrogenerated Chemiluminescence*; Bard, A., Ed.; Marcel Dekker, Inc.: New, York, NY, **2004**. (b) Richter, M. M. *Chem. Rev.* **2004**, *104*, 3003-3036; (c) Knight, A. W.; Greenway, G. M. *Analyst* **1994**, *119*, 879-890; (d) Faulkner, L. R.; Bard, A. J. *Electroanalytical Chemistry*; Marcel Dekker: New York, 1977; Vol. 10, p 1; (e) Bard, A. J.; Debad, J. D.; Leland, J. K.; Sigal, G. B.; Wilbur, J. L.; Wohlstadter, J. N. In *Encyclopedia of Analytical Chemistry: Applications, Theory and Instrumentation*; Meyers, R. A., Ed.; John Wiley & Sons: New York, 2000; Vol. 11, p 9842.
(5) Akins, D. L.; Birke, R. L. *Chem. Phys. Lett.* **1974**, *29*, 428.
(6) Chandross, E.; Sonntag, F. *J. Am. Chem. Soc.* **1966**, *88*, 1089.
(7) Choi, J.-P.; Wong, K.-T.; Chen, Y.-M.; Yu, J.-K.; Chou, P.-T.; Bard, A. *J. Phys. Chem. B*. **2003**, *107*, 14407.
(8) (a) Kapturkiewicz, A.; Grabowski, Z.; Jasny, J. *J. Electroanal. Chem.* **1990**, *279*, 55. (b) Kapturkiewicz, A. *J. Electroanal. Chem.* **1991**, *302*, 131. (c) Kapturkiewicz, A. *Chemical Physics*. **1992**, *166*, 259. (d) Kapturkiewicz, A.; Herbich, J.; Nowacki, J. *Chem. Phys. Lett.* **1997**, *275*, 355.
(9) Kapturkiewicz, A. *Z. Physik. Chem. NF*. **1991**, *170*, 87.

(10) Kapturkiewicz, A. *J. Electroanal. Chem.* **1990**, *290*, 135.
(11) Lackowicz, J. R. *Principles of Fluorescence Spectroscopy*; Plenum Press: New York, 1983; pp 189-208.
(12) Sahami, S.; Weaver, M. *J. Electroanal. Chem.* **1981**, *122*, 155.
(13) (a) Rudolph, M. *J. Electroanal. Chem.* **2003**,*543,* 23; (b) Ruldolph, M. *J. Electroanal. Chem.* **2004**, *571*, 289; (c) Rudolph, M. *J. Electroanal. Chem.* **2003**, *558*, 171. (d) Rudolph, M. *J. Comp. Chem.* **2005**, *26*, 619; (e) Rudolph, M. *J. Comp. Chem.* **2005**, *26*, 633; (f) Rudolph, M. *J. Comp. Chem.* **2005**, *26*, 1193.
(14) Kadish, K.; Ding, J.; Malinski, T. *Anal. Chem.* **1984**, *56*, 1741.
(15) Wallace, W.; Bard, A. *J. Phys. Chem.* **1979**, *83*, 1350.
(16) Ghilane, J.; Hapiot, P.; Bard, A. *Anal. Chem.* **2006**, *78*, 6868.
(17) Eberson, L. In *Organic Electrochemistry*; Baizer, M.; Ed.; Marcel Dekker: New York, NY, **1973**, pp 518-520.
(18) Seo, E.; Nelson, R.; Fritsch, J.; Marcoux, L.; Adams, R. *J. Am. Chem. Soc.* **1966**, *88*, 3498.
(19) Yang, G.; Liao, Y.; Su, S.; Zhang H.; Wang, Y. *J. Phys. Chem. A*. **2006,** *110*, 8758.
(20) Handbook of Chemistry and Physics, 87th Edition, 2006-2007. http://www.hbcpnetbase.com/ (Accessed 10/23/06).
(21) (a) Caspar, J.; Kober, E.; Sullivan, B.; Meyer, T. *J. Am. Chem. Soc.* **1982**, *104*, 630. (b) Englman, R.; Jortner, J. *Molecular Physics*, **1970**, *18*, 145.
(22) (a) Morimoto, A.; Biczók, L.; Yatsuhashi, T.; Shimada, T.; Baba, S.; Tachibana, H.; Tryk, D.; Inoue, H. *J. Phys. Chem. A*. **2002**, *106*, 10089. (b) Willets, K.; Callis, P.; Moerner, W. *J. Phys. Chem. B*. **2004**, *108*, 10465. (c) Anni, M.; Sala, F.; Raganato, M.; Fabiano, E.; Lattante, S.; Cingolani, R.; Gigli, G. *J. Phys. Chem. B*. **2005**, *109*, 6004.
(23) (a) Chapman, C.; Maroncelli, M. *J. Phys. Chem.* **1991**, *95*, 9095. (b) Huppert, D.; Bart, E. *Chem. Phys. Lett.* **1992**, *195*, 37. (c) Lavallee, R.; Zimmt, M. *J. Phys. Chem.* **1994**, *98*, 4254.
(24) Marcus, R. A. *J. Phys. Chem.* **1989**, *93*, 3078.
(25) Fabrizio, E.; Prieto, I.; Bard, A. *J. Am. Chem. Soc.* **2000**, *122*, 4996.

Chapter 6

(1) Cruser, S.; Bard, A. *J. Am. Chem. Soc.* **1969**, *91*, 1969.
(2) Lai, R.; Bard, A. *J. Phys. Chem. B.* **2005**, *107*, 5036.
(3) Karolin, J.; Johansson, L.; Strandberg, L.; Ny, T. *J. Am. Chem. Soc.* **1994**, *116*, 7801.
(4) Wagner, R.; Lindsey, J. *Pure Appl. Chem.* **1996**, *68*, 1373.

(5) (a) Guggenheimer, S.; Boyer, J.; Thangaraj, K.; Shah, M.; Soong, M.; Pavlopoulos, T. *Applied Optics*. **1993**, *32*, 3942. (b) O'Neil, M. *Optics Letters*. **1993**, *18*, 37.
(6) Burghart, A.; Kin, H.; Welch, M.; Thoresen, L.; Reibenspies, J.; Burgess, K. *J. Org. Chem.* **1999**, *64*, 7813.
(7) Ziessel, R.; Ulrich, G.; Harriman, A. *New J. Chem.* **2007**, *31*, 496.
(8) Arbeloa, T.; Arbeloa, F.; Arbeloa, I.; García-Moreno, I.; Costela, A.; Sastre, R.; Amat-Guerri, F. *Chem. Phys. Lett.* **1999**, *299*, 315.
(9) Arbeloa, F.; Arbeloa, T.; Arbeloa, I.; García-Moreno, I.; Costela, A.; Sastre, R.; Amat-Guerri, F. *Chem. Phys.* **1998**, *236*, 331.
(10) Camerel, F.; Bonardi, L.; Schmutz, M.; Ziessel, R. *J. Am. Chem. Soc.* **2006**, *128*, 4548.
(11) Camerel, F.; Bonardi, L.; Ulrich, G.; Charbonnière, L.; Donnio, B.; Bourgogne, C.; Gillon, D.; Retailleau, P.; Ziessel, R. *Chem. Mater.* **2006**, *18*, 5009.
(12) For reviews on ECL, see: (a) *Electrogenerated Chemiluminescence*; Bard, A., Ed.; Marcel Dekker, Inc.: New, York, NY, **2004**. (b) Richter, M. M. *Chem. Rev.* **2004**, *104*, 3003-3036; (c) Knight, A. W.; Greenway, G. M. *Analyst* **1994**, *119*, 879-890; (d) Faulkner, L. R.; Bard, A. J. *Electroanalytical Chemistry*; Marcel Dekker: New York, 1977; Vol. 10, p 1; (e) Bard, A. J.; Debad, J. D.; Leland, J. K.; Sigal, G. B.; Wilbur, J. L.; Wohlstadter, J. N. In *Encyclopedia of Analytical Chemistry: Applications, Theory and Instrumentation*; Meyers, R. A., Ed.; John Wiley & Sons: New York, 2000; Vol. 11, p 9842.
(13) (a) Werner, T.; Chang, J.; Hercules, D. *J. Am. Chem. Soc.* **1970**, *92*, 763. (b) Werner, T.; Chang, J.; Hercules, D. *J. Am. Chem. Soc.* **1970**, *92*, 5560.
(14) Choi, J.-P.; Wong, K.-T.; Chen, Y.-M.; Yu, J.-K.; Chou, P.-T.; Bard, A. *J. Phys. Chem. B* **2003**, *107*, 14407.
(15) Werner, T.; Chang, J.; Hercules, D. *J. Am. Chem. Soc.* **1970**, *92*, 763.
(16) Chandross, E.; Longworth, J.; Visco, R. *J. Am. Chem. Soc.* **1965**, *87*, 3259.
(17) (a) Prieto, I.; Teetsov, J.; Fox, M.; Vanden Bout, D.; Bard, A. *J. Phys. Chem. A*, **2001**, *105*, 520. (b) Fungo, F.; Wong, K.-T.; Ku, S.-Y.; Hung, Y.-Y.; Bard, A. *J. Phys. Chem. B*, **2005**, *109*, 3984. (c) Sartin, M.; Shen, W.-J.; Dodda, R.; Wu, C.-C.; Wu, F.-I.; Liu, T.-H.; Chen, H.-H.; Chen, C.; Shu, C.-F.; Bard, A. **Manuscript in preparation**.
(18) Sahami, S.; Weaver, M. *J. Electroanal. Chem.* **1981**, *122*, 155.
(19) Ghilane, J.; Hapiot, P.; Bard, A. *Anal. Chem.* **2006**, *78*, 6868.
(20) (a) Rudolf, M. *J. Electroanal. Chem.* **2003**,*543,* 23; (b) Ruldolf, M. *J. Electroanal. Chem.* **2004**, *571*, 289; (c) Rudolf, M. *J. Electroanal. Chem.* **2003**, *558*, 171. (d) Rudolf, M. *J. Comp. Chem.* **2005**, *26*, 619; (e) Rudolf, M. *J. Comp. Chem.* **2005**, *26*, 633; (f) Rudolf, M. *J. Comp. Chem.* **2005**, *26*, 1193.

(21) Kadish, K.; Ding, J.; Malinski, T. *Anal. Chem.* **1984**, *56*, 1741.
(22) The actual values used in reference (2) have been adjusted here, because the authors of reference (2) chose ferrocene as 0.424 V vs SCE, whereas we used 0.342 V vs SCE.
(23) Cauquis, G. In *Organic Electrochemistry*; Baizer, M.; Ed.; Marcel Dekker: New York, NY, **1973**, pp 33-35.
(24) Marcus, R. A. *J. Phys. Chem.* **1989**, *93*, 3078.

Vita

Matthew McCullough Sartin was born in Chester, Pennsylvania on January 21, 1982, the son of Eva Ann Sartin and James Lewis Sartin, Jr. After completing his work at Auburn High School in Auburn, Alabama, in 2000, he entered Auburn University at Auburn, Alabama. While pursuing his undergraduate degree, he worked as a research assistant for Dr. German Mills, who taught physical chemistry at the university. In 2003, he received the degree of Bachelor of Science in Chemistry from the Department of Chemistry. In August, 2003, he joined The Graduate School at The University of Texas at Austin. In December, 2005, he received the degree Master of Arts in Chemistry from The University of Texas, and continued his graduate education in the same research group.

Permanent Address: 406 Dixie Drive

Auburn, Alabama 36832

This dissertation was typed by the author.